Common mode filter design for mitigation of bearing degradation in inverter-fed Motor drive systems

Fan, Fei

2019

Fan, F. (2019). Common mode filter design for mitigation of bearing degradation in inverter-fed Motor drive systems. Doctoral thesis, Nanyang Technological University, Singapore.

https://hdl.handle.net/10356/138382

https://doi.org/10.32657/10356/138382

Common Mode Filter Design for Mitigation of Bearing Degradation in Inverter-Fed Motor Drive Systems

Fan Fei

School of Electrical & Electronic Engineering

A thesis submitted to the Nanyang Technological University
in partial fulfillment of the requirement for the degree of
Doctor of Philosophy

2019

STATEMENT OF ORIGINALITY

I hereby certify that the work embodied in this thesis is the result of original research, is free of plagiarised materials, and has not been submitted for a higher degree to any other University or Institution.

4/3/2020   Fan Fei

. . . .
. . . .

    Date   Fan Fei

SUPERVISOR DECLARATION STATEMENT

I have reviewed the content and presentation style of this thesis and declare it is free of plagiarism and of sufficient grammatical clarity to be examined. To the best of my knowledge, the research and writing are those of the candidate except as acknowledged in the Author Attribution Statement. I confirm that the investigations were conducted in accord with the ethics policies and integrity standards of Nanyang Technological University and that the research data are presented honestly and without prejudice.

4/3/2020

Assoc Prof See Kye Yak

. . . .
. . . .

Date   See Kye Yak

AUTHORSHIP ATTRIBUTION STATEMENT

This thesis contains material from 4 papers published in the following peer-reviewed journal and conference papers in which I am listed as an author.

Chapter 3 Section 1 is published as the following paper:

T. Svimonishvili, <u>F. Fan</u>, K. Y. See, X. Liu, M. A. Zagrodnik and A. K. Gupta, "High-frequency model and simulation for the investigation of bearing current in inverter-driven induction machines," IEEE Region 10 Conference (TENCON), pp. 55-59, Singapore, 2016.

The contributions of the co-authors are as follows:

- Prof See provided the initial project direction and edited the final manuscript draft.
- Dr. Tengiz prepared the manuscript draft.
- I co-designed the simulation and analyzed the data.
- The manuscript was revised with the comments from Dr. Liu, Mr. Zagrodnik and Dr. Amit from Rolls-Royce, who are our industrial collaborators.

Chapter 3 Section 2 is published as the following paper:

<u>F. Fan</u>, K. Y. See, J. K. Banda, X. Liu and A. K. Gupta, "Simulation of three-phase motor drive system with bearing discharge process," Progress in Electromagnetics Research Symposium, pp. 2091-209, Singapore, 2017.

The contributions of the co-authors are as follows:

- Prof See suggested the research area and edited the final manuscript draft.
- I designed the bearing discharge model, performed all the simulation work and analyzed the data.
- I prepared the draft of the manuscript and was revised by Mr. Banda, who is another researcher of Prof See.

- The manuscript was revised with the comments from Dr. Liu and Dr. Amit from Rolls-Royce, who are our industrial collaborators.

Chapter 3 Section 3 is published as the following paper:

F. Fan, K. Y. See, J. K. Banda, X. Liu and A. K. Gupta, "Investigation and mitigation of premature bearing degradation in motor drive system," IEEE Electromagnetic Compatibility Magazine, vol. 8, no. 1, pp. 75-81, 2019.

The contributions of the co-authors are as follows:

- Prof See provided the initial project direction and edited the final manuscript draft.
- I setup up the prototype test jig and carried out all the experiments.
- I did all the simulation and analysis of the CM filter performance.
- Mr. Banda assisted in the collection of the bearing degradation data.
- The manuscript was revised with the comments from Dr. Liu and Dr. Amit from Rolls-Royce, who are our industrial collaborators.

Chapter 4 is published as the following paper:

F. Fan, K. Y. See, K. Li, X. Liu, M. A. Zagrodnik and A. K. Gupta, "In-circuit common-mode impedance measurement for motor drive system," Asia-Pacific International Symposium on Electromagnetic Compatibility (APEMC), pp. 1-3, Seoul, 2017.

The contributions of the co-authors are as follows:

- Prof See provided the initial project direction and edited the final manuscript draft.
- I proposed a new measurement approach and did all the tests with the technical support from Dr. Li, who is another researcher of Prof See.
- I prepared the manuscript draft and it was revised with the comments from Dr. Liu, Mr. Zagrodnik and Dr. Amit from Rolls-Royce, who are our industrial collaborators.

Chapter 5 is published as the following paper:

<u>F. Fan</u>, K. Y. See, K. R. Li, et al. "Systematic Common-Mode Filter Design for Inverter-Driven Motor System based on In-Circuit Impedance Extraction", IEEE Transactions on Electromagnetic, accepted for publication.

The contributions of the co-authors are as follows:

- Prof See provided the initial project direction and edited the final manuscript draft.
- I proposed a new CM filter design approach and did all the tests with the technical support from Dr. Li, who is another researcher of Prof See.
- I performed the FEM simulation of a CM choke.
- The manuscript was revised with the comments from Dr. Liu, and Dr. Amit from Rolls-Royce, who are our industrial collaborators.

4/3/2020

Date

Fan Fei

Fan Fei

ACKNOWLEDGEMENTS

TABLE OF CONTENTS

ABSTRACT

Recent advancements in the insulated-gate bipolar transistor (IGBT) enable higher switching speeds in power electronics and have improved the power conversion efficiency significantly. Hence, pulse width modulated (PWM) variable frequency drives (VFDs) are widely used in modern control of electro-mechanical drive systems. On the other hand, higher switching frequencies cause the presence of high-frequency common-mode (CM) voltage, which results in unwanted CM current flows through the motor bearing and leads to premature motor bearing failures, such as frosting, fluting and pitting. Consequently, new drive installations can fail within months, which results in unplanned and costly system downtime. Thus, it is important to understand the different cause-and-effect chains of different types of bearing current so that cost-effective mitigation techniques for a certain drive configuration can be proposed. A prototype consists of a commercially available inverter and a 5.5 kW induction motor is used as a system-under-investigation to better understand the fundamental mechanism of bearing degradation and the necessary countermeasures.

Modifying and hardening the bearing design may not be always possible and may affect the overall operation of the motor. Hence, it is best to have an effective solution without modifying the motor and adding an external CM filter to attenuate the CM current entering into the induction motor is explored in this thesis. Optimal CM filter design requires prior knowledge of both the source and termination impedances of the filter. To facilitate the measurement of the source and termination impedances, an inductive coupling approach is adopted to extract these impedances. To allow the

proposed inductive coupling approach be used in high-power motor drive systems, further improvements are necessary to extract in-circuit CM impedance of a motor drive system. Such improvements offer enhanced signal-to-noise ratio under a harsh electrical background noise environment. With the successful extraction of in-circuit source and termination impedances, a suitable CM filter can be designed systematically to achieve the desired attenuation without guessing and overdesigning. In the evaluation of first-order single-inductor and second-order LC filters, it is found that the second-order filter may not be always a better choice due to DM-to-CM conversion in the motor drive system, as the system is usually asymmetrical in nature. With the known information of the CM noise source and termination impedances, one can also evaluate the effect of the mode conversion on the CM filter design in a quantitative way.

LIST OF FIGURES

LIST OF TABLES

LIST OF ABBREVIATION

BNC   Bayonet Neill-Concelman

BVR   Bearing Voltage Ratio

CM   Common Mode

CISPR   Comité International Spécial des Perturbations

                Radioélectriques

DM   Differential Mode

DUT   Device Under Test

EDM   Electrical Discharge Machining

EMC   Electromagnetic Compatibility

EMI   Electromagnetic Interference

ESL   Equivalent Series Inductor

HF   High Frequency

IGBT   Insulated Gate Bipolar Transistor

IT   Insulated Terrestrial

LISN   Line Impedance Stabilization Network

MOSFET   Metal Oxide Semiconductor Field-Effect Transistor

PWM	Pulse Width Modulation
RF	Radio Frequency
SA	Spectrum Analyzer
SNR	Signal-to-noise Ratio
SOL	Short-open-load
SMPS	Switched-Mode Power Supply
SPWM	Sinusoidal Pulse Width Modulation
VFD	Variable-frequency Drive
VNA	Vector Network Analyzer

Chapter 1   Introduction

1.1   Background

Performance improvements with competitive pricing of power electronic converters have led to wide usage of variable frequency drives (VFDs) [1-3]. The use of pulse-width-modulated (PWM) VFDs to control AC machines for motor drive systems has been growing since the invention of insulated-gate bipolar transistor (IGBT) at 1980s [4]. The advancements of power electronics devices and their ability to operate at higher switching frequencies have resulted in better motor torque and speed controls, as well as improved efficiency, which contributes to substantial energy savings [5-7]. Hence, both land- and marine-based applications have benefited from these significantly improved, efficient and low-cost PWM VFDs [8].

Even though VFDs offer energy savings and great flexibility in AC motor operation, PWM VFDs incorporating high-speed switching devices produce time-varying high-amplitude common mode (CM) voltage with high dv/dt[9]. The CM voltage causes the flow of undesired CM current in the motor drive system, which not only lead to EMI associated problems but also results in premature motor bearing failures, such as frosting, fluting and pitting as illustrated in Fig. 1-1[10]. High levels of CM voltage can also yield motor winding and cable insulation degradation. Consequently, new drive installations can fail within months after their operation, which contributes to unplanned and costly system downtime[11]. It is reported that over 40% of all motor failure is caused by bearing failure[12].
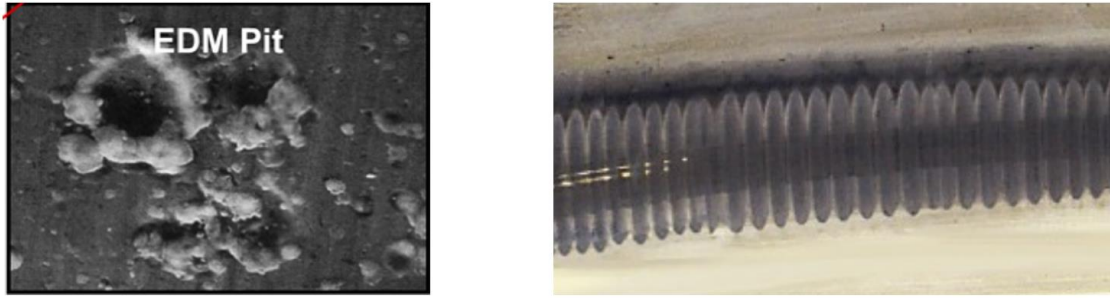
Fig. 1-1 Premature motor bearing failure

1.2 Terminologies
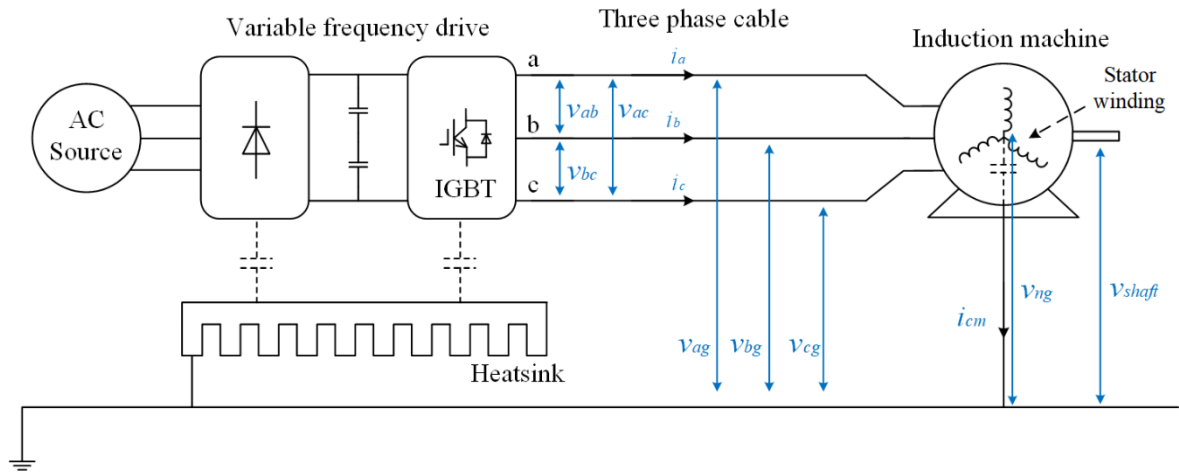
Fig. 1-2 CM voltage and CM current in a motor drive system

Fig. 1-2 shows a simplified diagram of a typical motor drive system. The induction motor is powered through the inverter via a three-phase cable. The metal frame of the motor and the heatsink of the inverter are usually grounded for safety reasons. The stray capacitances in the system provide the return path of the high-frequency CM current, from motor stator winding to heatsink and then back to IGBT devices. The commonly used terminologies in Fig. 1-2 are given as follows here:

- v_{ab}, v_{bc} and v_{ac}: phase-to-phase voltage.

- v_{ag}, v_{bg} and v_{cg}: phase-to-ground voltage.

- v_{ng}: neutral-to-ground voltage.

- i_a, i_b and i_c: phase current.

- i_{cm}: CM current.

- v_{shaft}: voltage between motor shaft and ground.

A commonly used two-level PWM voltage source inverter consists of three-phase legs and each leg is a series connection of two IGBT or MOSFET switches. The output terminal of each phase is connected to either the positive dc bus or negative dc bus during normal operation, so that the output voltage could be $+V_{dc}/2$ or $-V_{dc}/2$ referring to the mid-point of dc bus as ground. Original CM voltage is defined as the average of the AC terminal line to dc-link mid-point voltages [13]. Thus, the CM voltage at the inverter side is calculated as:

$$V_{cm0} = \frac{V_{a0} + V_{b0} + V_{c0}}{3} \tag{1-1}$$

where V_{cm0} is the original CM voltage and V_{a0}, V_{b0} and V_{c0} are the terminal line to dc-link mid-point voltages. The CM voltage is a high-frequency pulsed step waveform which varies with the switching frequency. Fig. 1-3 and Fig. 1-4 illustrate eight operating states of PWM control and their corresponding CM voltage levels. Sometimes, the terminal CM voltage is defined as the average of the AC terminal line to ground voltages [14].
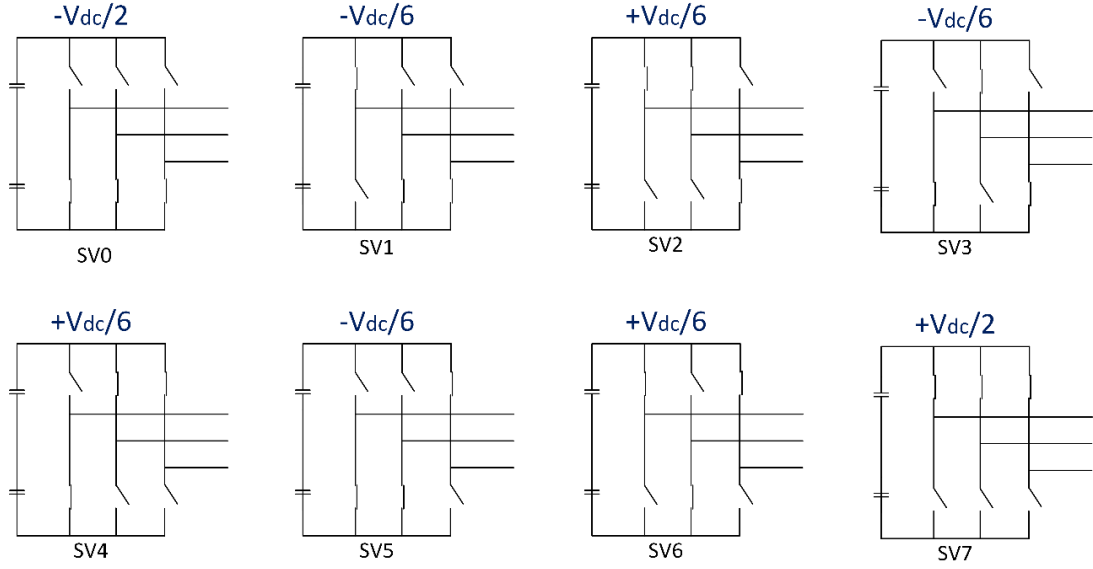
Fig. 1-3 Eight switching states of PWM operation
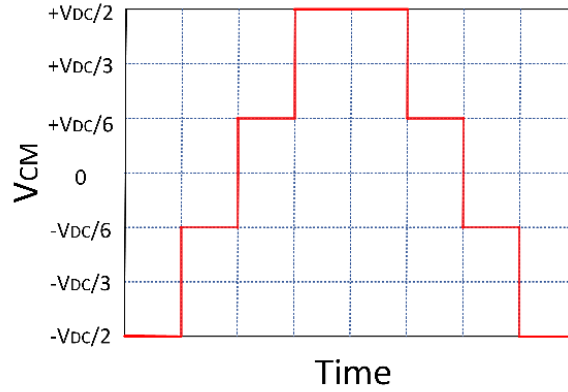
Fig. 1-4 CM voltage waveform

The CM current that is caused by the high-frequency CM voltage is defined as the average of phase currents flowing from the inverter to the induction motor. The total CM noise current passes through the whole bundle of the three-phase power cable and returns to ground. Thus the CM current per phase is one-third of the total CM current:

$$i_{cm} = \frac{i_a + i_b + i_c}{3} \tag{1-2}$$

Fig. 1-5 illustrates the basic structure of a motor bearing, consisting of inner and outer bearing races and bearing balls. The inner race of the bearing is mounted on the motor

shaft with low-impedance solid contact. The outer race is stuck in the frame which is grounded. The bearing impedance is capacitive in nature due to the lubricating film or grease around the rolling elements. For the CM path, the two motor bearings are practically connected in parallel. Once the bearing voltage exceeds a specific threshold level, both bearings will discharge through the compromised bearing, which is commonly called electrical discharge machining (EDM) [15].
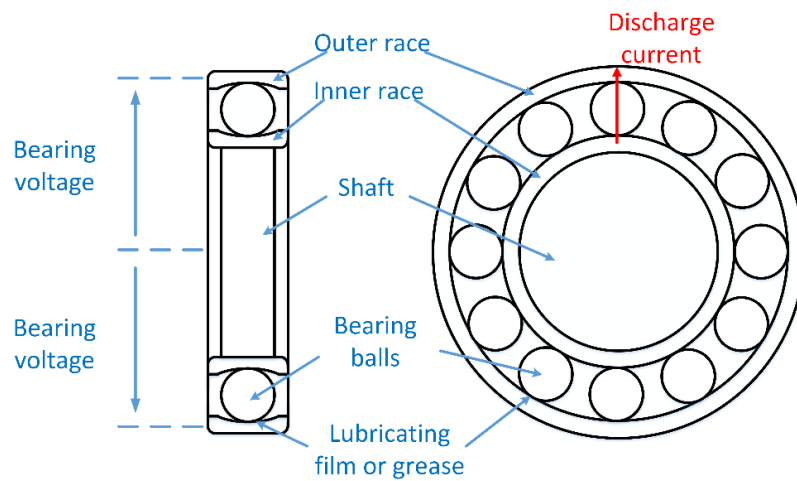
Fig. 1-5 Structure of a motor bearing

1.3   Motor drive systems in the marine application

In contrast to conventional Terra-N (TN) and Terra-Terra (TT) system where the neutral is always grounded, naval ships always use ungrounded insulated terrestrial (IT) power networks to provide better reliability [8], as shown in Fig. 1-6. In an IT system, live phases and the distributed neutral are all floating, i.e. not connected to ground, so that if one phase is shorted to ground, it will not cause then overcurrent protection device to activate. The protection device will only operate when a second insulation breakdown arises in another phase.
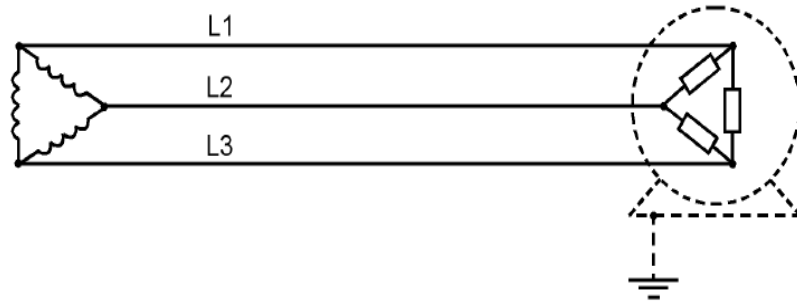
Fig. 1-6 Insulated terrestrial power system.

In the case of a single-phase fault, the presence of large line-to-ground filter capacitors will induce a high leakage current which poses safety hazards to humans. Thus, there is an upper limit on the line-to-ground capacitance in the filter, commonly known as the Y capacitors. The power level of induction motors in the marine application can be as high as several MW or even higher, which translates into multi-core power cables for the motors. These cables are too rigid to be bend and therefore the number of turns for a CM inductor has been constrained. Usually, multi CM inductors in series are necessary to achieve large enough CM inductance in marine applications. Therefore, design of an optimized CM filter for marine application to provide sufficient attenuation can be challenging due to many design constraints.

Also, the mechanism of bearing degradation for MW motors may be different from those with smaller power due to their relatively large stray capacitance. For large motors, simply grounding the motor shaft is not an effective solution, as part of the overall ground current can still pass through the bearings as rotor ground current and damages the bearings within a very short time.

1.4   Motivation

As both the CM voltage and current are characterized by their high-frequency spectral content, proper modelling of the electric motor concerned is essential in identifying the CM current path behavior so that the most effective methods for the reduction of CM current can be adopted. With proper equivalent circuit models, time-domain simulations for both single- and three-phase induction motors allows one to understand the mechanism of bearing degradation in greater depth so that correct mitigation techniques can be applied for the reduction of bearing current.

The subject of bearing failure has been studied extensively and there are three main mitigation methods for bearing degradation: a) Mitigation at the source end (the inverter side), such as soft switching method or advanced pulse width modulation (PWM) techniques [16-19], b) Mitigation between the source and load ends (the interconnecting power cable), such as CM filters at DC or AC side [14, 20, 21] and c) Mitigation at the load end (the motor side), such as insulated motor bearings, shaft grounding rings and Faraday shield [22-25]. For a large number of inverter-driven induction motors that have already in use in the industries, using CM filter is more convenient, economical and maintenance-friendly as compared with the other two mitigation methods.

Most filters available in the market have their filter attenuation measured based on 50 Ω resistive source and load terminations [26]. However, the termination of a CM filter in an inverter-driven motor system is far from 50 Ω. Hence, the filter attenuation given in the specification based on 50 Ω terminations may not work well under the actual operating environment. To design a CM filter that is effective for a specific operating

condition, the actual CM termination impedances must be known. The CM load(motor) impedance can be measured offline as the motor speed has little impact on the CM motor impedance over the mid-to-high frequency range [27]. Online extraction of the CM motor impedance is also possible based on the spectrums of CM voltage and CM current [28]. As for the CM source (inverter) impedance, one could consider estimating it from offline measurement or simply assume some typical values, but such estimates are not reliable because the noise source impedance under actual operating conditions can be very different[29, 30]. The in-circuit impedance extraction based on an inductive coupling approach seems to be a viable method by injecting a high-frequency excitation to the CM loop and monitoring the same signal simultaneously [31], but the presence of significant background noise in high power motor drive systems cause poor signal-to-noise ratio (SNR) to enable reliable and accurate extraction of in-circuit impedance. Therefore, an improvement over the existing approach is necessary for the in-circuit impedance measurement of high power inverter-fed motor drive systems [32].

1.5   Organization of Thesis

This thesis is organized as follows:

This chapter provides the introduction, background and motivation of the thesis.

Chapter 2 gives a review of the bearing degradation issues for inverter-fed motor drive systems and commonly adopted mitigation methods. The causes of bearing voltage and four types of bearing currents are described in detail for the readers to appreciate the

remaining chapters of the thesis. In addition, existing methods to measure and extract the noise source impedance of a converter are also reviewed.

Chapter 3 explains the development of equivalent circuit models of single- and three-phase motor drive systems to enable in-depth study and analysis of the CM current propagation paths. A controlled switch is designed to emulate the EDM process in the motor bearings. Then, a 5.5 kW motor drive system is chosen for the test setup to investigate the bearing degradation experimentally, as well as to evaluate various mitigation techniques.

Chapter 4 describes the proposed improvements done on an existing inductive coupling method to extract the in-circuit noise source impedance of a motor drive system. The improvements enhance the SNR of the measurement setup and protect the measurement instruments from transient events. The method with the improvements is verified experimentally and then applied to the 5.5 kW prototype for the actual in-circuit impedance extraction.

Chapter 5 describes a systematic design process of a first-order CM choke filter based on the extracted noise source impedance. Firstly, two critical frequencies are selected to give a quick estimate of the filter performance based on an analytical approach and then comprehensive modeling using finite element method (FEM) is performed to extract the CM choke's parameters. Then, the performance of a second-order LC CM filter is evaluated and the mode conversion of the second-order filter is studied quantitatively.

Chapter 6 concludes the thesis and discusses possible future work which is worth exploring further.

Chapter 2 Literature Review

2.1 Bearing degradation problem

To mitigate the bearing degradation problem effectively, the first step is to understand the mechanism behind the causes of bearing degradation. The terminology of bearing voltage ratio (BVR) is introduced to connect between the CM voltage and bearing voltage. In general, the bearing currents can be sub-divided into four categories and two of them are held responsible for premature bearing failures.

2.1.1 Motor capacitances and bearing voltage ratio

To analyze the CM current propagation paths, a motor side CM voltage source is placed between the stator windings and the motor frame, as shown in Fig. 2-1. The stray capacitances inside the induction motor are usually negligible at the differential-mode (DM) line-operation of 50 Hz or 60 Hz. However, from CM perspective at higher frequencies, the effects of the stray capacitances cannot be ignored and must be taken into consideration. The four most critical stray capacitances are explained as follows [33, 34]：

- C_{wf}: stator winding-to-frame capacitance. It is the lumped capacitance between the stator winding and the motor frame. As the dominant capacitor in the CM current loop, C_{wf} is the largest among all the other stray capacitors inside the induction motor. Its value depends on the winding insulation, winding placement, the geometry of the winding slot and the power rating of the motor.

- C_{wr}: stator winding-to-rotor capacitance. It is the sum of the stray capacitances between parallel conducting plates and the rotor, whose value depends on the length of the rotor, the width of the conducting plates and the air gap of the motor.

- C_{rf}: rotor-to-frame capacitance. Its value depends on the surface area of the rotor, the surface of the stator iron stack and the separation distance between them.

- C_b: bearing capacitance. It is a dynamic capacitance during the operation of the induction motor. When the motor speed is high enough (roughly larger than 100 rpm) [35], the lubrication film, which is regarded as insulating material, covers the full surface of motor bearings, making the bearing a capacitor with the capacitance C_b. At lower motor speed, the lubrication film does not cover the whole surface of bearing and there exists some metal contact between bearing balls and races.
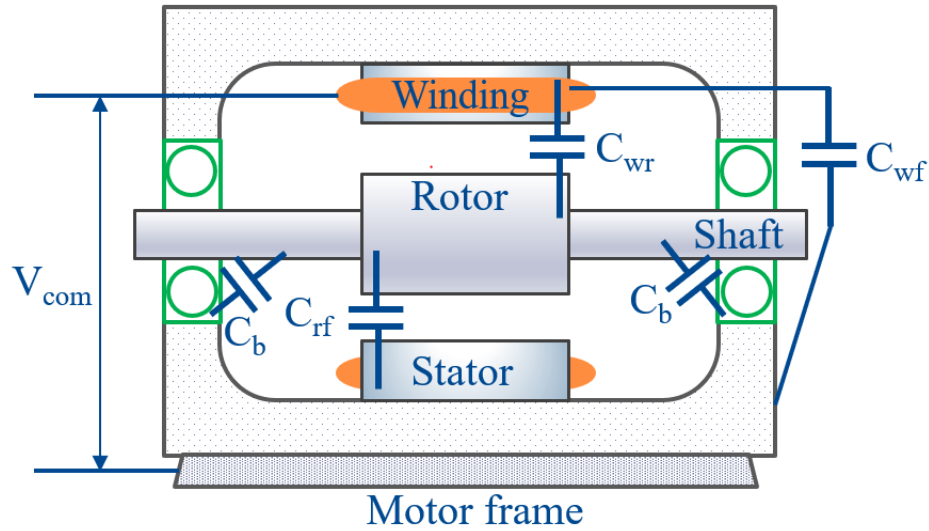
Fig. 2-1 CM voltage across the stator winding and frame

When the lubrication film of the bearing is intact, the stator winding-to-frame capacitance C_{wf}, stator winding-to-rotor capacitance C_{wr}, rotor-to-frame capacitance

C_{rf} and the bearing capacitances at the drive end $C_{b,DE}$ and opposite drive end $C_{b,ODE}$ will form a capacitive voltage divider as shown in Fig. 2-2 and equation (2-1). Therefore, the bearing voltage or the shaft voltage mirrors the CM voltage at the motor terminal with a ratio defined as "bearing voltage ratio (BVR)" [36, 37].
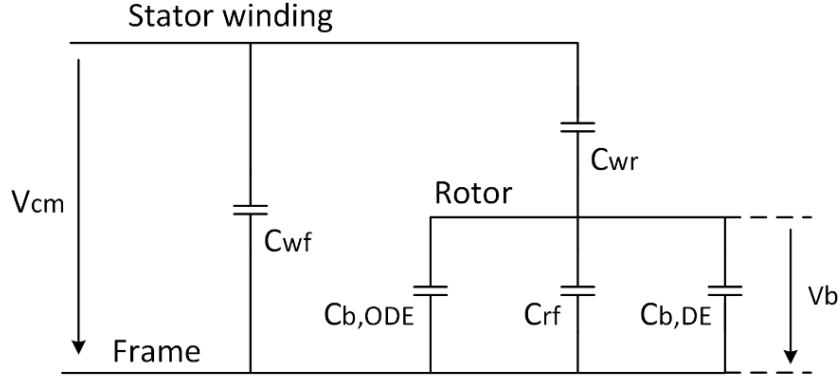
Fig. 2-2 Equivalent circuit of motor stray capacitances

$$BVR = \frac{shaft\ voltage}{CM\ voltage} = \frac{C_{wr}}{C_{b,ODE} + C_{b,DE} + C_{rf} + C_{wr}} \qquad (2\text{-}1)$$

2.1.2   Bearing current categories

A voltage-source inverter (VSI) used in a VFD presents a high-frequency CM voltage source and the CM voltage of an inverter is never zero under sinusoidal pulse width modulation. Large and fast variation of the CM voltage stresses the motor terminals and couples with the motor stray capacitors which are of no influence at line frequency. Capacitive couplings from stator windings to the ground creates multiple bearing current routes [35]. Four types of inverter-induced bearing currents are induced as shown in Fig. 2-3 and their flowing paths are illustrated in Fig. 2-4 and Fig. 2-5.
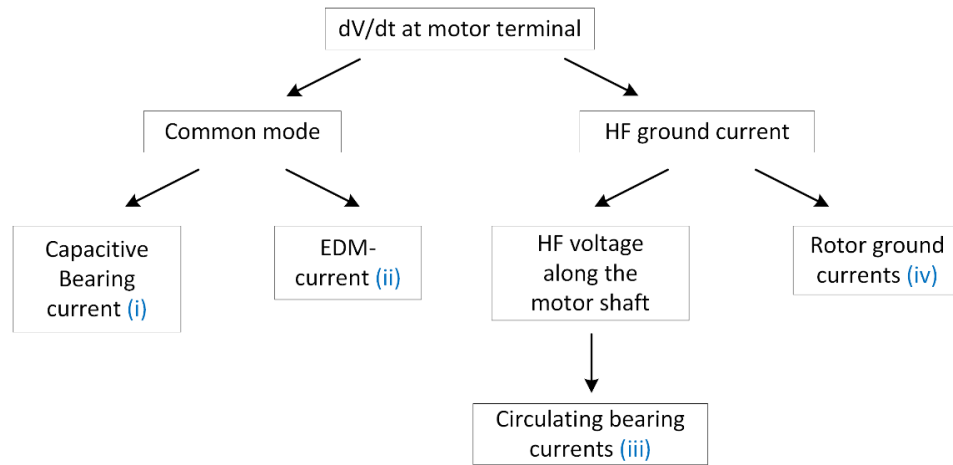
Fig. 2-3 Bearing current of inverter-driven induction motors
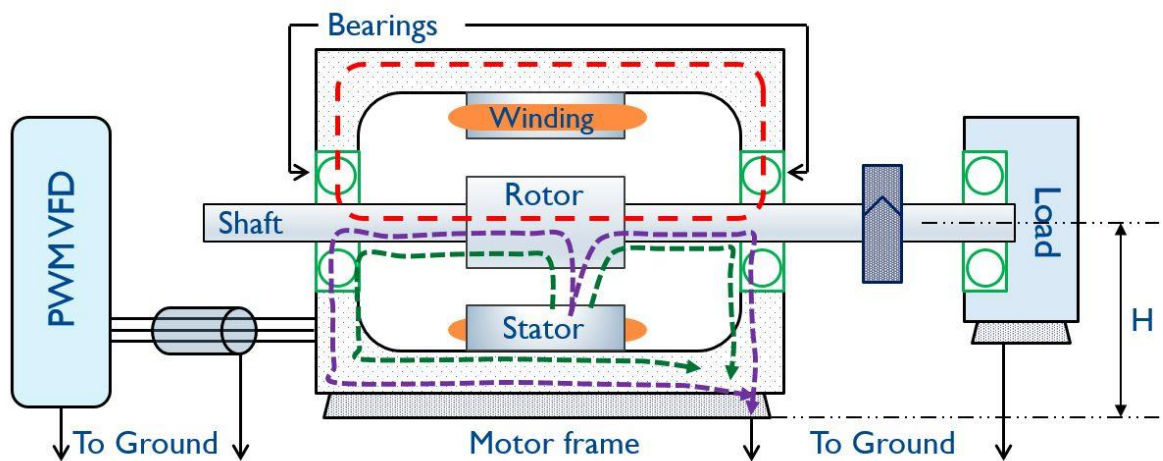
Fig. 2-4 Bearing currents loops inside an induction motor (type i, ii and iii)
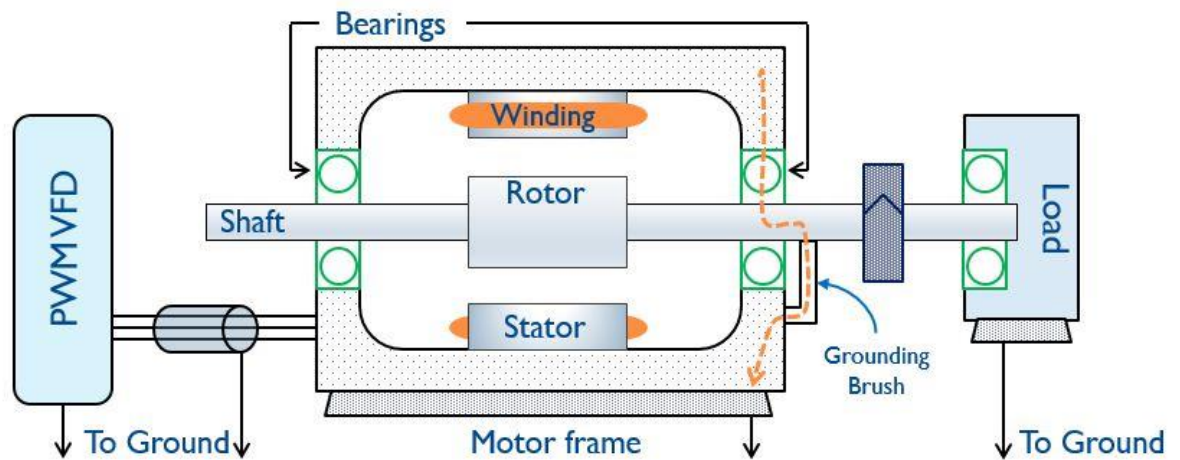
Fig. 2-5 Bearing currents loops inside an induction motor (type iv)

i. Capacitive bearing current:

Bearing voltage mirrors the shaft voltage at low bearing temperature (25 °C) and high rotating speed (over 100rpm) due to the voltage divider rule. The bearing voltage thus has a similar waveform as the CM voltage shown in Fig. 1-4 with high *dv/dt*. The *dv/dt* across the intact bearing causes a small capacitive bearing current in the range of a few milliamperes, which can be obtained with (2-2). The capacitive bearing current loop is illustrated in Fig. 2-4 with the green dashed line, from the stator winding to the motor frame via intact bearing lubrication.

$$i_b = C_b \frac{dv_b}{dt} \tag{2-2}$$

Bearing balls and bearing races may have metallic contact at low rotating speed or elevated bearing temperature, making the bearing an ohmic resistance. Then, the bearing voltage causes a small bearing current usually with amplitude less than 200 mA.[35]

Compared with other bearing currents, the capacitive bearing current has relatively smaller amplitude and not contributes to the bearing degradation. Thus this bearing current is not discussed any further.

ii. Electric discharge machining (EDM) current:

As mentioned before, bearing voltage mirrors the CM voltage and can be written as:

$$v_b = v_{cm} \cdot BVR = v_{cm} \cdot \frac{C_{wr}}{C_{b,ODE} + C_{b,DE} + C_{rf} + C_{wr}} \tag{2-3}$$

The low-frequency to medium-frequency components of the bearing voltage stress bearing balls which are surrounded by thin lubrication film with low dielectric strength. Lubrication film may breakdown when the bearing voltage exceeds a certain discharge threshold voltage. The energy in both bearing balls (capacitors) will be released instantly,

resulting in arcing over the bearings and the races. Consequently, melted and vaporized crates are produced in the bearing raceway, as shown in Fig. 2-6 [38].
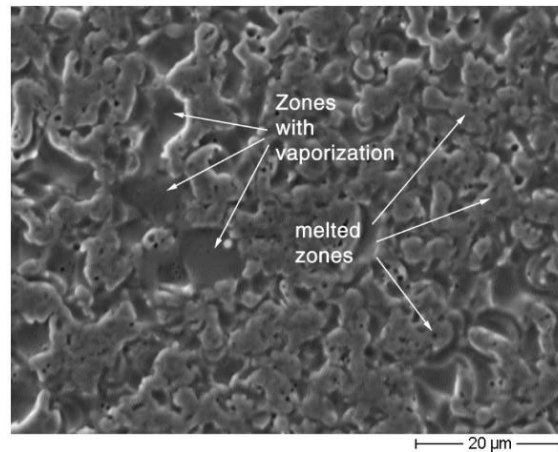
Fig. 2-6 Melted and vaporized crates

EDM current path is illustrated with the violet dashed lines in Fig. 2-4. Although EDM current has the same current path as the capacitive bearing current, its peak amplitude can reach a few amperes and is the dominant cause of bearing degradation for small-sized motors.

iii. Circulating bearing current:

The current flows through the winding to the rotor is the source of capacitive bearing current and EDM current, while the current from the winding to the stator is the source of circulating bearing current [39]. To facilitate the understanding of circulating bearing current, the grounding current flowing axially through the stator winding will be briefly introduced. Fig. 2-7 illustrates the physical structure of the embedded copper coil and its per-phase equivalent circuit.
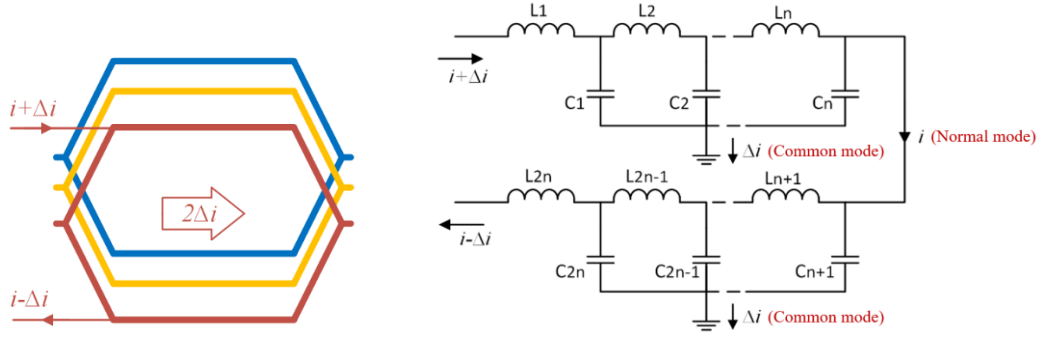
Fig. 2-7 Physical structure of the copper coil and per phase equivalent circuit

C_1, C_2…. C_{2n} are winding-to-frame stray capacitances between each winding and the motor frame. The ground represents the motor frame that is usually connected to ship hull. These capacitances provide paths for the flow of CM current to ground. L_1, L_2… L_{2n} are the inductances of each winding of the stator. Hence, Fig. 2-7 is a full equivalent circuit model to describe the stator winding and the motor frame. When a current of $i+\Delta i$ flows into the stator winding input, part of the current ($i-\Delta i$) flows out of stator winding back to the source and the rest flows to the ground via the winding-to-frame stray capacitances. In other words, for each phase, there is a total leakage current of $2\Delta i$. This noise current propagates from line to ground is considered as common-mode (CM) current. The propagations of normal-mode (NM) or differential-mode (DM) current and CM current are clearly indicated in Fig. 2-7. The CM current flows from line to ground through the winding-to-frame stray capacitance and the DM current flows through the windings between the phases and has no direct interaction with the winding-to-frame stray capacitance. The flow of the leakage current in the stator coil is shown in Fig. 2-8. Assuming parasitic capacitors are distributed in the conductor uniformly, current entering the stator winding will be dissipated to the frame through the parasitic capacitances. For any given position Y_n in the Y-axis, stator winding current at both coil

side can be expressed as $i+\Delta in$ and $i-\Delta in$, respectively. The current distribution in the coil thus can be illustrated as Fig. 2-9.
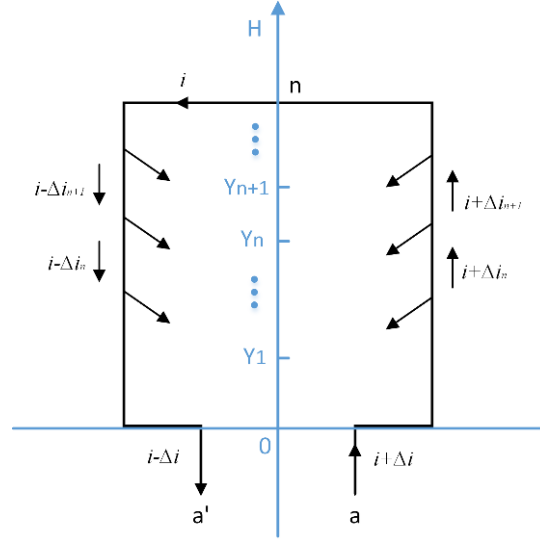
Fig. 2-8 Flow of current in the stator winding
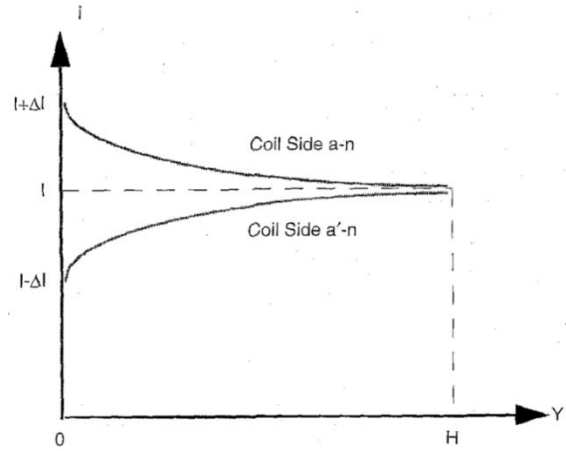
Fig. 2-9 Current distribution in the stator winding

The net leakage current that flows through the stator windings in the axial direction equals to:

$$\sum i = [(i_a + \Delta i_a) - (i_a - \Delta i_a)] + [(i_b + \Delta i_b) - (i_b - \Delta i_b)] \\ + [(i_c + \Delta i_c) - (i_c - \Delta i_c)] = 2(\Delta i_a + \Delta i_b + \Delta i_b) \qquad (2\text{-}4)$$

$\sum i$ is enclosed by a Gauss surface Φ inside the stator case as shown in Fig. 2-10, the cross-section of the motor in the radial direction. By Gauss' Law, there exists a time-varying magnetic flux surrounding the motor shaft, and this flux will induce an end-to-end shaft voltage [39]. If this shaft voltage exceeds the threshold voltage of the lubrication film, the bearing insulation property will be destroyed, and consequently the shaft voltage will cause a harmful circulating bearing current. The flux in the motor and the paths of circulating current are illustrated in Fig. 2-11.
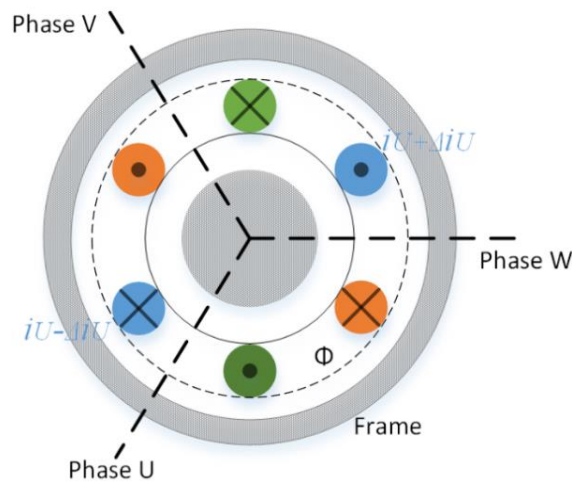
Fig. 2-10 Gauss surface inside the stator case
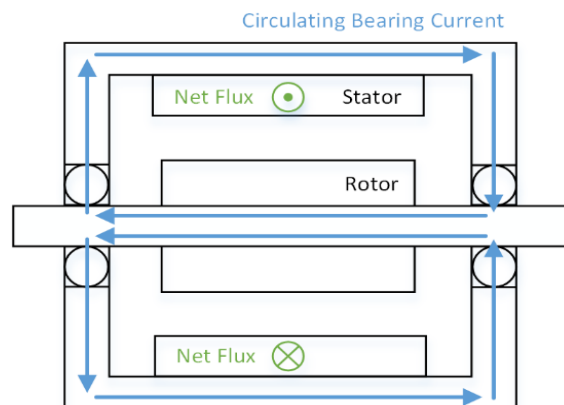
Fig. 2-11 Flux in the motor and circulating bearing current

The circulating bearing current can also be thought as the result of the transformer effect [40]. In this case, the motor can be considered as a transformer where the CM leakage current acts as a primary and induces the circulating current flowing through the shaft or secondary. Equivalent transformer circuit is shown in Fig. 2-12.
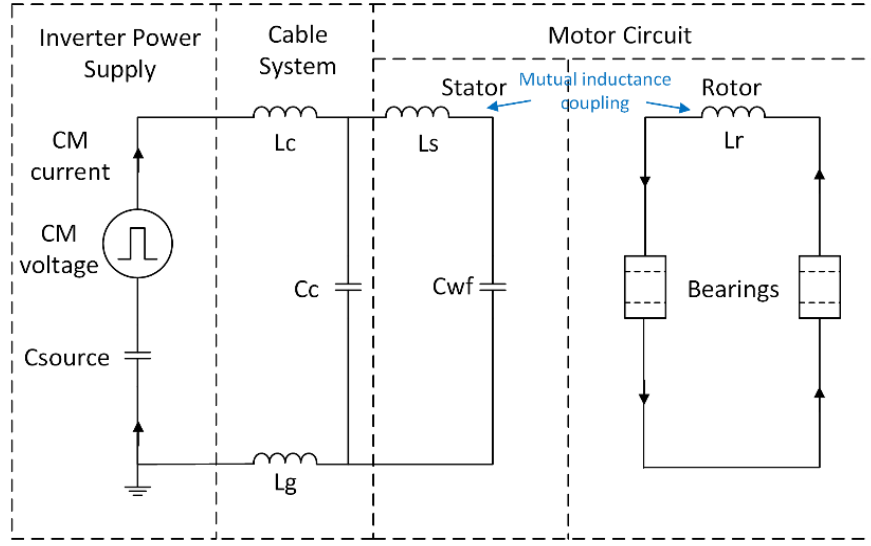
Fig. 2-12 Transformer effect causing the circulating bearing current

The amplitude of the circulating current strongly depends on the shaft length and the high-frequency ground current. The former one is proportional to the frame size and the later one is proportional to the stray capacitance between stator winding and the frame. Distance between the stator winding and the frame does not change much with the motor size but the area of overlap is proportional to the square of the motor frame size. Therefore, the flow of circulating bearing current increases with the cube of the motor frame size [35], i.e.

$$v_{end-to-end} \sim i_g l_{shaft} \sim (Size)^2(Size) = (Size)^3 \qquad (2\text{-}5)$$

iv. Rotor ground current [9]:

The use of grounding brush reduces the shaft voltage with respective to the grounded motor frame and hence, eliminates the occurrence of the EDM bearing currents. However,

if the rotor is connected to the ground with significantly lower impedance than the stator frame grounding impedance, part of the overall ground current will flow through the bearing as the rotor ground current. The rotor ground current path is illustrated with the dashed line in Fig. 2-5. Also, the grounding brush adds to the existing circulating bearing current, which can be significant for large motor size and cause premature damage to the bearing. The bearing without grounding brush or the one at the no-load side may suffer from a higher circulating current.

To sum up, bearing current of type i is considered as harmless no matter the motor size. The current of types ii, iii and iv are potential threats to the motor bearings. Rotor ground current can be avoided by using ungrounded shaft or insulated coupler. The electrical motors are usually MW level in the marine propulsion system, so the circulating bearing current is more dominant than the EDM current. Mechanism of the harmful bearing currents is summarized in Fig. 2-13.

Electrostatic discharge machining (EDM) Current	$\Rightarrow$	$\dfrac{V_b}{V_{com}} = \dfrac{C_{WR}}{C_{WR}+C_{RF}+2C_B}$
Circulating bearing current	$\Rightarrow$	Due to high-frequency stator ground current
Rotor ground current	$\Rightarrow$	Due to high-frequency stator ground current and grounded rotor

Fig. 2-13 Mechanism of harmful bearing currents

2.2   Mitigation Techniques

2.2.1   Outline of mitigation

People are looking at the bearing degradation problem from two perspectives: the inverter end and the motor end. Many different mitigation techniques at both ends have been proposed to deal with the bearing degradation problem. Some well-known methods are briefly listed as follows,

1. To address the EDM bearing currents [41-43]

    - Inverter End

        1)   Passive filter at inverter side: sine filter, *dv/dt* filter, etc.

        2)   Active filter

        3)   Soft-switching technique

    - Motor End

        1)   Passive filter at motor side: shunt filter

        2)   Grounding brush or ground ring

        3)   Insulated motor bearings or insulated bearing seats

        4)   Hybrid bearings

        5)   Conductive lubrication grease

        6)   Faraday shield

2. To address the CM current and the circulating bearing current [22, 44-48]

    - Inverter End

        1)   Passive filter at inverter side: CM filter, etc.

        2)   Active filter

3)   Advanced modulation strategies

- Motor End

1)   Grounding filter at motor side

2)   Insulated motor bearings or insulated bearing seats

In general, *dv/dt* filters, sine filters and CM filters are mitigation techniques that can reduce the bearing currents but their effectiveness depends strongly on the type of bearing current that is of interest to suppress.

1. The EDM bearing current

In a motor drive system with short cable where the overvoltage is low, the EDM bearing currents generated in the motors are unaffected by all three types of filters because they do not eliminate the CM voltages. Hence, the voltage buildup in the bearings remains unchanged [9]. The sine filter leads to nearly sinusoidal line-to-line voltages, but not sinusoidal line-to-ground voltages.

For a motor drive system with electrically long cable, i.e., the physical length is comparable to the wavelength of the frequency of the analysis, voltage reflection can occur at the motor end if the motor's characteristic impedance is much higher than the cable's characteristic impedance. Under this situation, the *dv/dt* or sine filters can help reduce the overshoot of the CM voltage and further reduce the consequent EDM events.

2. The circulating bearing current

For larger motors with higher power ratings, the bearing current is dominated by the CM circulating current. Under such situation, the CM filters are more effective to reduce the CM circulating currents than the *dv/dt* or sine filters. This is because the CM filters

can provide high CM impedance at high frequency. Therefore, most commercially available filters always add a separate CM filter to their sine filter products [49].

To deal with the CM current problems for a large quantity of inverter-driven induction motors which have already been used in industrial applications, passive CM filter is more convenient, economical and maintenance-friendly compared with other remedial actions. Thus, CM filter design and optimization will be the emphasis of this project.

2.2.2   Passive CM filter design method

An EMI filter suppresses the noise by providing the impedance mismatch between the filter and the propagation paths. The attenuation of an LC filter can be derived by the following procedures [50], considering the case of the source voltage $V_{source,CM}$, the source impedance $Z_{source,CM}$ and the load impedance $Z_{load,CM}$, as shown in Fig. 2-14(a) and (b). L_{CM} represents a CM choke or CM inductor while C_{YT} represents the sum of the Y capacitors.

(a)

(b)
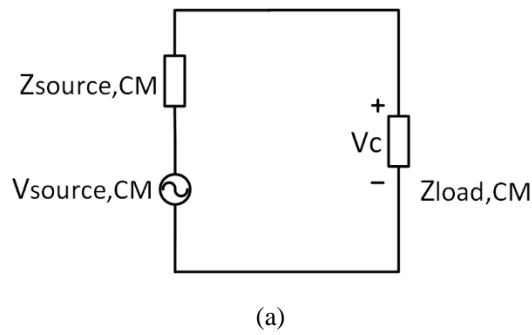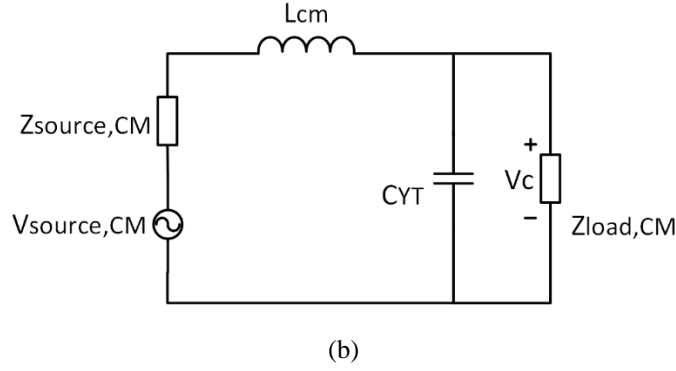
Fig. 2-14 Mismatched source and load without(a) and with(b) filter

1) Calculate the output voltage without the filter, V_o

$$V_o = \frac{V_{source,CM} Z_{load,CM}}{Z_{source,CM} + Z_{load,CM}} \qquad (2\text{-}6)$$

2) Calculate the output voltage with filter, V_c

$$V_c = \frac{V_{source,CM} Z_C Z_{load,CM}}{\left(Z_{source,CM} + Z_{load,CM}\right)\left(Z_C + Z_{load,CM}\right) + Z_C Z_L} \qquad (2\text{-}7)$$

3) Calculation the attenuation as $20\log\left(V_o/V_c\right)$

4) Following the above procedures give the result for attenuation

$$A_{dB} = 20\log\left|\frac{\left(Z_{source,CM} + Z_{load,CM}\right)\left(Z_C + Z_{load,CM}\right) + Z_C Z_L}{\left(Z_{source,CM} + Z_{load,CM}\right) Z_C}\right| \qquad (2\text{-}8)$$

Commonly used filter topologies are summarized in Fig. 2-15 and Fig. 2-16 [51]. As long as knowing the source impedance and the load impedance, attenuation of certain EMI filter under certain frequency can be calculated following the same steps.

Zload / Zsource	High	Low
High		
Low		
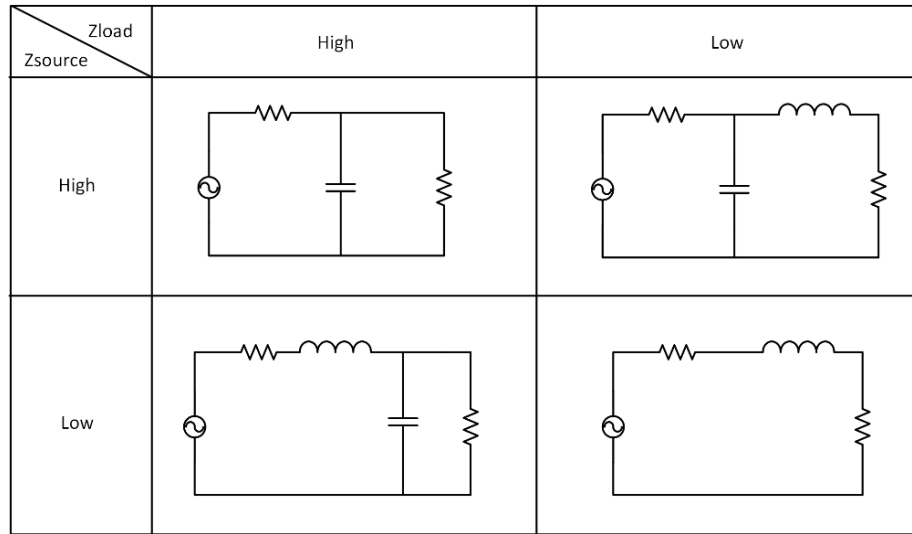
Fig. 2-15 First order and second order filter topologies

Zload / Zsource	High	Low
High		
Low		
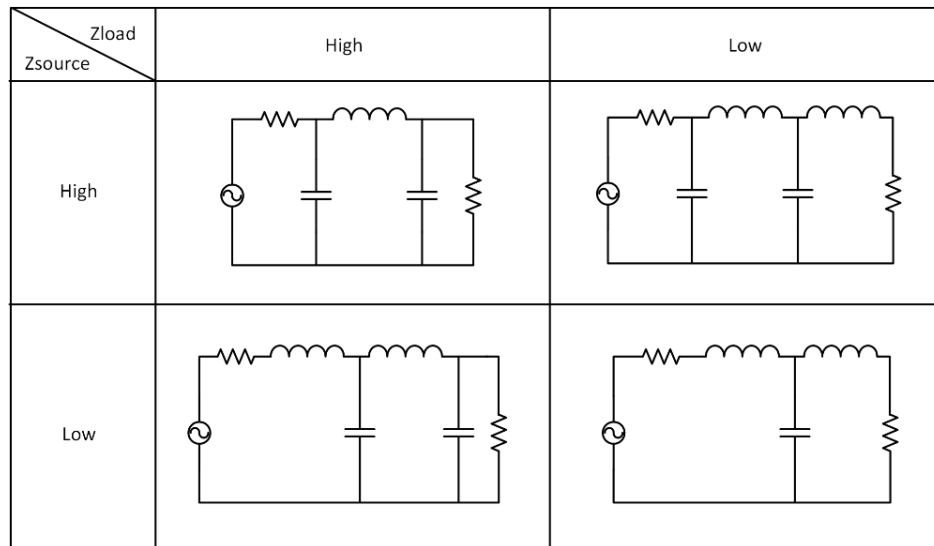
Fig. 2-16 Higher order filter topologies

For the load impedance, the military considers the worst-case environment by using a 10 µF feedthrough capacitor with 15 mΩ series resistance. This capacitor provides the worst-case low impedance and through which the current is measured [26].

Another condition for the EMI filter design is that the mains is considered as a load. Mains impedance under a variety of situations has been examined and the results show that the mains impedance is dynamic [52]. Hence in the interest of test repeatability, a

line impedance stabilization network (LISN) is put between the EMI source and the

dynamic load to develop a stable load impedance, as shown in Fig. 2-17.
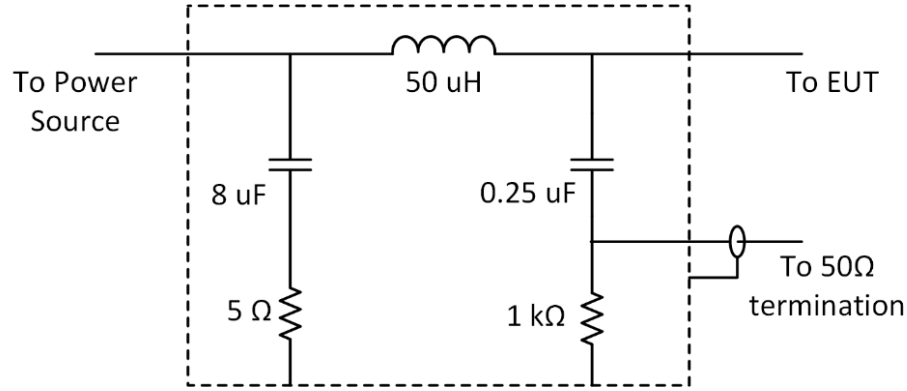
Fig. 2-17 LISM schematic of MIL-STD-461F

In the motor drive system, the load faced by the CM filter is a three-phase cable and

an induction motor, whose impedance can be measured offline with an impedance

analyzer.

Source impedances in communication and microwave applications are usually well

defined as 50 Ω but things are different when it comes to the motor drive system. The

noise source of an EMI filter for an inverter is unfortunately not readily available. One

could consider estimating this value from off-line measurement or simply assume some

typical values, but such estimates are not reliable because the noise source impedance

under actual operating conditions can be very different. Therefore, online extraction of

the source impedance of an inverter is necessary for the optimal EMI filter design.

2.3   Impedance extraction methods

Through a comprehensive literature review, existing online impedance measurement

technique includes the resonance method [51], the inductive coupling approach [53], and

the ABCD network approach [31, 54]. In this section, these three approaches are reviewed, and their merits and shortcomings are discussed.

2.3.1 The resonance method

The resonance method is a way to determine the source impedance of a black box. Physically, there is an insulation layer between the electronic devices and the grounded heat sink and chassis, which is capacitive in nature. Therefore, the black box is assumed to be a Norton circuit with a capacitive source impedance. Insight into the source impedance can be obtained by cleverly choosing the load impedance and examining the resonance between the source and load. Conceptual schematic of the resonance method is shown in Fig. 2-18.
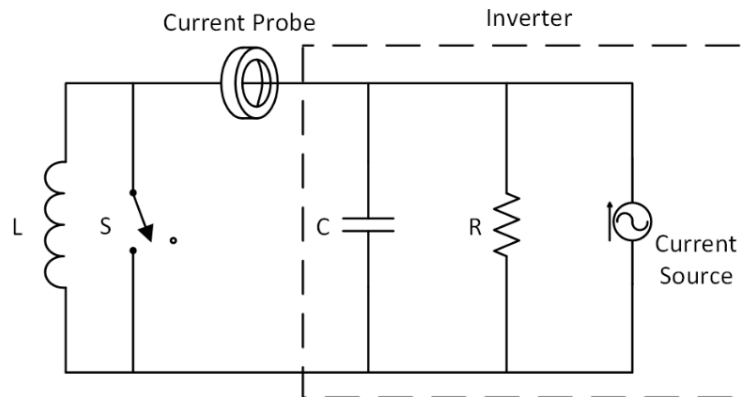
Fig. 2-18 Conceptual schematic of the resonance method

The value of the current source can be directly measured using a current probe by shorting the load. Then connect the noise source to an inductive load to create a resonance at certain frequency and the Q of the source may be found at this frequency. The Q of the source is defined as

$$Q = \frac{I_L}{I_{sc}} \tag{2-9}$$

where I_{sc} is the short circuit current, and I_L is the current when the inductive load resonates with the source impedance.

Q can be also used to calculate the resistive and capacitive components of the noise source

$$R = \omega L Q \tag{2-10}$$

$$C = \frac{Q}{\omega R} \tag{2-11}$$

where R is the source resistance, L is the load inductance, C is the source capacitance and ω is the resonant frequency.

Although the resonance method can extract the source impedance under operating condition, it is different from the real working environment. The load of the system needs to be replaced by a known inductor to introduce the resonance, which means the interruption of the normal operation of the induction motor. For the CM source impedance measurement, the short circuit is achieved via large capacitors between phases and the ground, causing the change of resonant frequency and adding to the source capacitance. Besides, large leakage current could be a potential threat to personal safety. Q is calculated by the short circuit current and the inductive load current under the same frequency. Therefore, it may take efforts and a long time to choose load inductance by trial and error method and find a resonant frequency where the short circuit current at this frequency point is pronounced and stable.

The noise source in the measurement is considered to be capacitive, which is realistic at low frequency before the equivalent series inductance (ESL) of the stray capacitance

becomes dominant. After hitting the resonant frequency, the source impedance behaves like an inductor, thus the resonance method may not be able to capture the resonance point and fail to estimate the source impedance at high frequency.

2.3.2 The inductive coupling approach

The inductive coupling approach has been developed to determine the CM noise source impedance of a switched mode power supply (SMPS) which allows the online impedance measurement without interrupting the normal operation of the system. The idea of this approach is to inject a high-frequency signal into the system via an injecting probe and obtain the loop impedance by comparing the injected signal and the received signal. The concept of this method and its equivalent circuit is illustrated in Fig. 2-19 and Fig. 2-20.
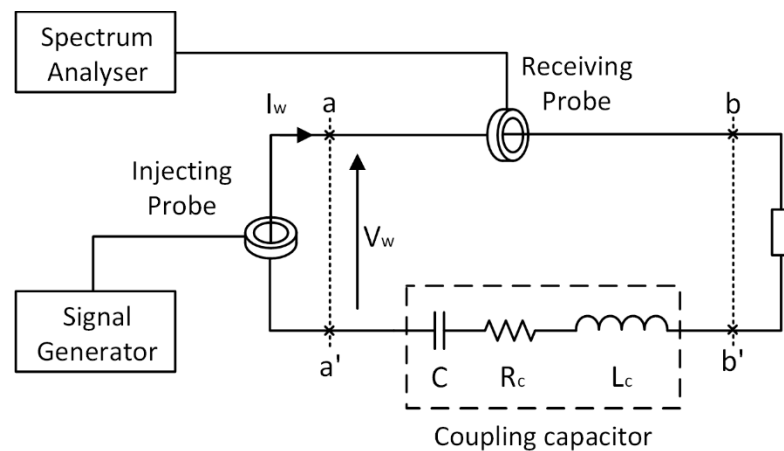
Fig. 2-19 Basic setup of the two probes approach
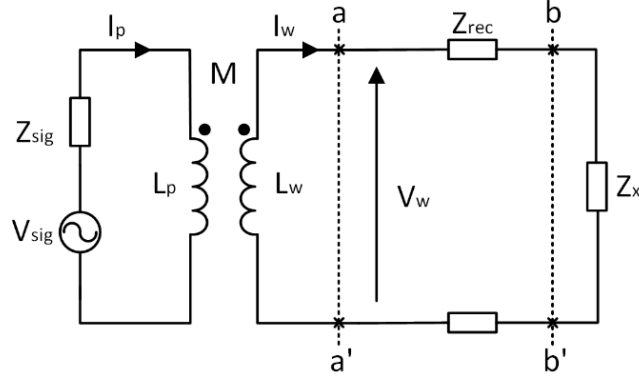
Fig. 2-20 Equivalent circuit of the two probes approach

The radio frequency (RF) coupling circuit for the impedance measurement consists of two current probes and one coupling capacitor. Injecting probe and receiving probe clamped on the cable are connected to signal generator and spectrum analyzer respectively. Injecting probe at a-a' works as a transformer whose ratio is N:1. Self-inductances of the primary side and secondary side are denoted by L_p and $L_w$while the mutual inductance between the injecting probe and the wire loop is M. Output voltage and output impedance of signal generator are presented as V_{sig} and Z_{sig}. Induced voltage and current into the system at the secondary side of the transformer are presented as V_w and I_w. The relationship between source voltage and induced voltage can be illustrated as:

$$V_w = \frac{j\omega M V_{sig}}{Z_{sig} + j\omega L_p} - (j\omega L_w - \frac{j\omega M}{Z_{sig} + j\omega L_p})I_w \tag{2-12}$$

(2-12) can be simplified as:

$$V_w = V_M - Z_M I_w \tag{2-13}$$

$$V_M = \frac{j\omega M V_{sig}}{Z_{sig} + j\omega L_p} \tag{2-14}$$

$$Z_M = j\omega L_w - \frac{j\omega M}{Z_{sig} + j\omega L_p} \tag{2-15}$$

where V_M and Z_M are the equivalent source voltage and source impedance.

The impedance of DUT can be obtained by

$$Z_x = \frac{V_M}{I_w} - (Z_M + Z_{rec} + Z_c) \qquad (2\text{-}16)$$

The current in the wire loop I_w is measured by the receiving probe

$$I_w = \frac{V_p}{Z_T} \qquad (2\text{-}17)$$

where V_p is the voltage measured by the receiving probe and Z_T is the transfer impedance of the receiving probe.

Substituting (2-15) and (2-17) into (2-16)

$$Z_x = \frac{j\omega M V_{sig}}{Z_{sig} + j\omega L_p} \frac{Z_T}{V_p} - (Z_M + Z_{rec} + Z_c) \qquad (2\text{-}18)$$

Then (2-18) can be simplified as

$$Z_x = \frac{k V_{sig}}{V_p} - Z_{in} \qquad (2\text{-}19)$$

where $k = \frac{j\omega M Z_T}{Z_{sig} + j\omega L_p}$ and $Z_{in} = Z_M + Z_{rec} + Z_c$. In (2-19), $k V_{sig}$ and Z_{in} are both constant coefficients for a given frequency. $k V_{sig}$ can be determined by replacing the load with a large standard resistor $R_{std} \gg |Z_{in}|$, thus

$$k V_{sig} \approx R_{std} V_p|_{Z_x = R_{std}} \qquad (2\text{-}20)$$

To obtain Z_{in}, Z_x is replaced with a short circuit and is calculated as:

$$Z_{in} = \frac{k V_{sig}}{V_p} \qquad (2\text{-}21)$$

Finally, the impedance of DUT can be determined by (2-21) with known $k V_{sig}$ and Z_{in}.

The most attractive feature of the inductive coupling approach is that the current probes can avoid direct electrical contact to the electrical system. Although the conventional inductive coupling approach can extract the source impedance online, the setup in Fig. 2-19 must be carefully calibrated with the power source disconnected. Thus, this method will not interrupt the operation of the system during measurement, but the system has to be stopped for calibration, which may not be feasible if the system is mission critical. For calibration, the device under test (DUT) is first replaced by a known standard precision resistor and then a short circuit. However, for many practical applications, the DUT cannot be easily replaced due to either the size or inaccessibility.

Output frequency of the signal generator is fixed during the measurement so that the measured impedance of DUT is also under certain frequency, which is not enough to show the impedance change with frequency. One possible way is to repeat the measurement for different frequency points, but it also means time-consuming work. Another way is to use the two-port ABCD network approach with a vector network analyzer (VNA) for frequency sweep.

2.3.3 Two-port ABCD network approach

In this method, the inductive coupling probes and the electrical system are treated as three cascaded two-port networks. By obtaining the ABCD parameters of the electrical system, the loop impedance can be calculated with ease. Basic setup of the two-port ABCD network approach and its equivalent circuit consisting of two-port networks are shown in Fig. 2-21 and Fig.2-22, respectively.
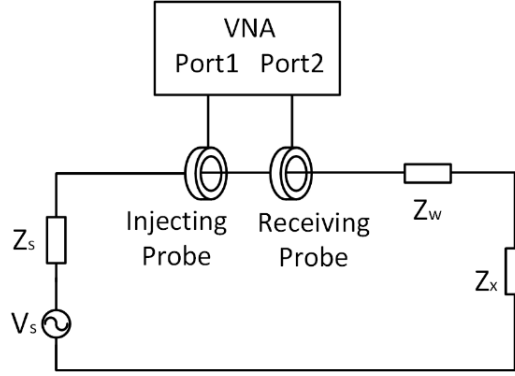
Fig. 2-21 Basic setup of two-port ABCD network approach
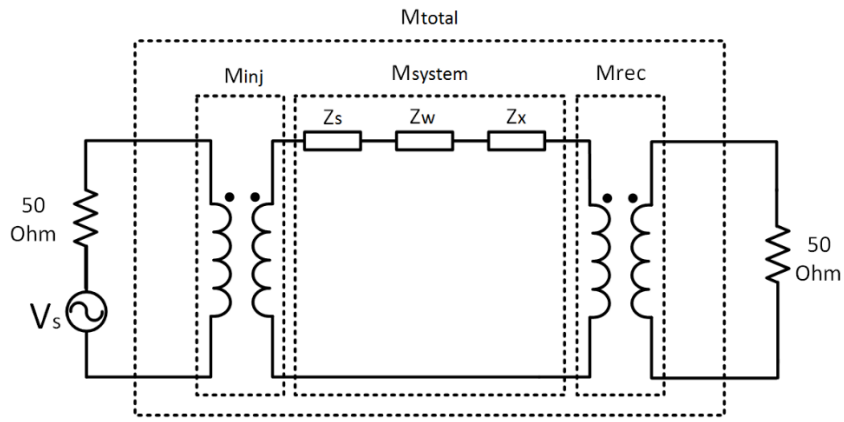
Fig. 2-22 Equivalent circuit of two-port ABCD network approach

Here V_s is the power source of the electrical system whose internal impedance is Z_s. Z_w is the impedance of the wiring connection. Z_x is the impedance of the electrical system under actual operating conditions.

Through two clamp-on type current probes, an RF signal is injected from VNA's port 1 to the circuit loop and then is detected at VNA's port 2. Each current probe, one as injecting probe and another as receiving probe, can be treated as a transformer and represented by a two-port network, as shown in Fig. 2-22, named as M_{inj} or M_{rec}.

M_{system} represents the two-port network consisting of the electrical system, the power source, and the wiring connection. The injecting probe, receiving probe and the electrical

system are modeled as three cascaded two-port networks. M represents the equivalent two-port network between port 1 and port 2 which can be characterized by the VNA and expressed as

$$\begin{bmatrix} A & B \\ C & D \end{bmatrix} = \begin{bmatrix} A & B \\ C & D \end{bmatrix}_{inj} \begin{bmatrix} A & B \\ C & D \end{bmatrix}_{system} \begin{bmatrix} A & B \\ C & D \end{bmatrix}_{rec} \qquad (2\text{-}22)$$

where $\begin{bmatrix} A & B \\ C & D \end{bmatrix}$, $\begin{bmatrix} A & B \\ C & D \end{bmatrix}_{inj}$, $\begin{bmatrix} A & B \\ C & D \end{bmatrix}_{system}$ and $\begin{bmatrix} A & B \\ C & D \end{bmatrix}_{rec}$ are the ABCD parameters

of M, M_{inj}, M_{system}, and M_{rec}, respectively.

M_{inj} and M_{rec} can be first characterized with the VNA and the test fixture before the actual in-circuit impedance measurement, thus the unknown ABCD parameters of M_{system} can be obtained through (2-22) as well as Z_{system}, which is the sum of Z_x, Z_s and Z_w.

Two-probe network approach has the ability to extract in-circuit impedance of the noise source by injecting a high-frequency excitation to the CM loop, but it has limitations when applied to a high-power motor drive system. First, the background noise in a motor drive system can be very high due to the fast switching of IGBTs or MOSFETs, so the signal-to-noise ratio of the measuring device is far from enough. On the other hand, the high-frequency noise could exceed the receive limitation of the VNA and damage the measurement ports. Therefore, an improved method suitable for the high-power systems is strongly desired.

Chapter 3   Investigation of premature bearing degradation

This chapter introduces the time domain simulation of both single- and three-phase induction motors driven under PWM operation. Besides, a prototype using a 5.5 kW motor drive system is built as a case study to investigate the bearing degradation and evaluate various mitigation techniques. To make the simulations considerably more realistic, parameters in the models are obtained from either measured results or published papers. Comprehensive modeling of the 5.5 kW induction motor is accomplished with a three-phase universal model and the process of electrical discharge machining is emulated by a voltage-controlled switch.

3.1   Single-phase induction motor driven by a CM voltage source

The advantage of single-phase equivalent circuits is that they avoid the complexity of three-phase circuits by ignoring the differential mode behavior of the system while providing a useful insight into the motor's CM behavior. In the CM viewpoint, all the three phases can be considered as one single conductor as the CM current is the average of three-phase currents and the CM voltage is one-third of the total voltage.

3.1.1 Circuit model of the single-phase equivalent circuit

The single-phase equivalent model of a motor drive system is represented in Fig. 3-1 with a motor zero sequence impedance and a capacitive voltage divider [55].
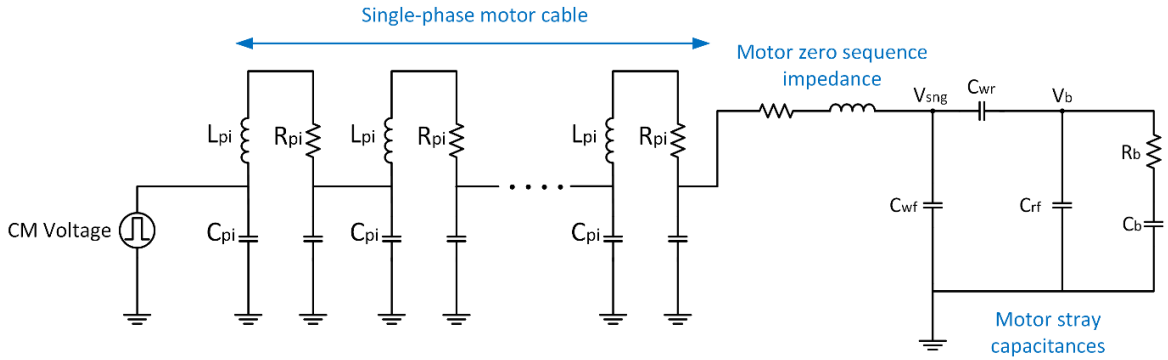
Fig. 3-1 Single-phase motor driven by a CM voltage source

A piecewise linear source is used in the circuit to present the CM voltage at the output terminal of a 2-level voltage source inverter whose value is one-third of the sum of phase-to-ground voltages. The inverter uses sinusoidal PWM with a modulation index of 0.8 and a switching frequency of 3 kHz.

The motor zero-sequence impedance is one-third of the stator resistance in series with one-third of the stator leakage inductance. The zero-sequence impedance for the 15 kW motor is adopted from [1], 300 µH and 59.8 Ω. Stray capacitances in the motor include the winding-to-frame capacitance (C_{wf}), winding-to-rotor capacitance (C_{wr}), rotor-to-frame capacitance (C_{rf}), and the bearing lubrication capacitance (C_b). R_b is the bearing resistance in series with the bearing capacitance. V_{sng} and V_b in Fig. 3-1 are the stator neutral-to-ground voltage and the bearing voltage respectively. The 5 m single-phase cable is connected between the CM source and the motor. It can be represented by cascaded lumped Pi electrical model with subsection length $\varDelta L$. For each lumped Pi sub-

section, the resistance R_{pi}, the inductance L_{pi} and the capacitance C_{pi} can be calculated by using the per unit length distributed parameters multiply by $\varDelta L$. For the given power cable, the per unit length distributed parameters are 160.28 mΩ/m, 163 nH/m and 124 pF/m, respectively.

3.1.2 Simulation results for a single-phase induction motor

In the simulation, the cable length is 5 m and the rise time of the CM voltage source is 30 ns. Fig. 3-2 compares the CM voltage (top plot) and the neutral-to-ground voltage (bottom plot) for the 15-kW motor. The CM voltage is a step waveform with the values of $+V_{dc}/2$, $+V_{dc}/6$, $-V_{dc}/2$ and $-V_{dc}/6$ and the neutral-to-ground voltage has a similar waveform. As shown in Fig. 3-2, the CM voltage has a fundamental frequency of 3 kHz. The stator's neutral-to-ground voltage exhibits considerable overshoot due to the impedance mismatch between the motor and the cable. From the viewpoint of differential mode, a single inverter switching event may cause up to double the dc bus voltage at the motor terminal, while for common-mode, the overvoltage can achieve 2/3 of the dc link voltage. In the simulation, the largest overvoltage caused by the 5 m cable and the 15 kW motor is as high as 35% of the CM voltage.
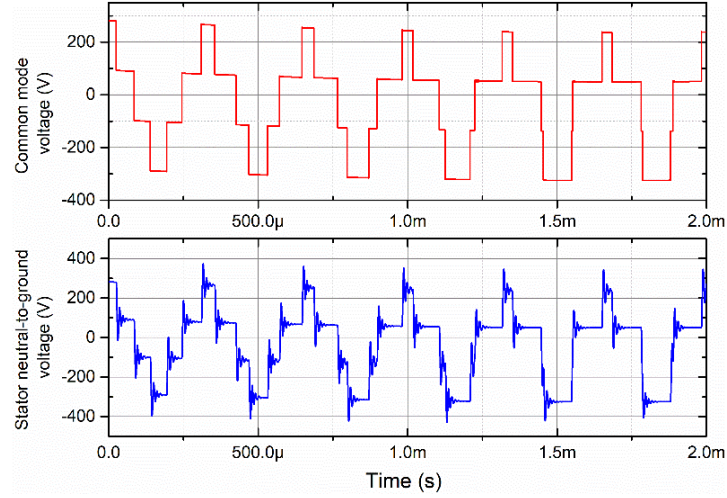
Fig. 3-2 CM voltage and neutral-to-ground voltage

Of all the parasitic capacitances in Fig. 3-1, C_{wf} is the largest one and dominates the motor CM impedance. The effect of C_{wf} on the bearing voltage is shown in Fig. 3-3.
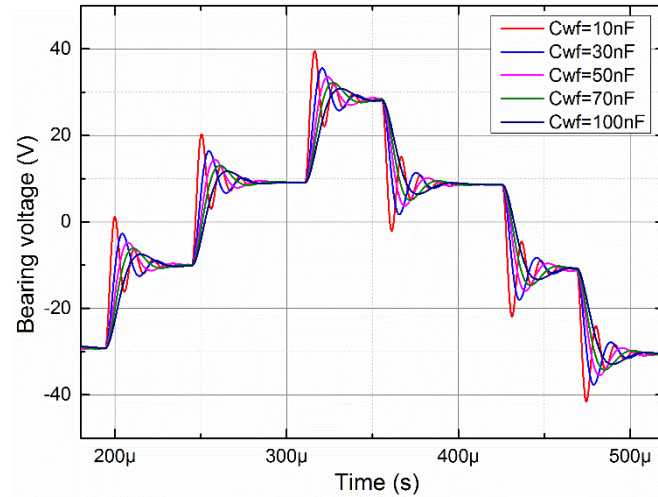
Fig. 3-3 Effect of the stator-winding capacitance on the bearing voltage

The variation of the bearing voltages is generated by sweeping the value of C_{wf} from 10 nF to 100 nF while keeping the values of C_{wr}, C_{rf}, C_b and R_b constant. Provided the bearing impedance is insulating, bearing voltage which is also the rotor-to-ground voltage mimics the neutral-to-ground voltage because of the voltage divider rule. As shown in Fig. 3-3, the steady bearing voltage for each switching operation is constant for

all the conditions. For an intact motor bearing, the steady state voltage is not affected by the change of C_{wf} as the BVR of the motor is calculated in (3-1) when neglecting R_b.

$$BVR = \frac{C_{wr}}{C_b + C_{rf} + C_{wr}}$$

(3-1)

Note that C_{wf} has a rounding-off effect on the bearing voltage in that the dv/dt of bearing voltage and overshoot decreases with increasing C_{wf}.
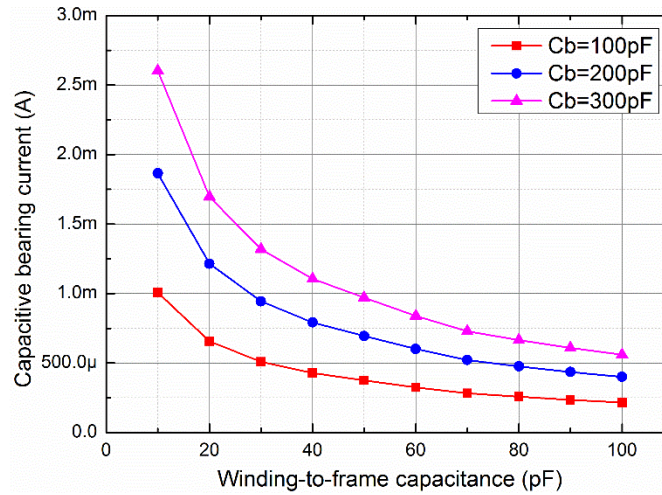
Fig. 3-4 Maximum capacitive bearing currents

If the motor bearing insulation is not punctured, a small capacitive bearing current will flow through the bearing whenever the CM voltage transitions from one level to another. The maximum capacitive bearing current for different bearing capacitances is calculated in Fig. 3-4. Larger bearing capacitance means smaller bearing impedance, thus resulting in a higher capacitive bearing current. However, as shown in Fig. 3-4, the capacitive bearing current is negligible for all three values of C_b. Although the bearing current can attain values of 2.5 mA or even higher with larger bearing capacitance, it is still considered to be too small a current to cause permanent bearing damage.

An actual ball bearing impedance is a nonlinear function of the motor and lubrication parameters and it also depends on the operating condition of the motor, temperature of the environment and the aging degree of the grease, so that the threshold voltage of the motor bearing is dynamic and irregular, which means the bearings can randomly alternate between insulating and conducting states[1].

3.2 Three-phase induction motor driven by a 2-level voltage source inverter

In this section, a high-frequency simulation of a three-phase 5.5 kW motor is presented for the study of the CM voltage and CM current. Since the bearings can alternate between insulating and conducting states at random, a controlled switch is designed to simulate this transition of bearing impedance from one state to another, so that it is possible to examine the variation of bearing voltage and the EDM current that flows through the compromised bearing.

3.2.1 Determination of motor parameters

A well-known IEEE 122 per-phase T-equivalent model is shown in Fig. 3-5 which can represent the low-frequency behavior (50, 60 and 400 Hz) of a three-phase induction motor. The IEEE 122 equivalent circuit is expressed simply in terms of the following components: stator resister and leakage inductance (R_s and L_{ls}), rotor resister (R_r), leakage inductance and slip (L_{lr} and s), magnetizing inductance (L_m) and core loss

(R_{core}). Parameters of a 6-pole TECO 5.5 kW induction motor in a Y-equivalent connection is listed in Table 3-1.
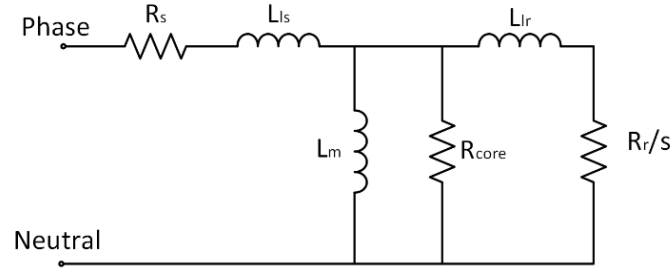
Fig. 3-5 IEEE 112 per-phase low-frequency equivalent model

Table 3-1 Parameter of 5.5 kW induction motor per phase (Y-equivalent)

	$s = 1$
R_s	0.89 Ω
L_{ls}	3.93 mH
R_r	0.91 Ω
L_{lr}	4.65 mH
L_m	102.94 mH
R_m	418.10 Ω

High-frequency response of the induction motor is hard to be achieved with the T-equivalent lumped circuit as the applied voltage is not uniformly distributed through the stator windings and the stray capacitances of the stator windings are not considered. Thus an improved universal model from [56] is adopted to simulate the high frequency behaviors of the induction motor by adding more stray parameters to the conventional model, as shown in Fig 3-6.
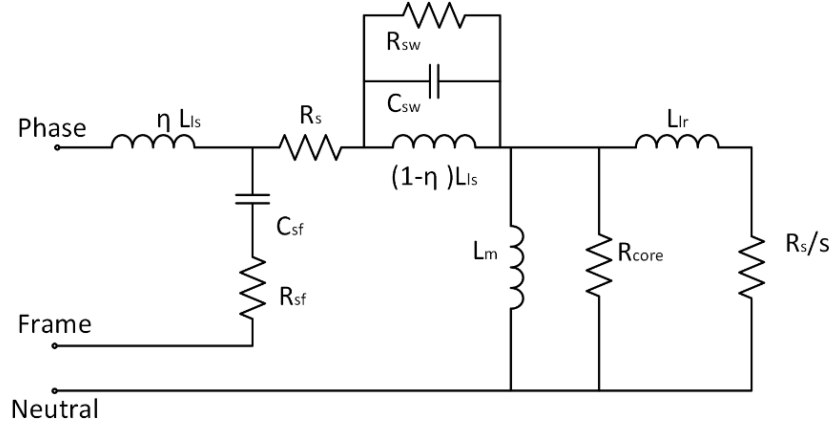
Fig. 3-6 Per-phase universal induction motor model

The leakage inductance of the stator winding is divided into two parts, ηL_{ls} for the first few turns and $(1 - \eta)L_{ls}$ for the rest coils because the high-frequency rise-time-related effects of the PWM voltage on the DM reflected voltage mainly depends on the first few turns at the first coil group. Effective winding-to-frame stray capacitance of the first few slots and resistance of this fraction of windings are denoted as C_{sf} and R_{sf}. R_{sw} and C_{sw} are the loss equivalent resistance and interturn winding capacitors of the stator coils. These additional components create a few resonances and anti-resonances in the motor's CM and DM frequency response, thus careful selection of these values can help to simulate the induction motor in a wider frequency range.

Equivalent Y-connection for the actual Δ-connection of the stator windings in a three-phase induction motor is shown in Fig. 3-7 where the neutrals of the three-phase circuit are connected together to the parasitic capacitors in the induction motor, C_{sf}, C_{sr}, C_{rf}, C_b and the series resistance of the motor bearings, R_b. L_f and R_f are the frame inductance and frame resistance from the slot to the ground reference point. A switch is placed across the bearing to simulate the EDM process when the bearing voltage exceeds the threshold value.
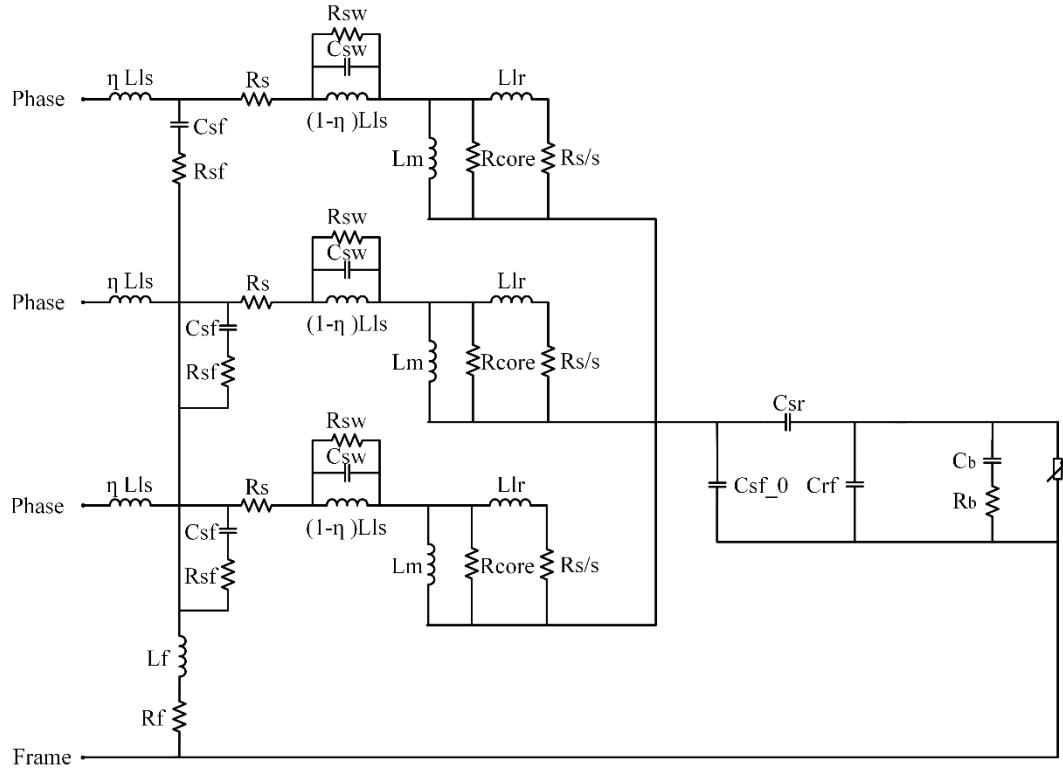
Fig. 3-7 Equivalent Y-connection for the actual Δ-connection of the stator windings in a three-phase induction motors

The following two impedance measurements are required to estimate the high-frequency parameters in the universal induction motor model as well as the stator and rotor leakage inductances.

- DM impedance of the motor

- The winding (one lead) to frame capacitance at low frequency and high frequency

The measurement setup and results for the 5.5 kW induction motor are shown in Fig 3-8 and Fig 3-9 and a few key points for the calculation of motor parameters are marked in the figure. The impedances are measured offline when the slip rate $s = 1$.
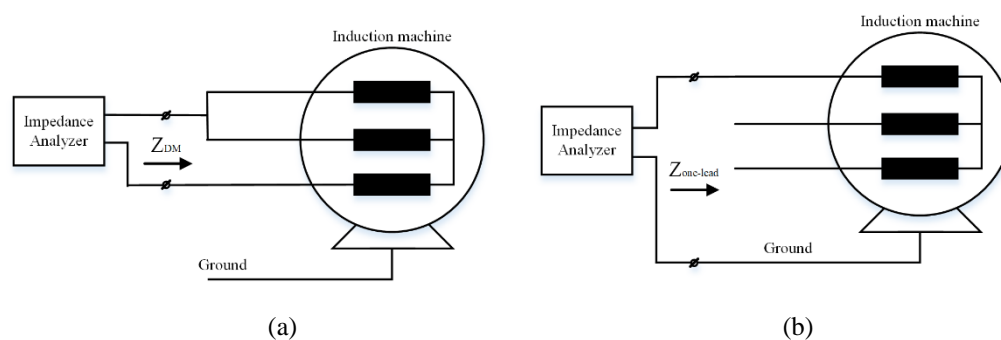
Fig. 3-8 Measurement setup (a) DM impedance; (b) one-lead-to-frame impedance
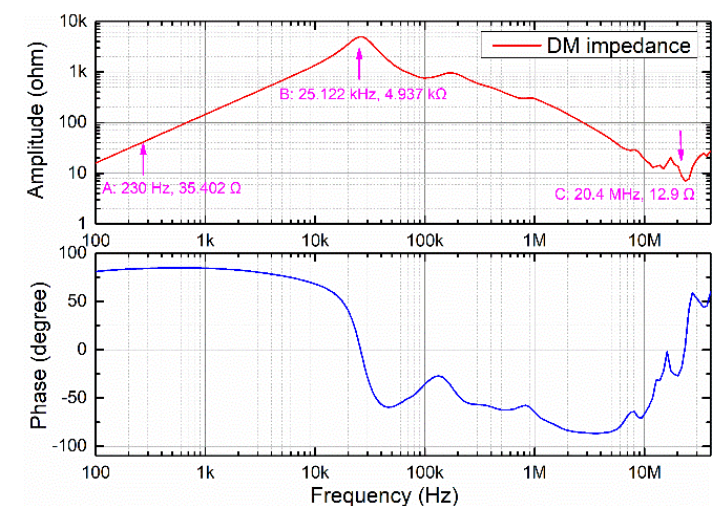
(a)
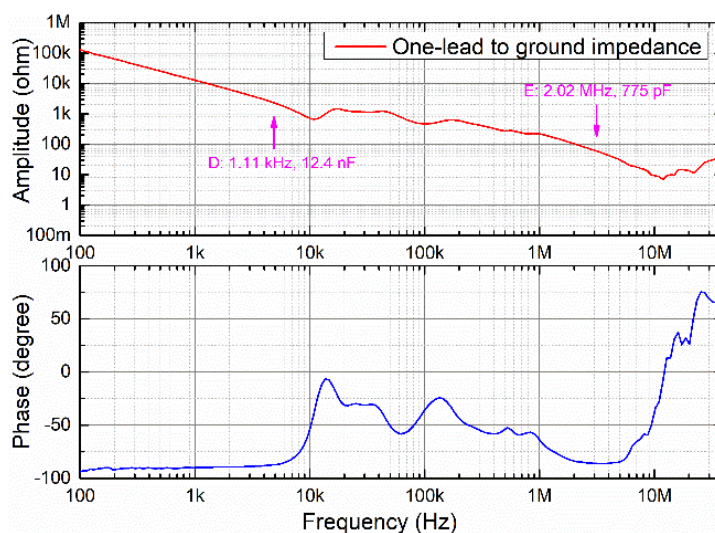
(b)

Fig. 3-9 Impedance measurement results of the 5.5 kW motor (a) DM impedance; (b) one-lead-to-frame impedance

The marked points (A)-(E) shown in Fig. 3-9 are used to estimate the high-frequency parameters of the induction motor according to equations (3-2) to (3-6). The selection of these marked points is summarized below and the measured results are given in Table 3-2.

(A) Frequency and the corresponding impedance magnitude where the impedance phase angle has its maximum value.

(B) Frequency and impedance magnitude at the first resonant point.

(C) Frequency and impedance magnitude at the anti-resonant point.

(D) The winding (one-lead) to frame capacitance at low frequency.

(E) The winding to frame capacitance at high frequency.

<div align="center">Table 3-2 Measured data of the 5.5 kW motor</div>

Steps	Magnitude (Ω)	Phase Angle (degree)	Frequency (Hz)
A	35.40	84.7	230
B	4937.02	6.4	25122
C	13.01	−26.0	20408017
D	102.17	−83.9	2021288
E	11566.03	−89.7	1111

$$C_{sw} = \frac{2(2\omega_r)^2 L_{ls} C_{sf} - 1}{(2\omega_r)^2 L_{ls}((2\omega_r)^2 L_{ls} C_{sf} - 1}$$ (3-2)

$$R_{sf} = \frac{2}{3}|Z|_{anti-r}$$ (3-3)

$$\eta L_{ls} = \frac{1}{C_{sf}(2\pi f_a)^2}$$ (3-4)

$$R_{sw} = \frac{2}{3}|Z|_{max} - |R_{core}//(j2\pi f_r L_{lr})|$$ (3-5)

$$C_{sf\_0} = C_{sf(LF,one-lead-to-frame)} - 3C_{sf(HF,one-lead-to-frame)} \qquad (3\text{-}6)$$

The bearing stray capacitances in the high-frequency model, i.e. C_{sr}, C_{rf} and C_b, are hard to be measured directly but can be estimated through experiential equations introduced in [1] or electromagnetic numerical methods, such as finite element method (FEM). However, both experiential equation estimation and electromagnetic numerical methods require the material property and exact geometry structure of the motor bearings, which are difficult to obtain without dismantling the motor. In the three-phase model, bearing stray capacitances of the 5.5 kW motor in Table 3-3 is determined based on the measured bearing voltage ratio and the calculated data from [1], as shown in Fig. 3-10.

Table 3-3 Estimated bearing parameters

Parameters	C_{sr}	C_{rf}	C_b	R_b
Value	50 pF	2.4 nF	300 pF	5 Ω
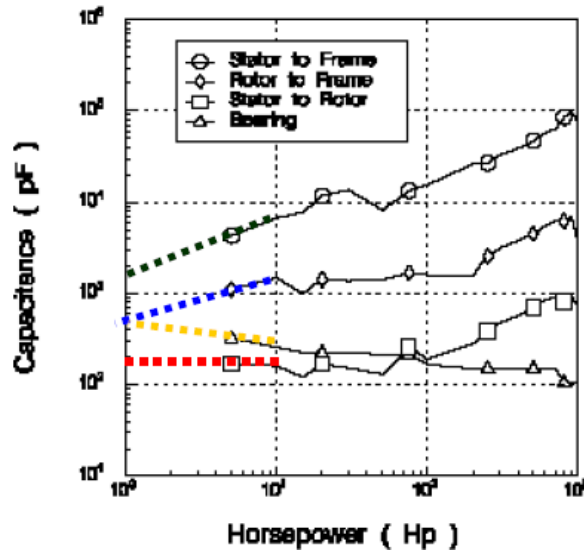
Fig. 3-10 Normalized Capacitances Curves until 1000Hp rated power motors [1]

With the low-frequency parameters from the data sheet in Table 3-1 and the obtained data points mentioned in steps (A) to (E) in Table 3-2, parameters for the high-frequency model of the 5.5 kW induction motor are then calculated and given in table 3-4.

Table 3-4 High-frequency parameters of the 5.5 kW induction motor

Parameters	C_{sw}	R_{sf}	nL_{ls}	R_{sw}	C_{sf_0}
Value	1 nF	8.66 Ω	78 nH	2896.08 Ω	10 nF

The measured and calculated DM and CM impedance of the 5.5 kW induction motor are demonstrated in Fig. 3-11. It has shown that the calculated results and the measured results are in good match with each other, particularly at the low- and high-frequency spans. The difference at mid-frequency around 100kHz is mainly due to the decrease in the magnetic core permeability, which leads to a significant decrease in the magnetizing inductance (L_m).
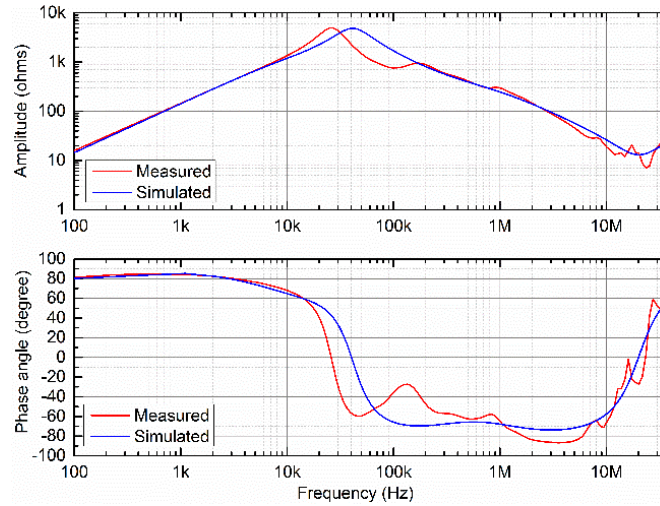
(a)
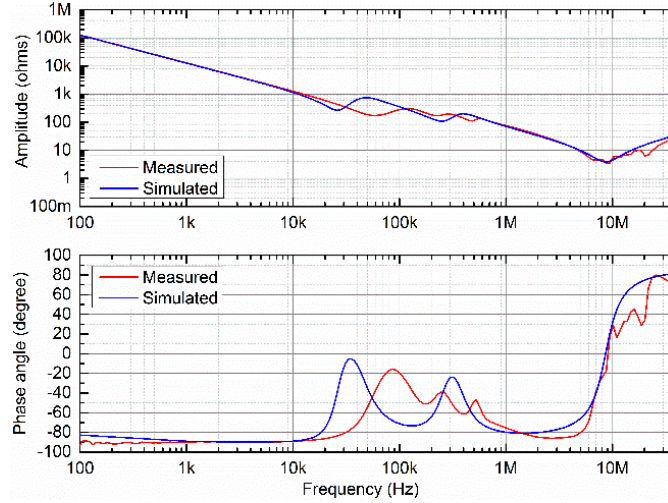
(b)

Fig. 3-11 Measured versus modeled impedance of 5.5 kW induction motor. (a) DM impedance (b) CM impedance

3.2.2 Determination of the cable parameters

Three-phase cable is modeled based on [57] to take care of the power loss in the transmission wire and the variation of the stray capacitor with frequency. Fig. 3-12 shows the distributed parameters per phase per *ft* of the power cable.
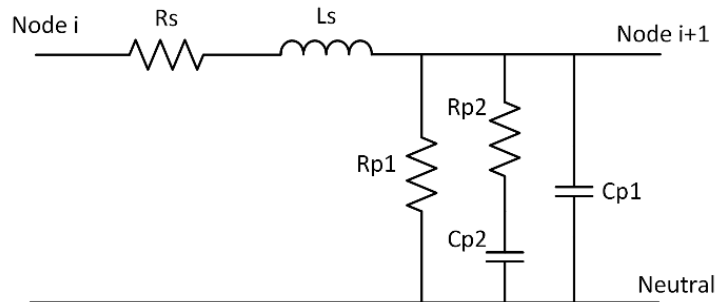
Fig. 3-12 Per-phase model of the power cable per-unit length

Parameters for the simulated cable are summarized in Table 3-5 and the model is validated by examining the cable characteristic, open- and short-circuit impedances as shown in Fig. 3-13.

Table 3-5 Distributed parameters (per ft) for a three-phase Beldon cable

Parameters	R_s	L_s	R_{p1}	R_{p2}	C_{p1}	C_{p2}
Value	2 mΩ	0.4 uH	48.01 MΩ	884.29 kΩ	13 pF	51 pF

(a)

(b)

(c)
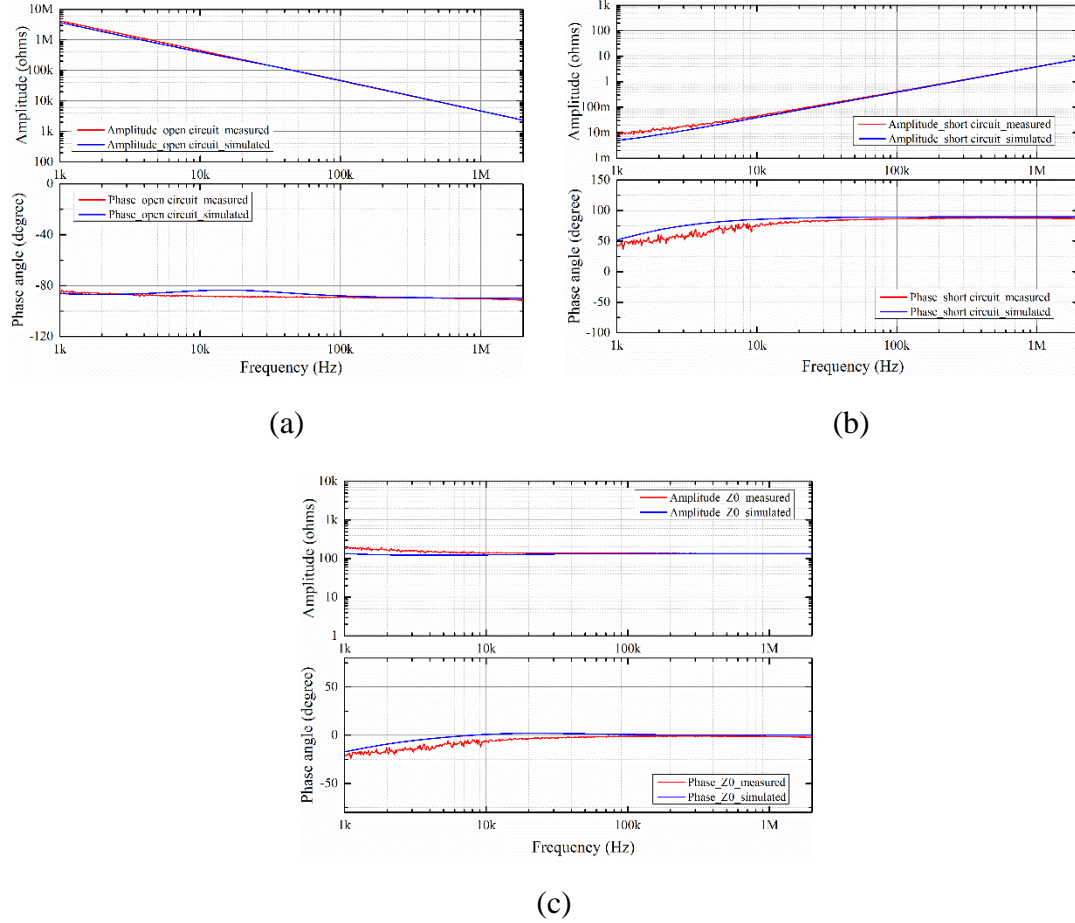
Fig. 3-13 Cable open- (a) and short- (b) circuit impedances and characteristic impedance (c)

3.2.3 Circuit model of the three-phase motor drive system

The three-phase simulation presented in this section involves a three-phase universal model for a 5.5 kW induction motor and 0.9-m long unshielded cable driven by a PWM 2-level voltage source inverter, as shown in Fig. 3-14. C_{p1}, L_s, C_{p2} and C_{p3} are the LCL filter connected between the power grid and the input of the commercial inverter. The two Y capacitors C_y, each of which is 2.5 nF, are mounted between the positive and

negative rails of the dc link and the grounded enclosure. C_h is the experimentally measured stray capacitances between the collector of each of the IGBTs (S1 through S6) and the enclosure. In the figure only the stray capacitor for S1 is shown to avoid clutter. All the parameters for the inverter are given in table 3-6.
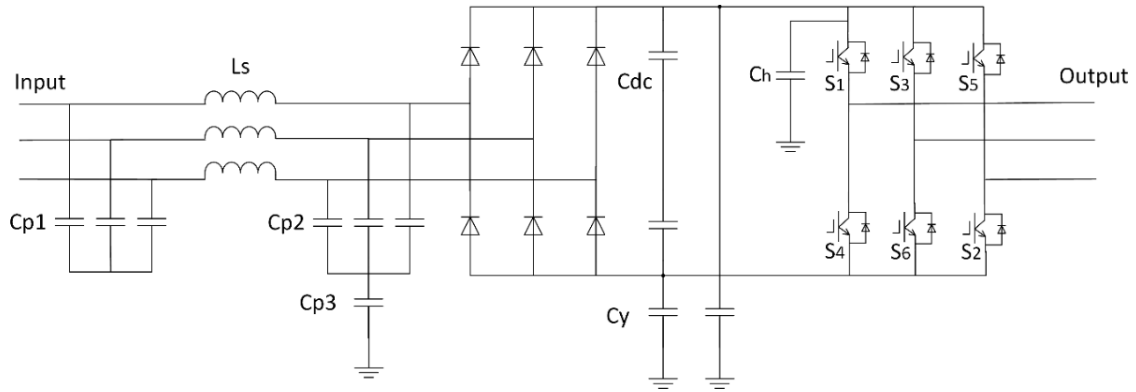
Fig. 3-14 Equivalent circuit for the Vacon inverter

Table 3-6 Parameters of the Vacon inverter

Parameters	C_{p1}	L_s	C_{p2}	C_{p3}	C_{dc}	C_y
Value	1 uF	600 uH	300 nF	300 nF	1.0 mF	2.5 nF

As mentioned in the previous section, bearing impedance can change from its insulating to conducting states at random. This random behavior of the bearings in Fig.3-7 is modeled via a "switch" whose model is shown in Fig. 3-15.
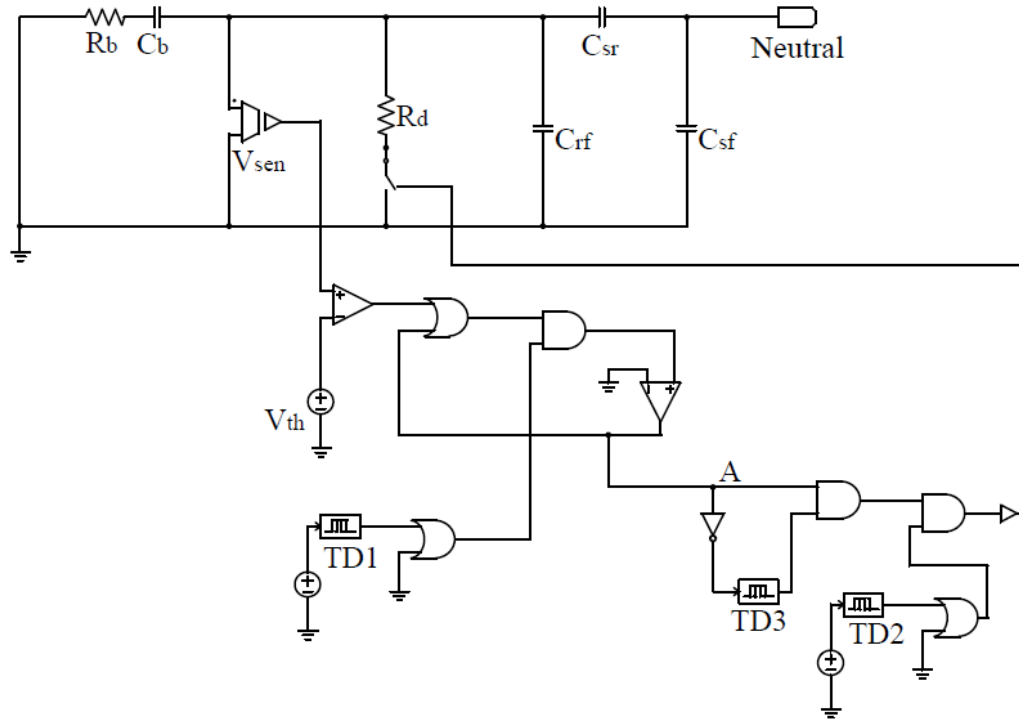
Fig. 3-15 Switch model for emulating the passage of EDM currents through the bearings

A voltage sensor(V_{sen}) is connected across the bearing capacitance(C_b) and bearing resistance(R_b), as shown in the figure. V_{sen} monitors the bearing voltage and provides a trigger voltage signal to the controlled switch. When a trigger voltage signal exceeds a pre-defined threshold value(V_{th}), the signal at point A will change from low to high, indicating the beginning of one single electric discharge. The transition of the bearing impedance from insulating to conducting state occurs when the switch closes because of the applied pulse, whose amplitude and width are configurable. The closure of the controlled switch is accompanied by a harmful EDM current which flows through the compromised bearing. Time delay TD1 and TD2 help to avoid the malfunction of the controlled switch at the unstable stage of the system, thus the discharge during normal operation is captured. Pulse width is controlled by TD3 and is set to 10 us in the

simulation. R_d represents the equivalent discharge resistance and determines the amplitude of discharge current.

3.2.4 Simulation results for the three-phase induction motor

Figs. 3-16 and 3-17 show the phase-to-phase voltage, the CM voltage, the phase current, the CM current and the bearing voltage based on different time scales. Fig. 3-16 is based on the output-frequency time scale while Fig. 3-17 based on the carrier-frequency time scale. These two figures show simulation waveforms when the bearing is intact, that is, the controlled switch in Fig. 3-15 is always open.
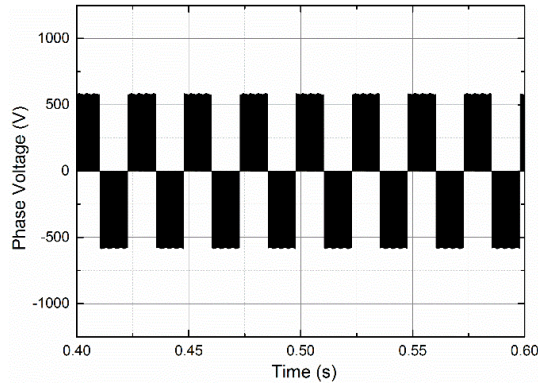
(a)
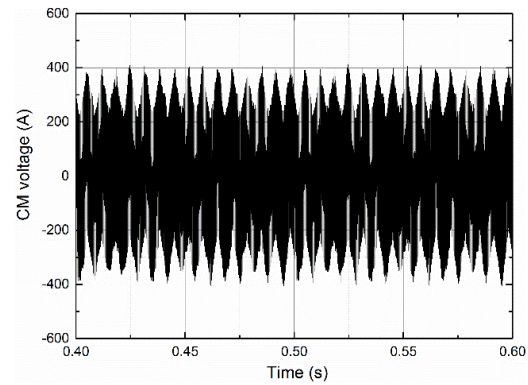
(b)
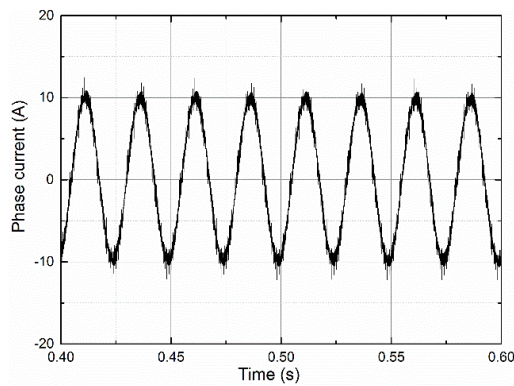
(c)
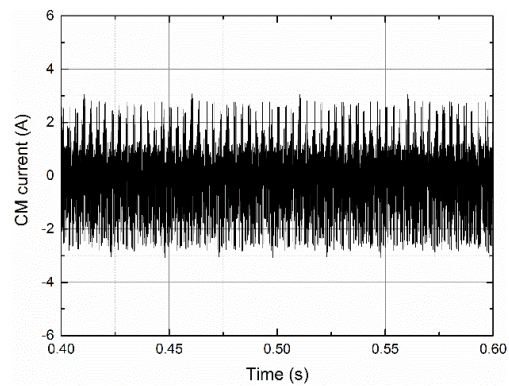
(d)
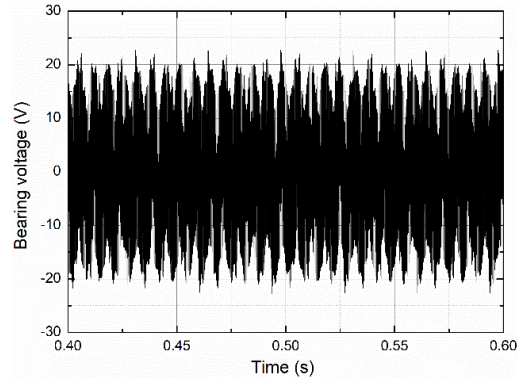
(e)

Fig. 3-16 Simulation waveforms based on the output-frequency time scale when the bearing is intact. (a)Phase voltage (b)CM voltage (c)Phase current (d)CM current (e)Bearing voltage
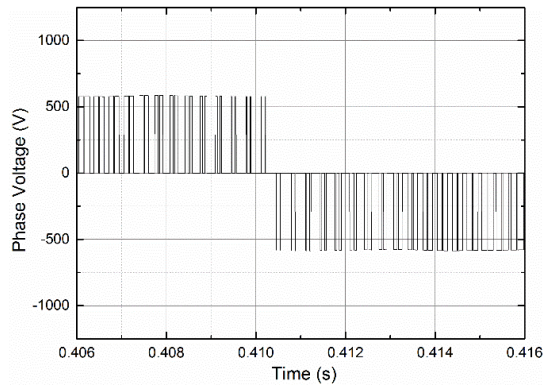
(a)
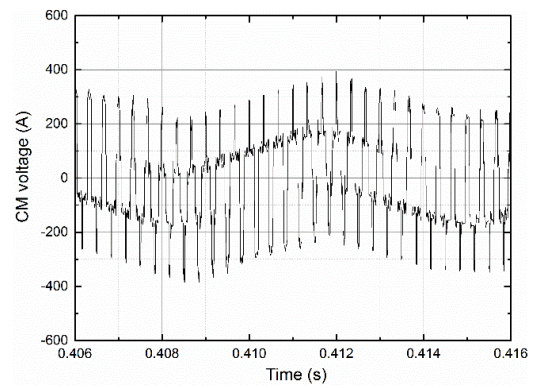
(b)
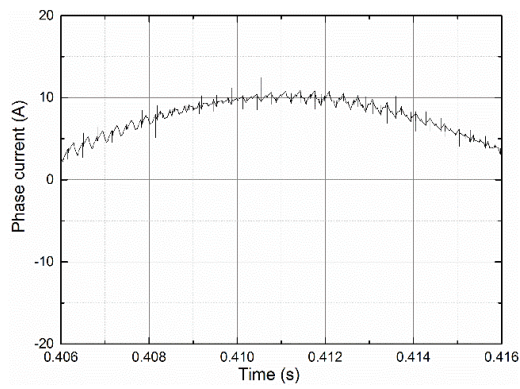
(c)
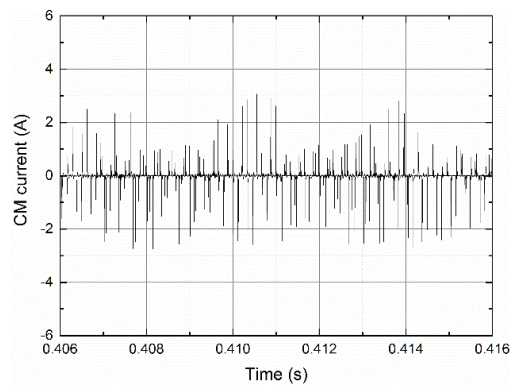
(d)
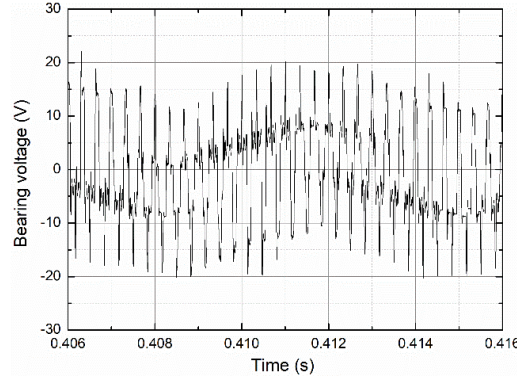
(e)

Fig. 3-17 Simulation waveforms based on the carrier-frequency time scale when the bearing is intact. (a)Phase voltage (b)CM voltage (c)Phase current (d)CM current (e)Bearing voltage

The voltage-source PWM inverter with a carrier frequency of 3 kHz was operating at an output frequency of 40 Hz under the so-called "voltage-per-hertz control". The 400-V 5.5-kW six-pole induction motor was unloaded and operated at 800 rpm. As shown in Fig 3-16 and Fig. 3-17, the CM voltage from a two-level PWM voltage source inverter is a high-frequency step waveform with 150 Hz oscillation which comes from the ripple of dc-link voltage.

A close-up waveform of the CM voltage, CM current and bearing voltage is shown in Fig. 3-18. The top plot shows the variation of the CM voltage whose high *dv/dt* causes a current spike each time when an IGBT switches. When the bearing impedance is insulating(capacitive), the ratio of the bearing voltage to the CM voltage can be expressed in terms of the values of C_{wr}, C_{rf} and C_b. The magnitude of the resulted bearing current ratio in Fig. 3-18 is consistent with that given in [58], which states that the ratio typically ranges from 2% to 10% for standard squirrel-cage induction motors with power ratings $\leq$500 kW.
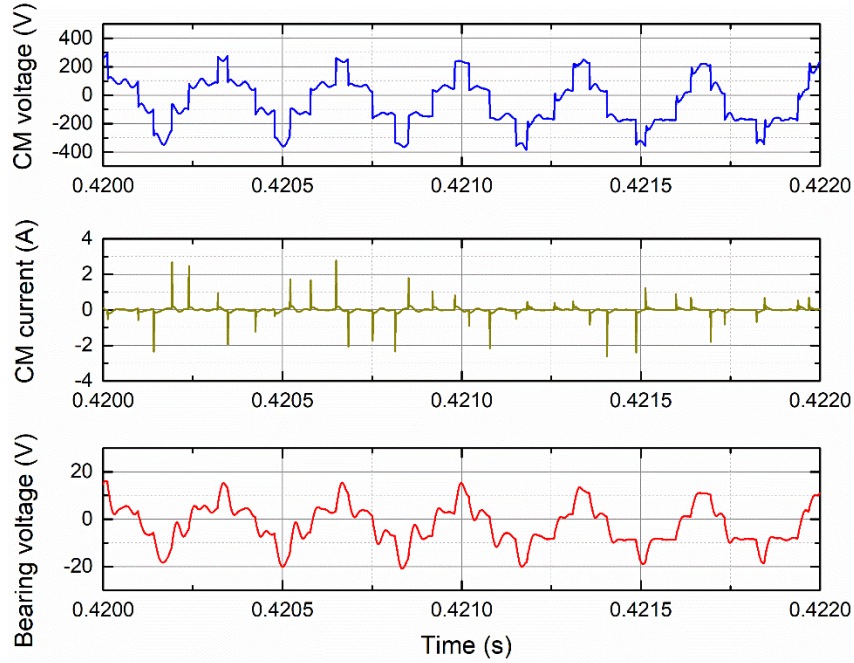
Fig. 3-18 Close-up waveforms of the CM current, CM voltage and bearing voltage

As can be seen in Fig. 3-19(a), the two bearing voltage curves are identical until the controlled switch closes (bearing impedance becomes conducting), at which point the voltage across C_b is shorted for approximately 10 μs (determined from the time delay TD3 in Fig. 3-12). After the bearing impedance becomes capacitive again (e.g., when the lubricating film is reestablished in the space between the bearing balls and races) and the controlled switch reopens, bearing voltage starts to follow the CM voltage over the capacitive voltage divider in Fig. 3-18. The bearing voltage drops suddenly to zero at the time of discharge. After the discharge transient, the bearing impedance restores back to capacitive again and then the bearing voltage follows the CM voltage waveform through the capacitive voltage divider. The bearing voltage can be charged up to twice the normal level by the bearing current [22], which is not due to the reflection of long cable. The closing of the controlled switch is accompanied by the passage of EDM bearing current, shown in Fig. 3-15(b), whose magnitude is determined by the resistor in series with the

controlled switch. At intact lubrication film, the normal capacitive bearing current is usually much smaller than the EDM bearing current, thus a sudden bearing voltage dropping together with a pronounced bearing current spike can cause an arcing in the bearing. Such repeated arcing through a compromised bearing can lead to premature bearing failures.
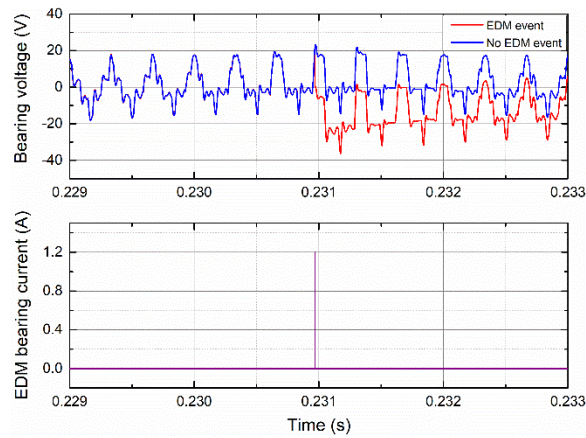
(a)
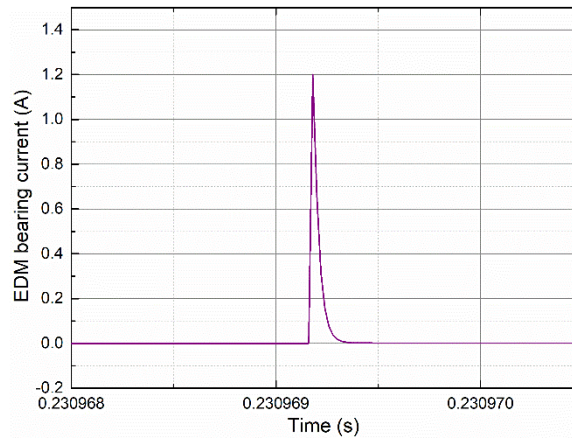
(b)

Fig. 3-19 (a) Bearing voltage (top) and EDM bearing current (bottom) for the 5.5-hp motor when the controlled switch is momentarily closed (red curve, EDM event). (b) Close-up waveforms of the discharge bearing current

The proposed model is also employed to perform a parameter analysis of the EDM process. Due to the pollution effect of the grease caused by metallic particles, an aged

motor bearing usually have increased bearing capacitance [59]. In Fig. 3-20, as bearing capacitance varies from 100 pF to 5 nF, the peak value of bearing voltage decreases from around 24 V to 8 V. Therefore, it's harder to puncture an aged bearing or in other words, the waiting time to puncture an aged bearing is longer.
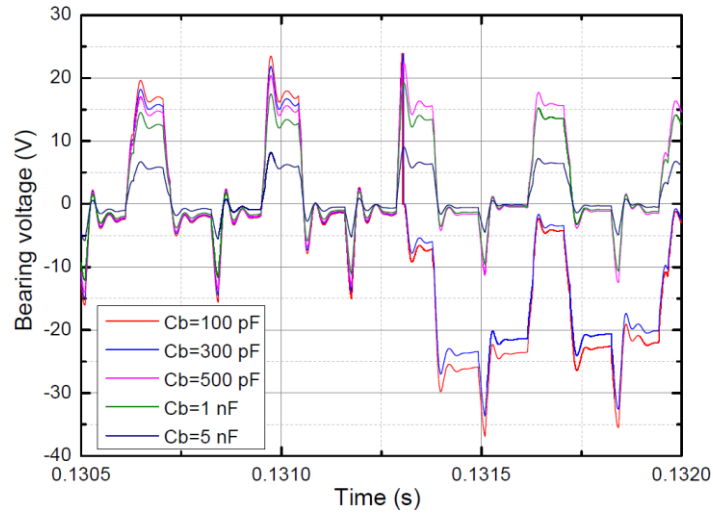
Fig. 3-20 Bearing voltages with different bearing capacitances

3.3 Experimental analysis of bearing degradation

In this section, an IGBT-based VFD system with a 5.5 kW induction motor is set up to understand the cause of bearing degradation and effectiveness of mitigation techniques. By analyzing the experimental results of the VFD system, it allows an in-depth understanding of the cause and effect chain of the bearing degradation. The effectiveness of shaft grounding brush and CM filter are also evaluated for the reduction of CM current.

3.3.1 Experimental setup

Fig. 3-21 shows the experimental setup connecting a voltage source PWM inverter and a 5.5 kW induction motor via a 5m unshielded cable. In the PWM controller, three-phase

balanced reference signals are compared with a repetitive 3 kHz triangular carrier signal to generate the sinusoidal PWM (SPWM) gate signals for the IGBTs. The presence of LISN is necessary because it prevents externally conducted emission on the mains from contaminating the measurement and provides stable and clean power to the inverter. All the subsystems including the induction motor are placed on a large metal sheet according to the conducted emission testing requirement of CISPR 25 [60]. All the measurements are performed under no load condition, which represents the worst-case scenarios of CM current [61]. As shown in Fig. 3-22, a tip made of carbon fiber is attached to the shaft to obtain the shaft voltage and a grounding brush of the same material can be used to provide a low impedance path between the rotating shaft and the motor frame. Motor bearings are modified to provide direct access to the bearing current as shown in Fig. 3-22. Both the drive and non-drive ends bearings are covered with an insulating support layer and the bearing outer surface and frame are connected via a short wire which facilitates the measurement of bearing current.
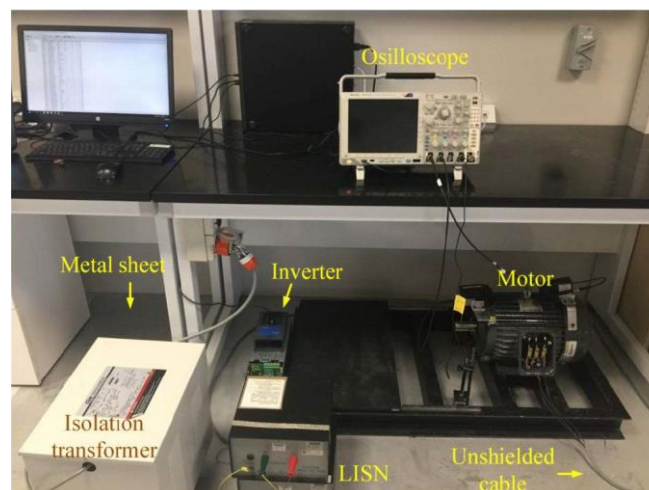
Fig. 3-21 Experimental setup of a PWM inverter and a 5.5 kW induction motor
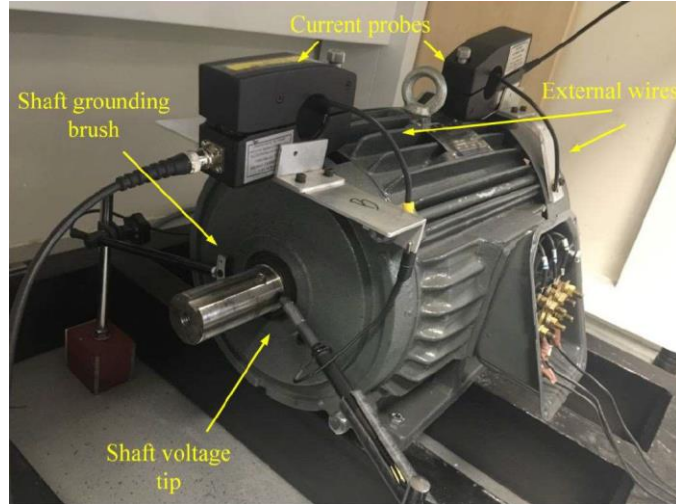
Fig. 3-22 Test instrument for the shaft voltage and bearing current measurements

In the experiment, an oscilloscope (Tektronix MD04104C, 1 GHz bandwidth, 3 GS/s sampling rate) is chosen for the measurement. Three differential probes (THDP0200, 200 MHz bandwidth) and a passive probe (Tektronix P2220) with AEGIS probe tip (SVP-TIP-9100) are selected to measure the inverter terminal voltages and shaft voltage, respectively. The CM current and the bearing current are measured with the same RF current probe (Solar Electronic 9134-1, 100 MHz bandwidth).

3.3.2 Causes of bearing degradation

Fig. 3-23 shows the measurement results when the motor rotating speed is 800 rpm and different time scales are chosen to illustrate the operating behavior of the motor drive system. Fig 3-23(a) is based on the inverter output frequency while Fig. 3-23(b) is based on the carrier frequency. The DC voltage after diode bridge rectifier is around 580 V. The voltage-source PWM inverter with a switching frequency of 3 kHz is operating at an output frequency of 40 Hz under V/f control. The line frequency voltage and current shown in Fig. 3-23(a) will not interact with the parasitic capacitances inside the motor.

However, the high-frequency CM voltage with high *dv/dt* capacitively induced a high-frequency shaft voltage according to BVR, as shown in Fig. 3-23(b).
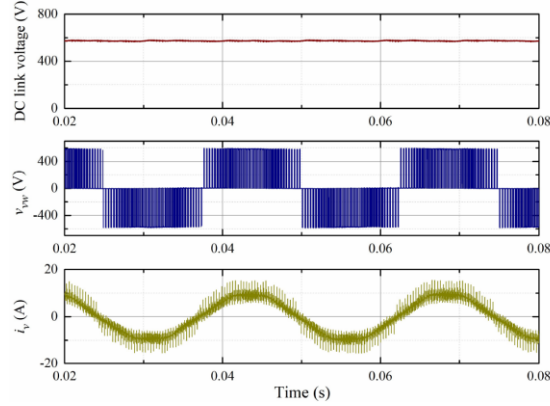
(a) Output frequency-based time scale: DC link voltage (top), line-to-line voltage v_{vw} (middle), phase current i_v (bottom)
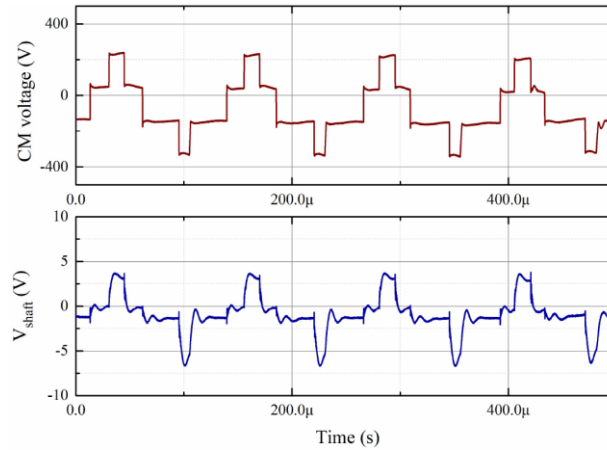
(b) Switching frequency-based time scale: CM voltage (top), shaft voltage v_{sh} (bottom)

Fig. 3-23 Measurement on a 5.5 kW, 6-pole induction motor at 800 rpm, switching frequency $f_{sw}= 3$ kHz

As the bearing impedance is a nonlinear function of the lubricating film parameters, the electric discharge occurs in a random manner. Fig. 3-24 captures one instant when the EDM process occurs. A breakdown in the lubricating film is observed and it causes the discharge of the bearing capacitor and results in a sharp pulse current. The pulse current in an unmodified motor could be more pronounced than the value shown since

the external wire and its bonding add to the loop impedance. After the bearing impedance restores back to capacitive, the bearing voltage starts to follow the CM voltage over BVR, thus the bearing voltage charges up to almost twice the normal level.

It is observed in Fig. 3-25 that the circulating bearing currents at both drive and non-drive ends, i_{b-DE} and i_{b-NDE} have a current ripple with a peak-to-peak amplitude of 15 mA and a frequency around 3 MHz, which matches well with the CM current. Therefore, the high frequency circulating bearing current can be considered as a result of the transformer effect, where the secondary side bearing current mirrors the primary induced CM current.
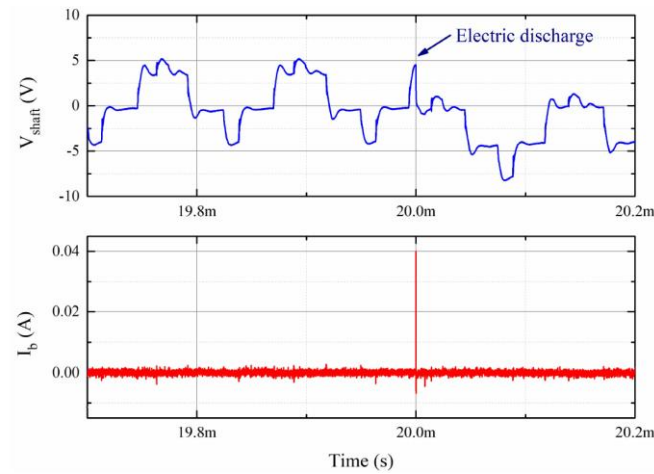
Fig. 3-24 The EDM current (top) and bearing current (bottom) for the 5.5 kW induction motor
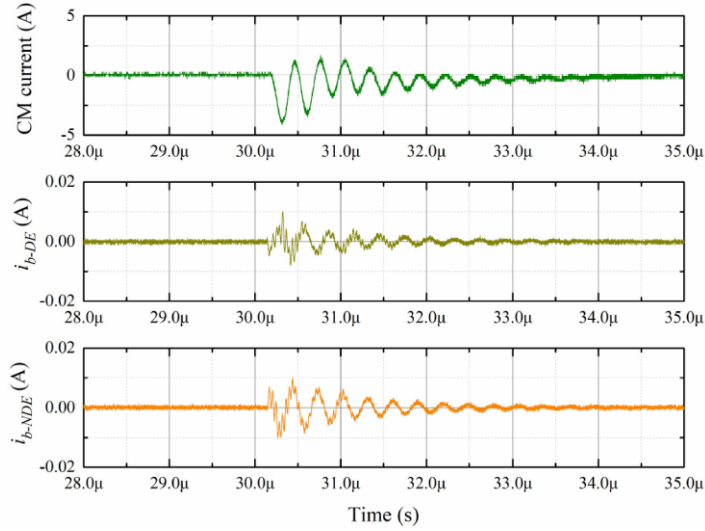
Fig. 3-25 CM current and circulating bearing current at both ends of the bearings

The cause and effect chain of bearing degradation is summarized in Fig. 3-26, where PWM CM source generates high-frequency CM voltage and CM current, causing bearing degradation via both capacitive and inductive couplings. Shaft grounding brush bypasses the bearing voltage to reduce EDM current while the CM filter attenuates the CM current to suppress the circulating bearing current. The effectiveness of these remedies will be evaluated as follows.
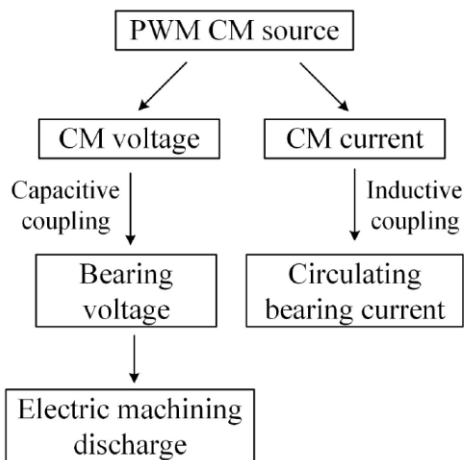
Fig. 3-26 Cause and effect chain of the bearing damage

3.3.3   Bearing grounding brush

Fig. 3-27 shows the motor shaft voltage waveforms for both ungrounded and grounded conditions. The grounding of the motor rotating shaft is achieved by a carbon fiber brush as shown in Fig. 3-22.

The grounding brush provides a low impedance path in parallel with the bearing lubrication film. Thus, the peak-to-peak shaft voltage drops from more than 8 V to less than 2 V at the instant when the brush touches the rotating shaft. Therefore, the EDM process can be prevented. However, there is no obvious reduction of the CM current and bearing current, as the CM impedance of the motor is dominated by the stator winding-to-frame capacitance, not the bearing capacitance.

The grounding brush helps to prevent bearing degradation caused by the EDM bearing current but has no impact on the CM current, which can be as high as tens of amperes in high-power motors. It is reported that in a 500-kW motor, the bearing current induced by the CM current can reach as high as 5 A peak-to-peak, which is good enough to destroy the insulating property of the lubricating film [35]. In order to reduce the CM current and the induced bearing current effectively, CM filter will be a more feasible solution.
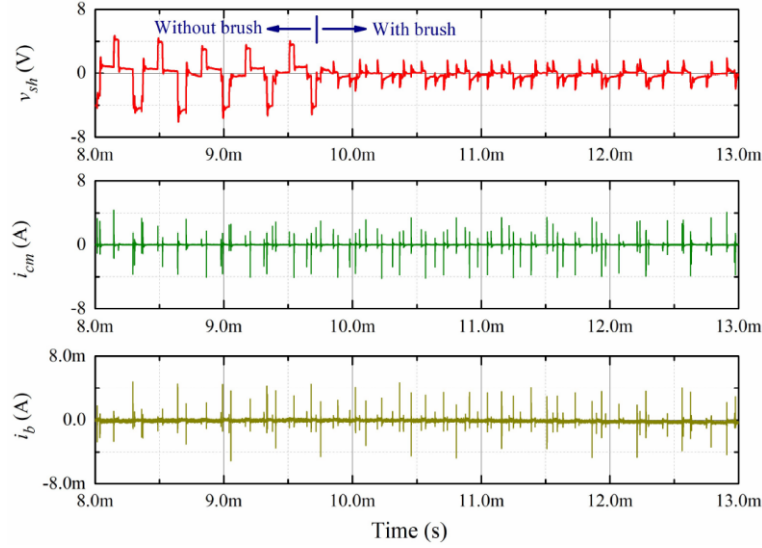
Fig. 3-27 Comparison of the shaft voltages of the ungrounded condition and grounded condition: shaft voltage v_{sh} (top), CM current i_{cm} (middle), bearing current i_b (bottom)

3.3.4 CM filter

High-power motor drive system usually requires thick multicore power cables to handle large current ratings. It's difficult to bend the rigid cables and therefore winding just a few turns or simply one turn on a magnetic core is usually adopted to provide the CM inductance. CM chokes with nanocrystalline core are selected in the test because of their high permeability, high saturation flux density and low core loss. For the experiment, four one-turn CM chokes are added between the inverter and the induction motor to suppress the CM current. The size of the chokes and the CM impedance of the four chokes together are shown in Fig. 3-28.
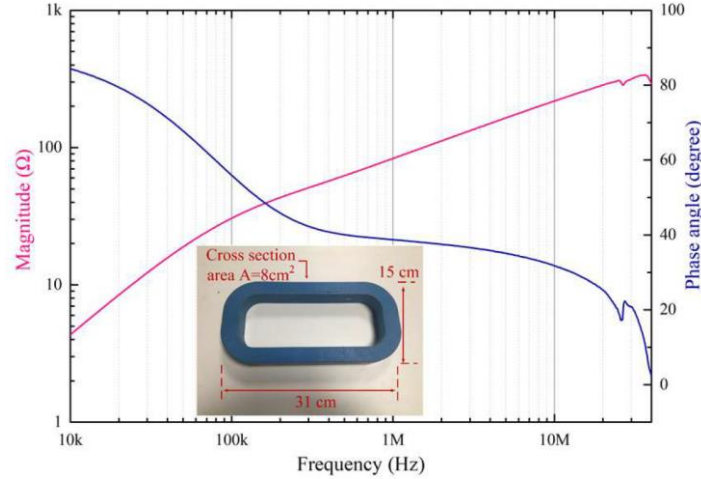
Fig. 3-28 CM impedance of the four one-turn CM chokes together

Fig. 3-29 shows the measured the CM currents with and without the CM chokes in time-domain. It is clearly observed the current spikes have reduced significantly due to higher CM impedance in the current propagation path. Fig. 3-30 shows the CM currents in frequency-domain and the CM chokes begin to show their effect above 500 kHz. The attenuation offered by the CM chokes is clearly observed by comparing the spectrum envelops of the CM currents with and without the CM chokes. For better visibility, the attenuation contributed by the CM chokes is plotted as a red curve in Fig 3-31. Most filters available in the market are designed and tested based on 50 Ω source and load terminations. Based on this assumption, the attenuation of the CM chokes can be estimated as follows:

$$Att = \frac{100 + Z_{CMC}}{100} \qquad (3\text{-}7)$$

where Z_{cmc} is the total CM impedance of the four chokes in Ω.
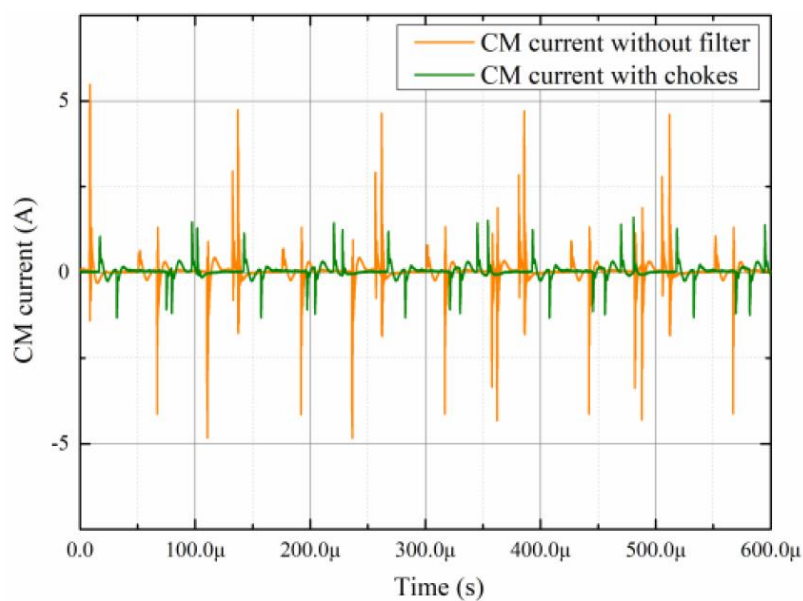
Fig. 3-29 Time domain waveforms of CM currents with and without chokes.
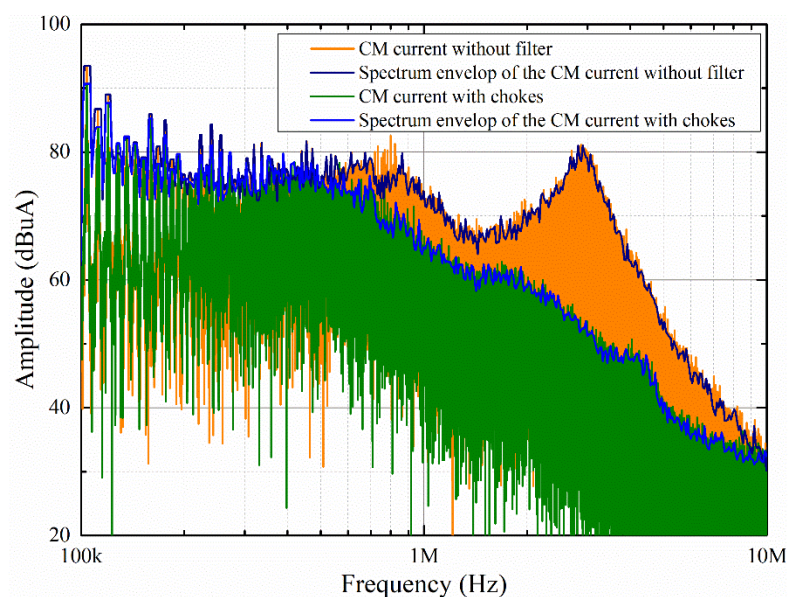
Fig. 3-30 Frequency spectrum of CM currents with and without chokes.

The estimated attenuation is also plotted as a blue curve in Fig. 3-31. A large discrepancy between the estimated and measured attenuations is observed. The reason is that in the motor drive system, the CM filter will rarely be terminated with 50 Ω source and 50 Ω load. Therefore, the actual filter attenuation is very much dependent on the

actual source and load impedances in a specific application. Detailed information of the source and load impedance will be indispensable in evaluating the filter performance.
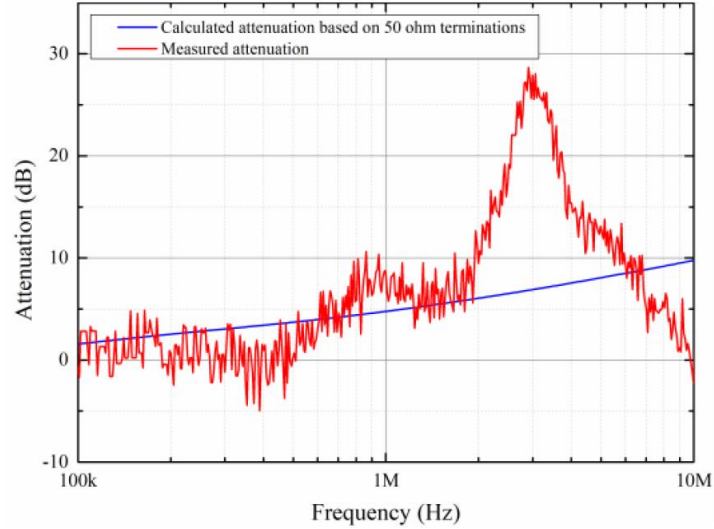
Fig. 3-31 Estimated attenuation based on 50 Ω terminations and measured attenuation.

3.4   Summary

This section discusses the high-frequency simulations of single- and three-phase induction motor circuits under PWM operation. High-frequency simulations are important in providing valuable insight into the motor's CM behavior which is especially useful in identifying remediation techniques for the reduction of CM noise. The model of the three-phase motor drive system with an improved controlled switch is introduced to study the bearing discharge process. Proposed model is integrated into the motor circuit and it takes care of the unstable state at the beginning of the simulation. EDM process is observed in the simulation and a parameter analysis is performed to understand the influence of bearing capacitance on the bearing discharge.

The cause and mechanism of the bearing current is also investigated. Mitigation techniques using grounding brush and adding CM filter are both experimentally studied and evaluated. It is found that the grounding brush can only help to prevent bearing degradation caused by the EDM bearing current but has no impact on the CM current. CM filter is preferred for high-power motors where the circulating bearing current is dominant.

Chapter 4 In-Circuit Impedance Measurement

4.1   Introduction

The CM filter is usually preferred over a *dv/dt* filter or a sine filter to suppress the CM current, as it can provide high CM impedance that reduces the resulted circulating bearing current in high power motor drive systems. CM filter designs have been well documented in [62, 63] and usually, the filters available in the market provide their attenuation specifications under the well-defined 50 Ω terminations [21, 50]. In reality, the noise source and load termination impedances in an inverter-drive system are far from 50 Ω and thus, off-the-shelf CM filters in the market are not always optimal for a specific operating condition. Results in the previous section have shown that the estimated attenuation based on the 50 Ω terminations and measured attenuation in the real system could be very different. Another option is to design the filter by considering the source and load impedance to be 0.1Ω/100Ω or 100Ω/0.1Ω [21], but the results still remains different from the real case.

To design a CM filter with desired performance, prior information of both the CM noise source and load termination impedances have to be known. The CM impedance of the motor (load) can be measured offline as the motor speed has little impact on the motor's CM impedance. Online extraction of the motor's CM impedance is also possible based on the spectrums of CM voltage and CM current. To obtain the CM impedance of the inverter (noise source), one could either estimate it from offline measurement or

simply assume some typical values, but such estimates can deviate significantly from the noise source impedance under the actual operating conditions. An indirect way to estimate the online source impedance was proposed in [29] by inserting a known-impedance component after the source and comparing the insertion loss. However, it is difficult to find the exact same time offset in time domain measurements, thus, the phase information of insertion loss may not be accurate enough [30]. As introduced in the literature review, the in-circuit impedance extraction based on an inductive coupling approach has been reported as a feasible method by injecting a high-frequency excitation to the CM loop and monitoring it simultaneously. However, for high-power motor drive systems with much higher background CM noise, the signal-to-noise ratio to yield good measurement results is an issue. This section improves on the existing in-circuit measurement approach in two aspects: firstly, enhances SNR under high background noise and secondly, provides protection to the test instrument in the measurement setup. The improvements allow the method to be extended to a high-power inverter-driven motor system for systematic CM filter design.

4.2 Proposed Improvement on In-circuit Impedance Measurement

4.2.1 SNR enhancement and surge protection

To improve the SNR of the in-circuit impedance measurement based on inductive coupling approach for high-power motor drive systems, an amplifier is added at the signal source output of a vector network analyzer (VNA) and an external directional

coupler is used to protect the two input ports of the VNA from possible damage due to switching transients of the inverter. The reflection and transmission coefficients are measured based on the test setups shown in Figs. 4-1 and 4-2, respectively.
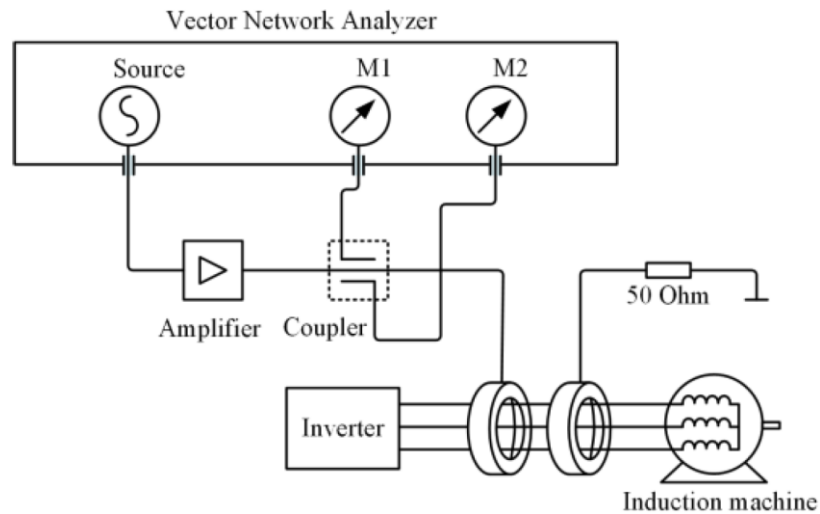
Fig. 4-1 Measurement of the reflection coefficient.
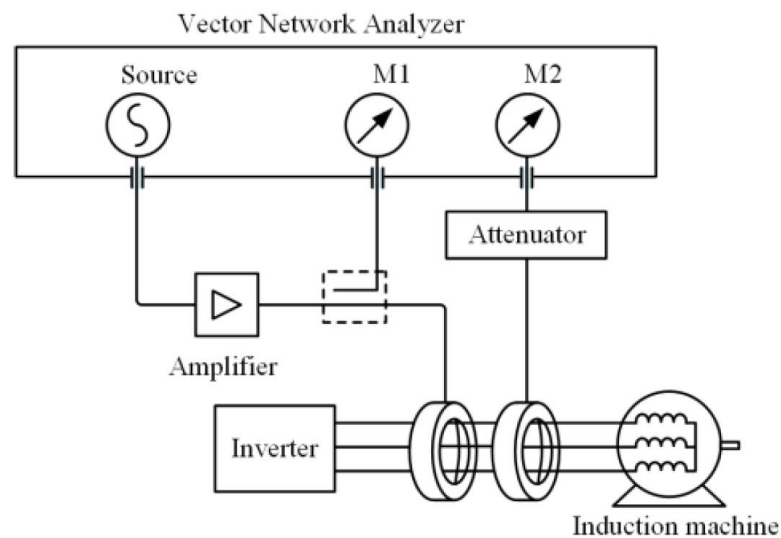
Fig. 4-2 Measurement of the transmission coefficient.

A VNA (Bode100 Omicron-Lab, 10 Hz to 40 MHz) measures the S-parameters. Its signal output feeds an injecting inductive coupling probe (Solar 9144-1N, 10 kHz to 100 MHz) through an amplifier (AR 100A250A, 10k Hz to 250 MHz, 100 W). Another inductive coupling probe (same model) tracks the same injecting signal and is measured

by another port of the VNA. As shown in Fig. 4-1, the reflection measurement is performed with the RF amplifier in combination with an external bidirectional coupler. The amplifier boosts the VNA output signal and protects the output from possible reverse power due to the motor drive system. M1 and M2 measure the coupled backward and forward signals through the directional coupler [64]. In the measurement, a directional coupler with 40 dB coupling coefficient is chosen and the loss of the coupler can be compensated through short, open and load (SOL) calibration. By using the external coupler, it is possible to boost the VNA source signal without damaging the measuring ports. The receiving probe is terminated with 50 Ω, which allows the extraction of S-parameter, S_{11}. By swapping the injecting probe and the receiving probe, S_{22} can also be obtained similarly.

For the transmission coefficient measurement in Fig. 4-2, an amplified RF signal is injected into the motor drive system and then measured by M2 through an external attenuator. The injected signal will be much higher than the existing CM background noise in the motor drive system for good SNR on the received signal at M2. M1 is coupled to the amplified output source of the VNA to measure the output signal. It is necessary to perform through calibration to de-embed the gain and phase introduced by the connection cable, the RF amplifier and the external attenuator. Therefore, the measured S_{21} becomes the transmission coefficient from the input of the injecting probe to the output of the receiving probe. Similarly, S_{12} can be measured by swapping the injecting and the receiving probes. Ideally, swapping the probes makes no difference since both probes are identical. However, the individual difference of the same model of probe exists and may cause a slight difference of the measurement results, which will be

explained in the next section. Thus, two sets of measurements are conducted to minimize error due to such differences.

After calibration, the measured S-parameters describe a lumped two-port network consisting of the motor drive system and the two probes, as illustrated in Fig. 4-3(a). The CM equivalent circuit model of the motor drive system consists of the inverter (noise source) impedance Z_s, induction motor (load) impedance Z_{load} and the three-phase cable bundle impedance Z_{wire}. The injecting and receiving probes can be modeled as two transformers with the ratios of N:1 and 1:N, respectively. Therefore, the two-port network between ports 1 and 2 is M_{total}, which is a cascaded network of M_{inj}, M_{system} and M_{rec}, as illustrated in Fig. 4-3(b). With the measured S-parameters, we can convert them to two-port ABCD parameters and M_{total} can be expressed as:

$$\begin{bmatrix} A & B \\ C & D \end{bmatrix}_{total} = \begin{bmatrix} A & B \\ C & D \end{bmatrix}_{inj} \begin{bmatrix} A & B \\ C & D \end{bmatrix}_{system} \begin{bmatrix} A & B \\ C & D \end{bmatrix}_{rec} \tag{4-1}$$

where $\begin{bmatrix} A & B \\ C & D \end{bmatrix}_{inj}$, $\begin{bmatrix} A & B \\ C & D \end{bmatrix}_{system}$ and $\begin{bmatrix} A & B \\ C & D \end{bmatrix}_{rec}$ represent the *ABCD* parameters of M_{inj}, M_{system} and M_{rec}, respectively.

(a)

(b)
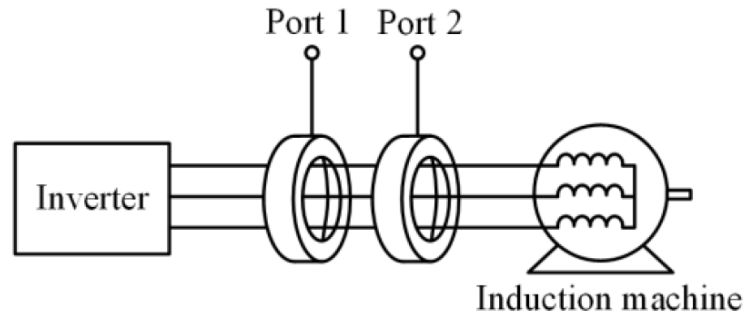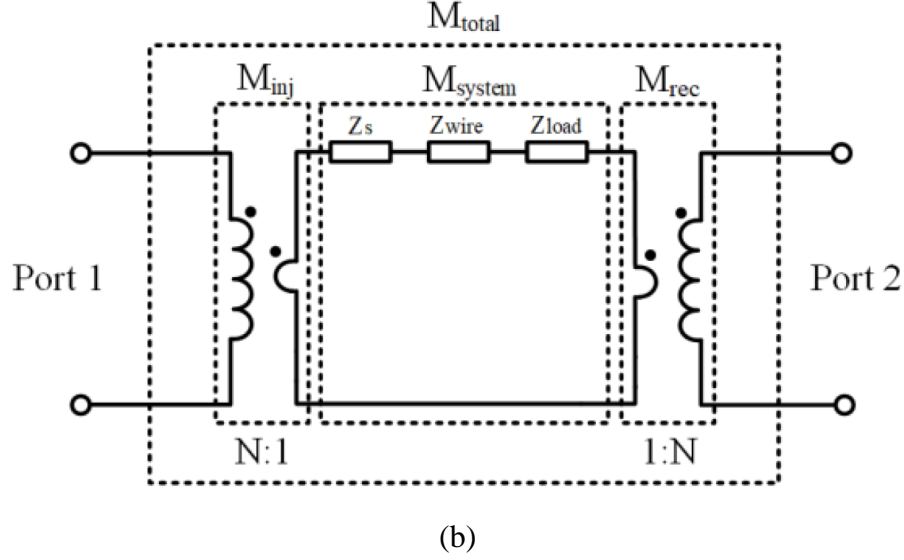
Fig. 4-3 (a)Two-port network consisting of current probes and motor drive system. (b) Equivalent circuit model.

$\begin{bmatrix} A & B \\ C & D \end{bmatrix}_{inj}$ and $\begin{bmatrix} A & B \\ C & D \end{bmatrix}_{rec}$ can be determined through pre-calibration of the probes.

Based on the matrix inversion of (4-1), $\begin{bmatrix} A & B \\ C & D \end{bmatrix}_{system}$ can be determined, where

parameter B is the system impedance. By subtracting the load and the cable impedances from the system impedance, one can extract the source impedance under its actual operating condition as follows:

$$Z_s = B_{system} - Z_{load} - Z_{wire} \tag{4-2}$$

Flow chart of the proposed online impedance extraction method is shown in Fig. 4-4. Reflection (S_{11}, S_{22}) and transmission coefficients (S_{12}, S_{21}) here are measured separately with different device configurations. After obtaining the S parameters, loop impedance Z_{system} is calculated with the same equation in (4-2).
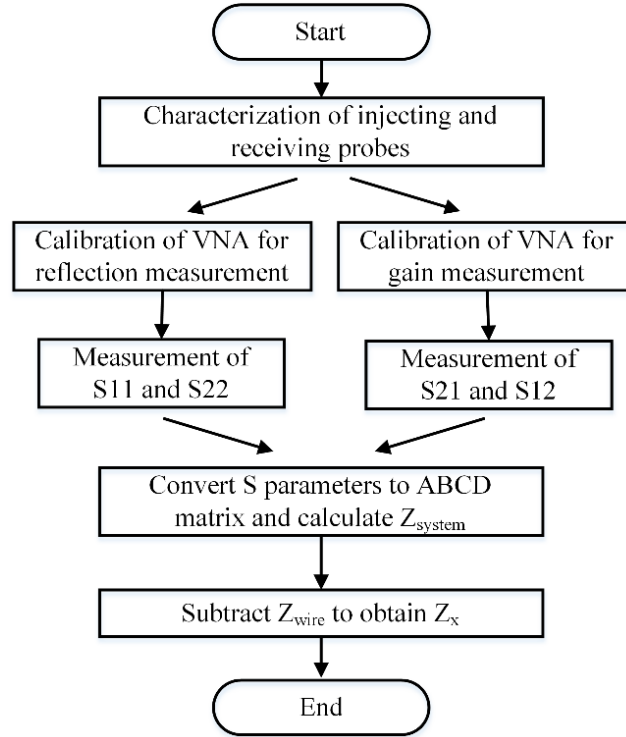
Fig. 4-4 Flow chart for the proposed approach with an amplifier

4.2.2 Characterization of Inductive Coupling Probes

As mentioned before, the probe with the cable being clamped can be represented by a transformer, which has to be characterized beforehand. A calibration fixture (Solar 9125-1) is used to measure the S-parameters of the injecting and receiving probes so that $\begin{bmatrix} A & B \\ C & D \end{bmatrix}_{inj}$ and $\begin{bmatrix} A & B \\ C & D \end{bmatrix}_{rec}$ can be obtained, respectively. Figs. 4-5 and 4-6 show the measurement setup to characterize the probe. The injecting or receiving probe is clamped onto the inner conductor of the test fixture. One end of the test fixture is terminated by a BNC short, which connects the frame and inner connector to form one side of the two-port network and the probe under test gives another side. At high frequency, both inductive and capacitive couplings exist between the current probe and clamped conductor, thus characterization of the current probe is necessary.
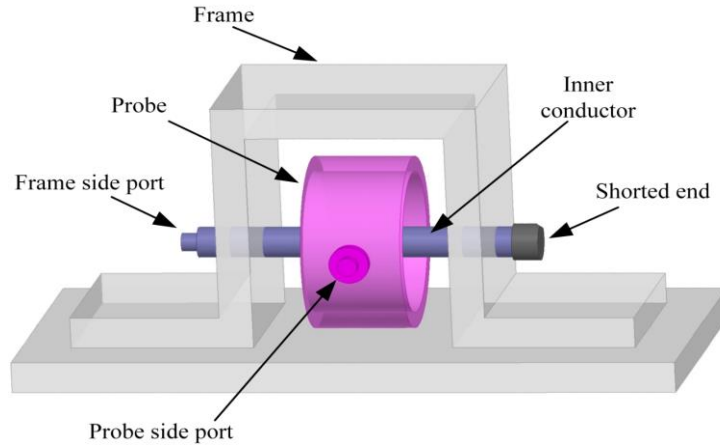
Fig. 4-5 Test fixture to characterize the injecting and receiving probes
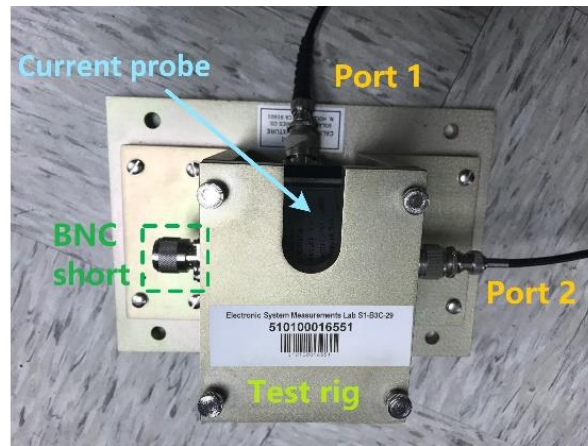
Fig. 4-6 Setup for the S-parameters measurement of the probe.

For the receiving probe, ports 1 and 2 of the VNA are connected to the frame-side port and the probe-side port, respectively. Whereas, for the injecting probe, ports 1 and 2 of the VNA are swapped. The measured amplitude of the S-parameters of the injecting and receiving probes are given in Figs. 4-7(a) and 4-7(b), respectively.

(a)   (b)
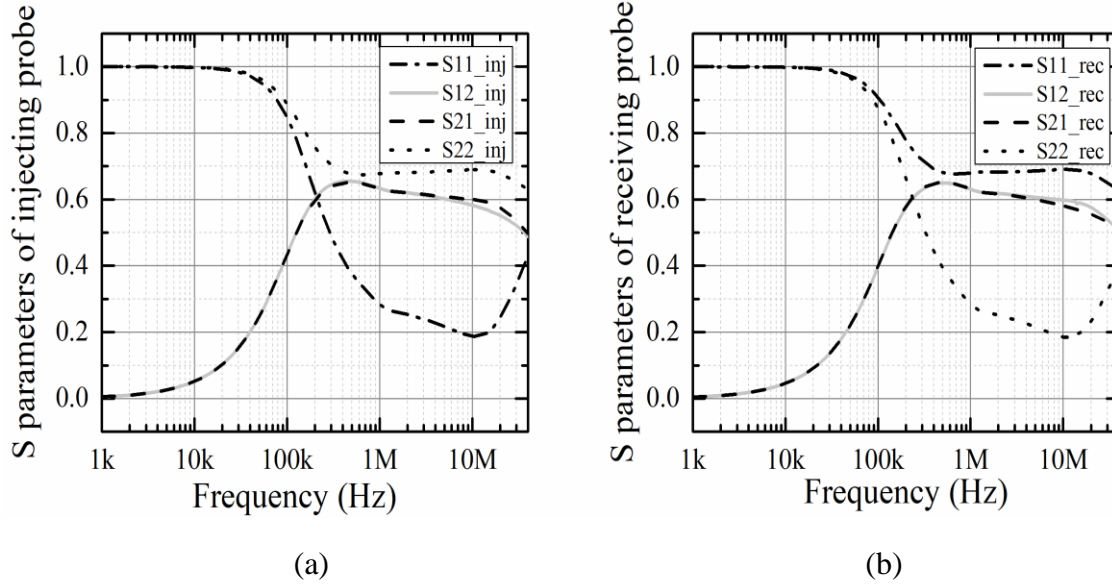
Fig. 4-7 Measured S-parameters. (a) Injecting probe. (b) Receiving probe.

4.2.3   Front-end protection and improved SNR

The background noise in a high-power motor drive system can be very high. Also, the fast switching of the IGBTs can cause front end damage to the measurement ports of VNA. Fig. 4-8 shows the time-domain signal captured directly from the output of an inductively sensing probe (Solar 9144-1N) whose peak value can be as high as 37 V and has well exceeded the input voltage limit of both ports M1 and M2, even with the internal attenuators set to their maximum values. Therefore, to use the inductively coupling method for high power inverter-driven systems, front-end protection is necessary, which can be achieved by adding the bidirectional coupler and the external attenuator for ports M1 and M2.
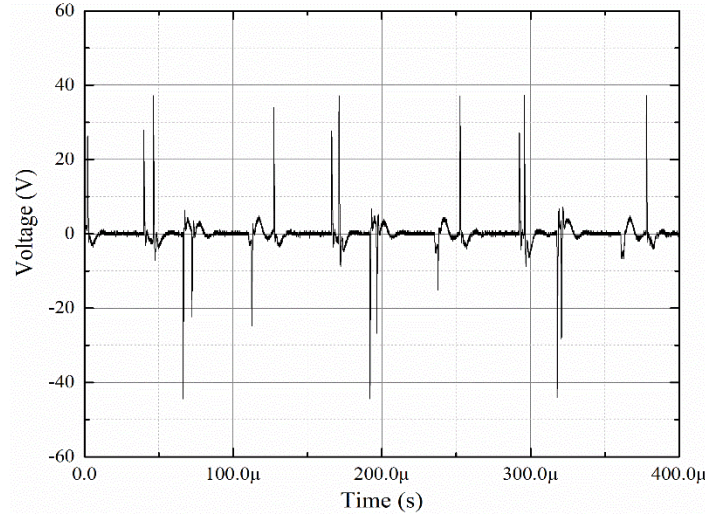
Fig. 4-8 Captured signal from current probe 9144-1N

The SNR of the existing inductively coupling approach is also examined experimentally. Considering the capacitive behavior of the CM path at low frequency, relatively high CM impedance is expected, and it attenuates the injected signal, which causes degradation of SNR. To evaluate the SNR performance, a test signal sweeping from 100 kHz to 1 MHz from the signal output of the VNA is injected into the CM path of the motor drive system. The captured signal from the receiving probe versus frequency is plotted in Fig. 4-9 and indicated as the dotted line, which is about 5 to 10 dB higher than the background CM noise in the system, plotted as the solid line. With the proposed setup, the amplified injecting signal provides a significant improvement in SNR, as observed in Fig. 4-9. The enhanced SNR ensures reliable measurement results with good confidence for high-power systems with high background noise.
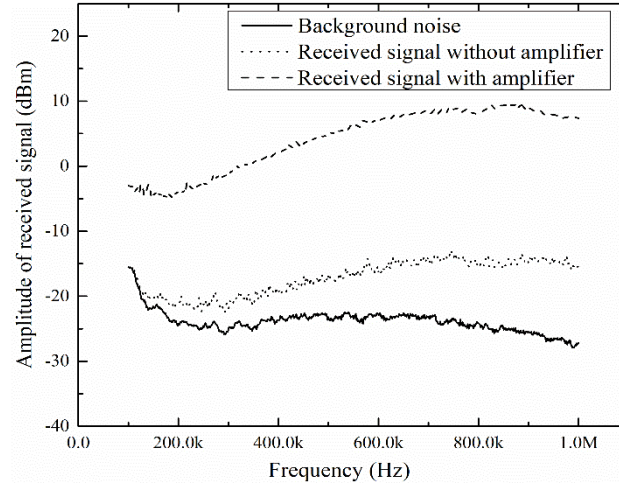
Fig. 4-9 Comparison of the background noise and received RF signal between the conventional setup and proposed setup with amplifier and front end protection.

4.2.4 Experimental Validation

To validate the proposed online measurement method, the motor drive system shown in Figs. 4-1 and 4-2 is replaced by several known passive components. The components under test include three through-hole resistors: 50 Ω, 220 Ω and 2.2 kΩ; two film capacitors: 120 pF and 2.2 nF; and two axial-lead inductors: 100 µH and 660 µH. The impedance of each passive component is extracted by subtracting the wire loop impedance from the measured impedance. Fig. 4-10 compares the measured results with the impedance analyzer and the proposed approach in the frequency range of 100 kHz-40 MHz. It has shown that for all both magnitude and phase of the measured impedance are in close agreement with each other. The self-resonant frequencies of the inductors and capacitors are expected and also match well.
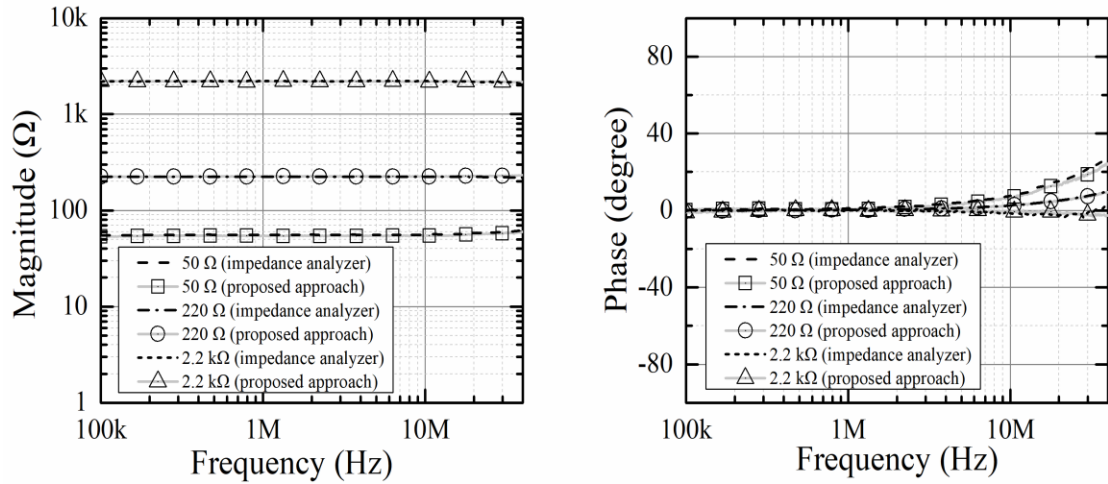
(a)
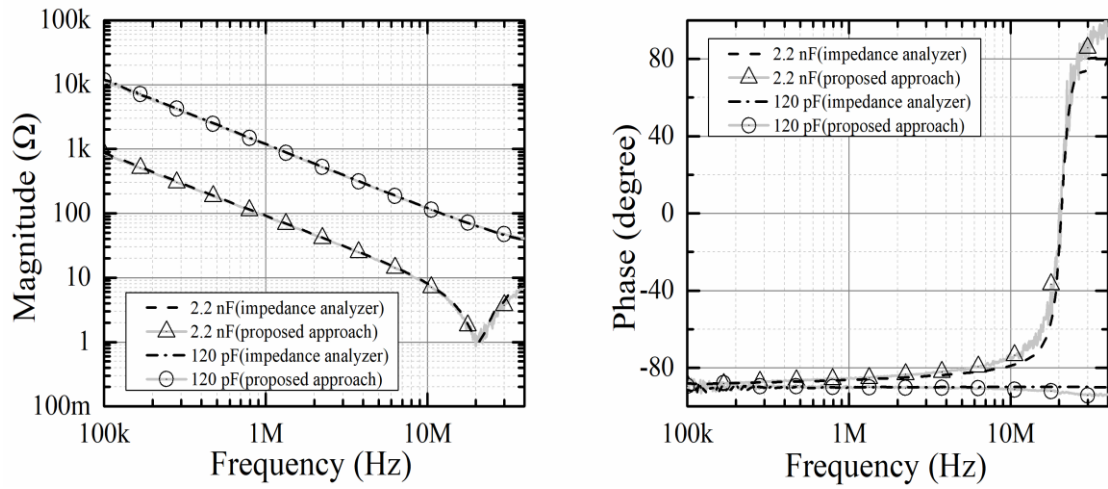
(b)
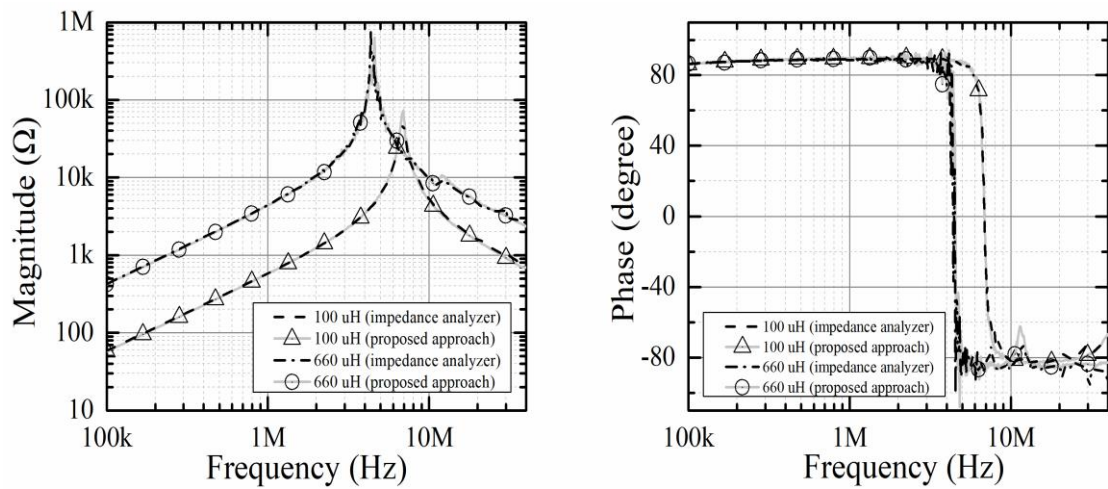
(c)

Fig. 4-10 Measured impedance of passive components (a) Resistors: 50 Ω, 220 Ω and 2.2 kΩ (b) Capacitors: 120 pF and 2.2 nF (3) Inductors: 100 μH and 660 μH.

4.3 Source impedance measurement

4.3.1 Experimental setup

Now the proposed method is used to extract the CM source impedance of a motor drive system consisting of a variable frequency drive (Vacon NXP 00225A2H1SSS), a 5.5 kW induction motor (TECO 1071033064C-1) and three-phase cable, as shown in Fig. 4-11. The VFD and induction motor are connected via a short cable of 0.4 m. Two fixed positions are marked on the cable for the injecting and receiving probes. The proposed method is able to extract the CM impedance of the total circuit, then the source impedance is calculated based on the assumption that the CM impedance of the induction motor is speed-independent.
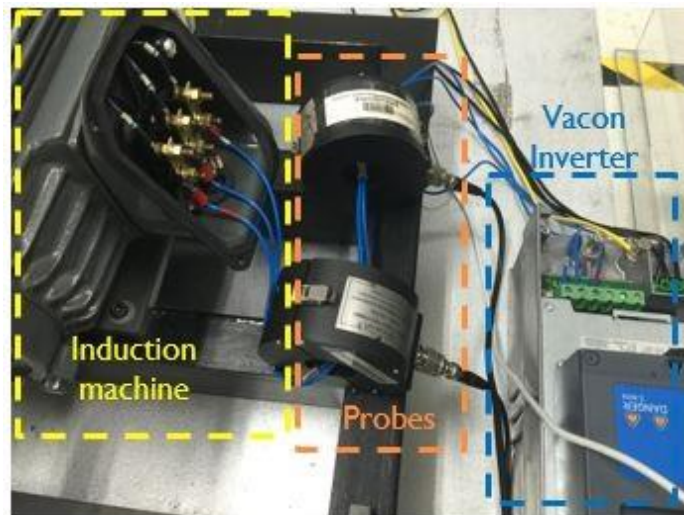
Fig. 4-11 Online measurement setup of an operating motor drive system

4.3.2 Extracted online source impedance

Fig. 4-12 shows the measured resultant CM impedance as well as the impedances of the motor and the cable. Then the noise source impedance is obtained by subtracting the CM impedances of the induction motor and the cable from the resultant system impedance, which is also shown in Fig. 4-12. CM impedance of the cable and the induction motor is obtained by the offline measurement with an impedance analyzer. CM impedance of the motor is usually stable as the operation condition does not affect the stray capacitance between the stator winding and the motor frame. Offline measurement of the motor CM impedance has been widely accepted in the study of CM current. [65-67]
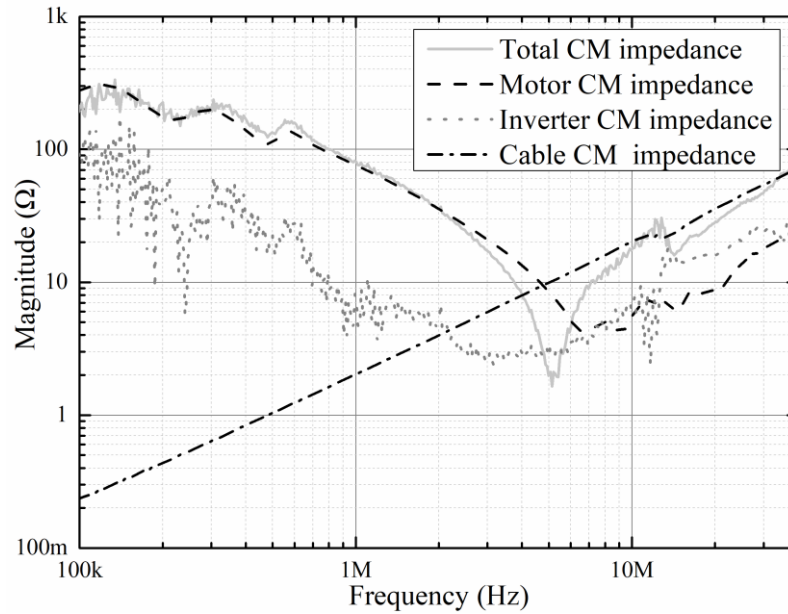
Fig. 4-12 Online extraction of the noise source (inverter) CM impedance.

By observing the frequency response of the noise source impedance, it is capacitive in nature at low frequency and becomes inductive as frequency increases. Such behavior is expected, as the insulation layer between the electronic devices and the grounded

heatsink and chassis formed a capacitance but the equivalent series inductance in the CM

path dominates with increasing frequency. Given the frequency response, the CM noise

source impedance can be represented by an equivalent series circuit of a 3 Ω resistor, a

95.5 nH inductor and a 19.9 nF capacitor.

Chapter 5   CM Filter Design

To suppress the CM current, a CM filter is preferred between the inverter and the induction motor. Usually, the designer will experiment with CM filters with different components and until the resulted CM current is below the required limit. Even if the designer can select off-the-shelf filters, he still has to experiment with different filters to achieve the desired attenuation.   However, such a trial-and-error process can be cumbersome. The extracted noise source impedance allows a CM filter to be designed systematically without overdesigning. In the evaluation of first order single-inductor and second order LC CM filters, it is found that the second order CM filter is prone to DM-to-CM conversion, especially at the resonant frequency caused by the leakage inductance of the CM choke and the equivalent DM capacitance of the line-to-ground capacitors. Therefore, an additional DM inductor is necessary to curb the mode conversion, which may not necessarily result in final size reduction as compared to that of first order single-inductor filter.

5.1   Determination of the filter attenuation

5.1.1   EMI standard

CM filters are inserted between the inverter and the induction motor to reduce the CM current at the inverter output side and the resulted circulating bearing current. Since the bearing impedance is dynamic and uncertain during operation, it's hard to quantify the limit of CM current for the bearing degradation. Therefore, in this study, a standard

suggested in DO 160, as shown in Fig. 5-1 is selected as a reference for the filter design. Most of the EMI requirements and limits for electrical motor drive systems are only applicable to the incoming power mains. With increasing trend of more sophisticated power conversion system, such as more electrical aircraft in aerospace applications, the EMI requirements are applicable to both power mains side, as well as load side, where DO160 is the most comprehensive standard with applicable limits based on their installed locations. Based on DO160 standard, the limit for our intended application is 72 to 40 dBμA for 150 kHz to 2 MHz, respectively; and 40 dBμA for 2 to 30 MHz. These limits are applicable to both the power mains side (Category B) and the load side (Category L, M and H). The full frequency range of DO160 conducted emission limit covers from 150 kHz to 152 MHz. As the in-circuit impedance extracted earlier is up to 30 MHz due to the bandwidth limitation of the inductive probes, the results to be presented here will be from 150 kHz to 30 MHz. Also, the conducted emission from an inverter driven motor drive expects to diminish above 30 MHz, and filter design up to 30 MHz is usually suffice.
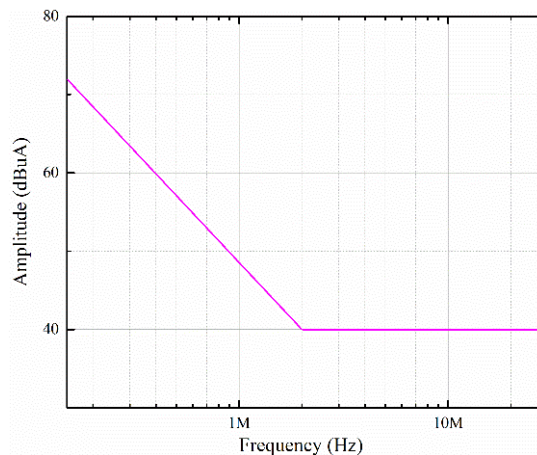
Fig. 5-1 Standard DO 160

Although the standard in DO 160 is typically used in the aerospace application, it can be used as a reference since the performance of a designed filter is independent of the

limit and the design methodology is pertinent for all the motor side CM filters in the motor drive system.

5.1.2 Experimental setup

Fig. 5-2 shows the 5.5 kW induction motor driven by a PWM inverter with a 5 m unshielded cable in between. Marked with the CM current path, Fig. 5-3 illustrates the system configuration, except an additional isolation transformer and a three-phase line impedance stabilization network. The LISN is to provide a well-defined main impedance as well as to prevent externally conducted emission from contaminating the measurement results. A mixed signal oscilloscope with a built-in spectrum analyzer (Tektronix MDO4104B-3) and a current probe (Solar Electronics 9134-1N, 100 MHz bandwidth) are selected for the CM current measurement at the output of the inverter.
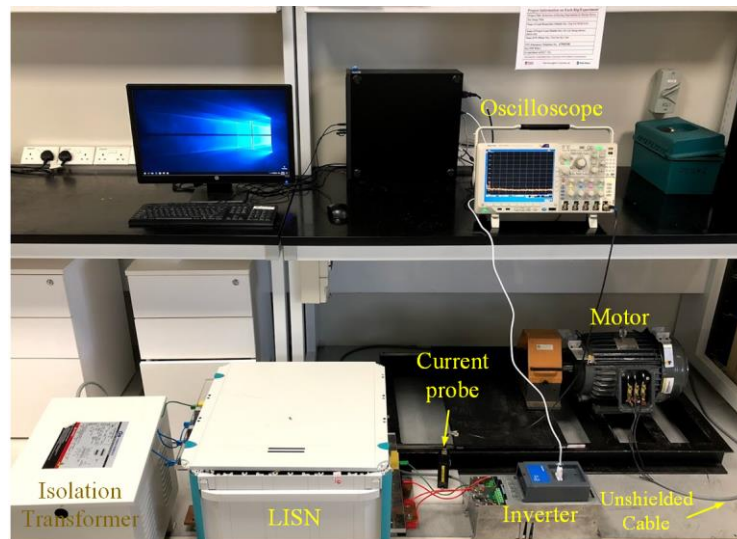
Fig. 5-2 5.5 kW induction motor driven by a PWM inverter.
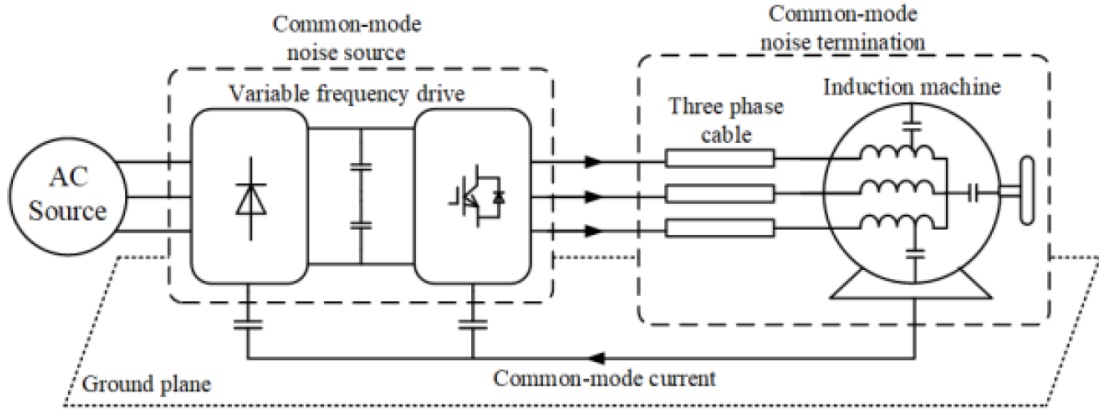
Fig. 5-3 CM current path of a motor drive system.

For the given inverter-driven motor drive, the conducted emission reference to be complied with is the DO160 standard. Fig. 5-4 shows the measured CM current without filter and it is obvious that the CM current fails to meet the required DO160 limit. The design target is to suppress the CM current below the limit with the smallest possible choke size.
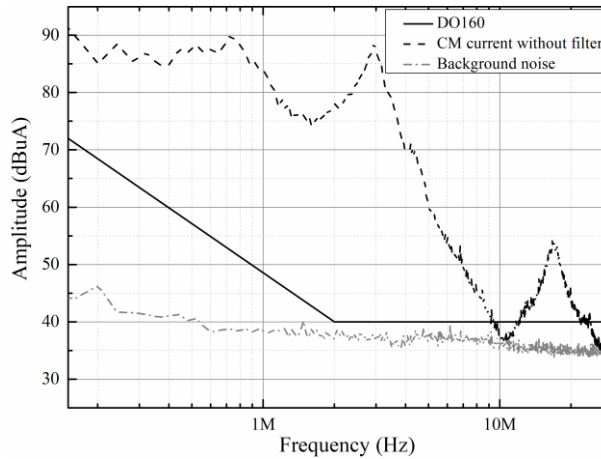
Fig. 5-4 Measured CM conducted emission without filter.

5.2 Design of CM choke

As a cost-effective method, three-phase CM chokes have been widely utilized for the AC power cable bundle between the inverter and the motor to suppress the CM noise

generated by the switching devices in order to meet certain regulations [68-72]. However, the size of the CM magnetic component could be a big issue as it can even take up to 25% of the system volume [73]. Thus, to avoid overdesign, the optimization of performance and size of CM inductors is necessary in the motor-drive system. Usually, the designer will experiment with CM chokes with different inductances and until the resulted CM current is below the required limit. Such a trial-and-error process can also lead to a final CM filter that meets the required attenuation. However, it takes a longer time to experiment and finalize the desired component value and has a tendency of overdesigning. In the case of high-power inverter-driven motor systems in the range of several hundred kW or higher, the CM chokes have to handle much high current rating and may not be readily available in the market. Several different values of CM chokes will have to be pre-designed and fabricated for trial-and-error, which can be costly and impractical.

Normalized attenuation is calculated in [74] for the optimization of CM chokes but the estimated attenuation could have large error since it assumes the inductance of the CM choke is always constant at both low frequency and high frequency. Reference [62] and [75] try to design a CM choke by simplifying the motor-drive system as a series LRC circuit but this simplification makes it impossible to predict the frequency response of the choke. Prediction of the choke performance requires prior knowledge of both noise source and termination impedances. Therefore, based on the online extracted inverter source impedance, this section introduces a step-by-step design methodology that leads to a specific value of CM choke in the early design phase before it is finally designed and fabricated.

5.2.1 Nanocrystalline magnetic cores

Nanocrystalline cores are widely adopted in the design of CM inductor due to their unique combination of properties [76-78]. Nanocrystalline core materials are well-known for their high magnetic flux saturation level and high permeability across the frequency range of interest [79]. In general, core material with high permeability is preferred to reduce the core size and the number of turns. Fig. 5-5 compares the real, imaginary and complex permeability of nanocrystalline material and the conventional ferrite material. For high-frequency modeling, it's very important to consider the complex permeability, $\mu^* = \mu' - j\mu''$, since real part of the impedance accounts for the major share of the attenuation and at high frequency the imaginary part of the complex permeability μ'' becomes dominant. At high frequency, the material becomes more resistive than inductive as the complex permeability angle arctan (μ''/μ') is larger than 45 degrees.

The permeability of nanocrystalline is significantly higher than that of ferrite in the low-frequency range and remains higher even at very high frequencies, which means it can help to reduce the volume of EMI filters notably. A magnetic core with high permeability provides high inductance with fewer turns but it is also prone to core saturation. There is always a trade-off between high permeability and core saturation, which is the reason why nanocrystalline core is chosen, as it has a high permeability, as well as a relatively high core saturation level. Toroid core shape is also preferred due to lower cost and higher effective permeability compared with other structures. Therefore, off-the-shelf magnetic cores made of nanocrystalline material VITROPERM from VAC are utilized for the choke design and Table 5-1 summarizes the core specs.

(a)   (b)
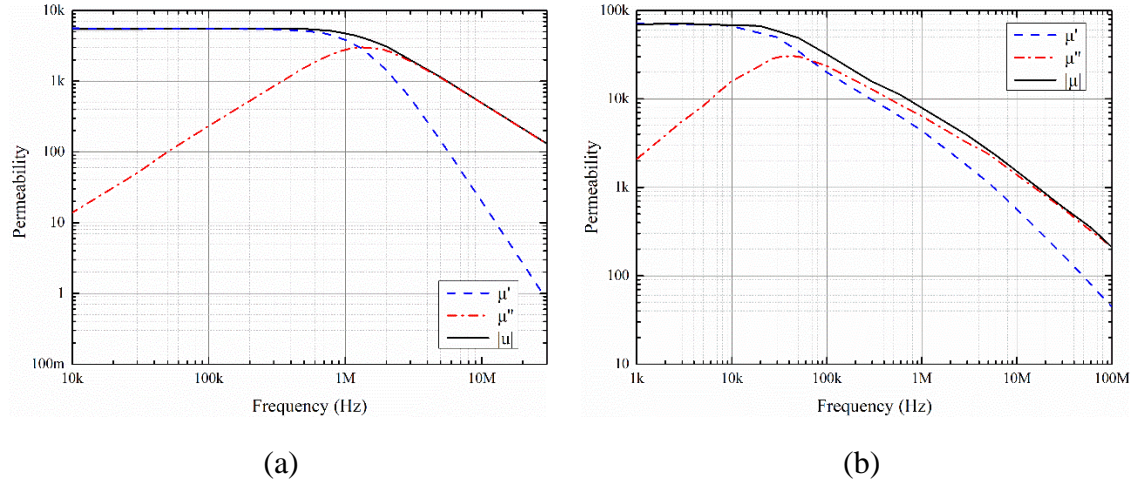
Fig. 5-5 Material properties: (a) Ferrite; (b) Nanocrystalline

Table 5-1 Parameters of nanocrystalline cores

No.	1	2	3	4	5
Magnetic core part no.	L2040-W424	L2050-W516	L2063-W517	L2090-W518	L2102-W947
Core outer diameter (mm)	40	50	63	90	102
Core inner diameter (mm)	25	40	50	60	76
Core height (mm)	15	20	25	20	25
Iron cross section (cm^2)	0.86	0.76	1.24	2.28	2.47
Mean path length(cm)	10.2	14.1	17.8	23.6	28
Weight(g)	64	79	161	395	508
Typical saturation current 10kHz(A)	0.5	1	1.2	1.7	4.9

5.2.2 Analytical estimation

Two critical frequencies are selected to give a quick estimation of the core size and the

number of turns based on analytical calculation before proceeding with the full-modeling

using finite element method (FEM). The first frequency is the lowest frequency specified by the DO160 standard, where its attenuation determined primarily by the choke inductance L_{CM}. The second frequency is at a higher frequency where the maximum attenuation is required. At this frequency, the real part of the choke impedance R_{CM} accounts for the major share of the attenuation because the imaginary part μ'' of the complex permeability becomes dominant.

Assuming the three-phase winding is symmetrical, and the core permeability is homogeneous, a lumped parameter L_{CM} can be used to represent the CM inductance of the choke which is a strong function of frequency [79]:

$$L_{CM}(f) = N_L^2 A_L \cdot \frac{\mu'(f)}{|\bar{\mu}(10\ kHz)|}$$ (5-1)

where N_L is the number of turns, A_L is the inductance per turn at a specific frequency of 10 kHz and μ' is the real part of the complex permeability $\bar{\mu}$.

Resistive part of the choke CM impedance is caused by the core loss and winding loss. Both are related to the frequency because the permeability and skin depth depends on the frequency value. The CM resistance at frequency f can be modeled by two resistors in series:

$$R_{CM}(f) = R_{core}(f) + \frac{1}{3}R_w(f)$$ (5-2)

where $R_{core}(f)$ is the associated resistance for core loss and $R_w(f)$ is the series winding resistance for each phase. Following [45], $R_{core}(f)$ can be modeled as

$$R_{core}(f) = 2\pi f N_L^2 A_L \cdot \frac{\mu''(f)}{|\bar{\mu}(10\ kHz)|}$$ (5-3)

where μ'' is the imaginary part of the complex permeability and $R_w(f)$ can be modeled

as [45]:

$$R_w(f) = \left(\frac{\pi}{4}\right)^{\frac{3}{4}} \cdot \frac{\sqrt{\phi_w^3}}{\delta\sqrt{d_{wires}}} \cdot \frac{4N_L l_t \rho_w}{\pi\phi_w^2} \tag{5-4}$$

$$\delta = \sqrt{\frac{\rho_w}{\pi\mu_0 f}} \tag{5-5}$$

where ϕ_w is the wire diameter, d_{wires} is the estimated distance between two adjacent conductors, l_t is the average length of one turn of the winding, ρ_w is the resistivity of the wire material and δ is the skin depth. This equation is valid only when the CM choke is designed on a single layer which is usually preferred so that the winding parasitic capacitance is low, and the proximity effect of the wire is negligible.

Without considering the stray capacitance, the total CM impedance of the choke at frequency f can be calculated as

$$Z_{CM}(f) = R_{core}(f) + \frac{1}{3}R_w(f) + j2\pi f L_{CM}(f) \tag{5-6}$$

Core loss resistance $R_{core}(f)$, copper loss resistance $R_w(f)$ and choke CM inductance $L_{CM}(f)$ are all frequency dependent and can be calculated following previous procedures. Therefore, $Z_{CM}(f)$ can be further written as:

$$Z_{CM}(f) = A \cdot N_L^2 + B \cdot N_L \tag{5-7}$$

$$A = 2\pi f A_L \cdot \frac{\mu''(f)}{|\bar{\mu}(10\ kHz)|} + j2\pi f A_L \cdot \frac{\mu'(f)}{|\bar{\mu}(10\ kHz)|} \tag{5-8}$$

$$B = \left(\frac{\pi}{4}\right)^{\frac{3}{4}} \cdot \frac{\sqrt{\phi_w^3}}{\delta\sqrt{d_{wires}}} \cdot \frac{4l_t \rho_w}{\pi\phi_w^2} \tag{5-9}$$

With the known information of the CM noise source, the CM choke and CM load termination, the CM filter attenuation can be determined. Fig. 5-6 shows the measured CM source and load termination impedances and the attenuation of the CM choke at

frequency f can be calculated with:

$$Att(f) = 20log \left| \frac{Z_S(f) + Z_L(f) + Z_{CM}(f)}{Z_S(f) + Z_L(f)} \right| \tag{5-10}$$

where $Z_S(f)$ and $Z_L(f)$ are the measured CM impedances of the source and load.
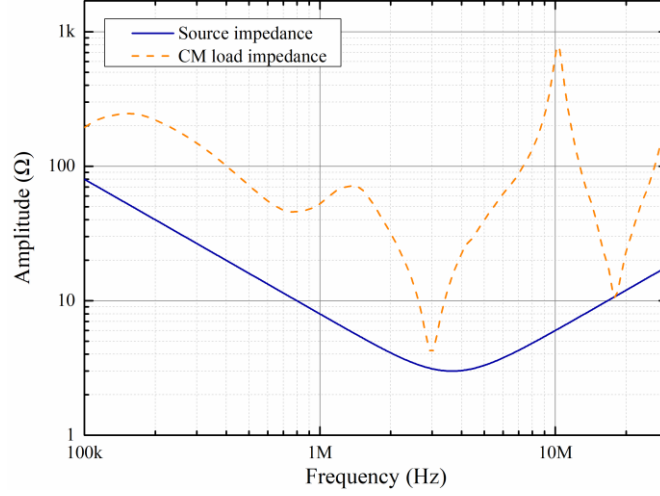
Fig. 5-6 Impedance of the CM source and CM load

Performance of the CM choke at the two selected frequencies have to meet the following requirement to achieve the desired attenuation:

$$20log \left| \frac{Z_S(f) + Z_L(f) + Z_{CM}(f)}{Z_S(f) + Z_L(f)} \right| \geq Att\_r(f) \tag{5-11}$$

where $Att\_r(f)$ is calculated by subtracting the DO160 limit from the measured CM emission as shown in Fig. 5-4. By substituting (5-7) into (5-11), the number of turns has to satisfy the following inequality:

$$|Z_S(f) + Z_L(f) + A \cdot N_L^2 + B \cdot N_L| \geq 10^{\frac{Att\_r(f)}{20}} \cdot |Z_S(f) + Z_L(f)| \tag{5-12}$$

Toroid core window area imposes another design constrain for the CM choke. The maximum number of turns is limited by the inner diameter of the core according to [80]:

$$N_L \leq \frac{(ID - D_w)\theta_{max}}{2D_w} \tag{5-13}$$

where D_w is the diameter of the wire, ID is the inner diameter of the core and θ_{max} is the maximum angle that one phase covers. If N_L obtained with (5-12) fails to fit the window area, a larger core should be chosen from the product list until N_L satisfies both (5-12) and (5-13). In some extreme cases, where there is no commercially available magnetic core with the suitable window or large inductance is needed without core saturation, two or more CM chokes can be added but at the expense of overall size.

5.2.3 FEM simulation

Parasitic capacitances of the CM choke, especially the winding-to-core capacitance degrades CM choke performance at a higher frequency. Thus, accurate prediction of the parasitic parameters is crucial in determining the attenuation of the CM choke in high frequency. High-frequency behavior modeling of the CM choke has been presented in [44, 81], but the choke parameters rely on the previous measurement results. In [80, 82], the total parasitic capacitance in the choke is modeled by a network of series and parallel connection of the turn-to-turn capacitance and the turn-to-core capacitance. This model considers the distribution of the choke winding and its parasitic capacitance but the proposed analytical estimation makes quite a lot assumptions and is only valid when the number of turns is larger than 10. Thus, a more accurate design is necessary using FEM (Ansys Maxwell).

In the CM filter design, core saturation is also an important consideration. The maximum magnetic flux density caused by the CM and DM currents together should be less than the saturation flux density of the core material. The peak value of the DM current can be directly measured or estimated from the rating of the power converter.

However, the estimation of the CM current is not as straightforward, as it depends not only on the operating system but also on the CM filter performance. Therefore, the estimation of maximum flux density in the core have to be calculated with FEM simulation based on the measured CM and DM currents when the CM filter is tested. In the design stage, only the DM current at the critical frequency range is considered, where the magnetic fluxes due to DM currents do not cancel completely [83].

As a summary, the proposed CM choke design procedure is shown in Fig. 5-7. Once the core size and the number of turns are finalized, the CM choke can be fabricated accordingly.

Input $Z_S(f)$, $Z_L(f)$ and $Att\_r(f)$

Increase core size

Select a relatively small core

Estimate N_L based on the attenuation at the selected two frequencies

N_L fit the window area? N

N_L fit the window area? N / Y

Increase N_L

FEM simulation and calculation of the overall attenuation

Satisfy $Att\_r(f)$? N / Y

Simulated flux density less than B_{sat} ? N / Y

Fabricate the choke for field test
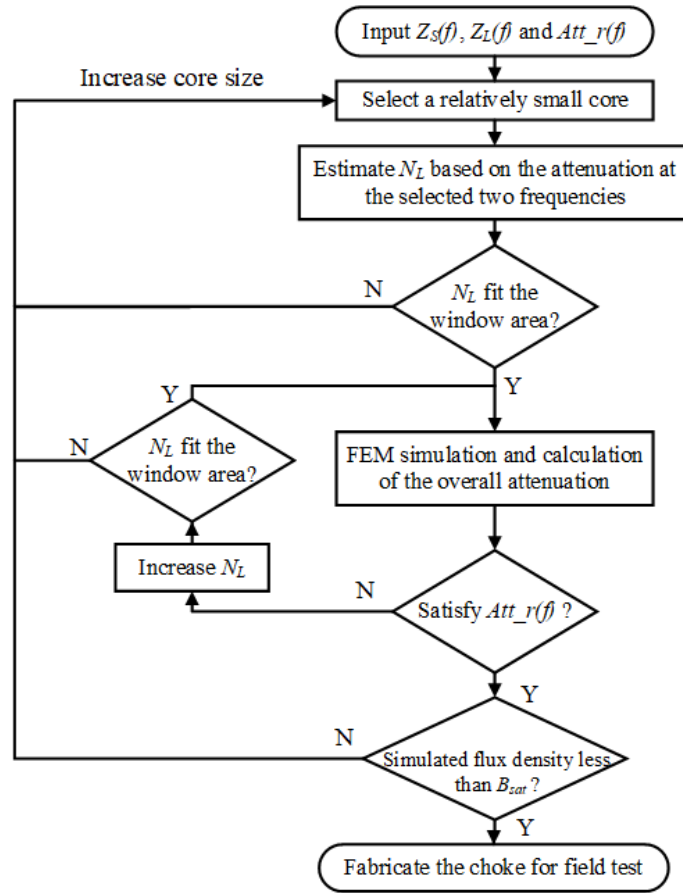
Fig. 5-7 Proposed design procedure for the CM choke.

Based on the above-mentioned procedure, a CM choke with magnetic core VAC L2090-W518 and 10 turns per coil is designed for the motor drive system. The measured inductance of the choke at 10 kHz is 7 mH. Fig. 5-8 shows the FEM model of this choke and the refined mesh after iteration is also plotted in the figure.
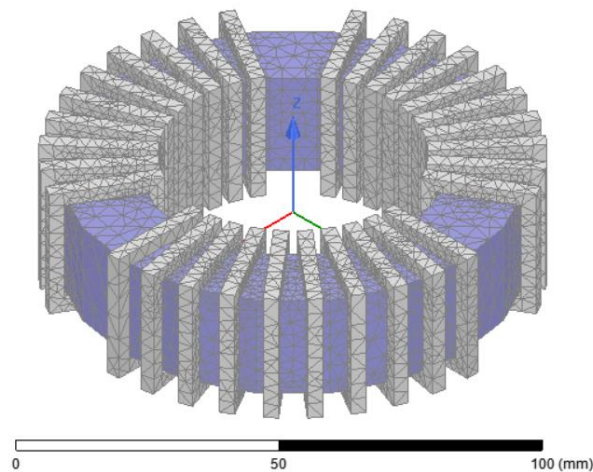
Fig. 5-8 FEM modeling of the designed CM choke

Fig. 5-9 compares the simulated CM impedance of the designed choke using FEM and the measurement result with an impedance analyzer. It shows that the simulated impedance agrees rather well with the measured impedance.
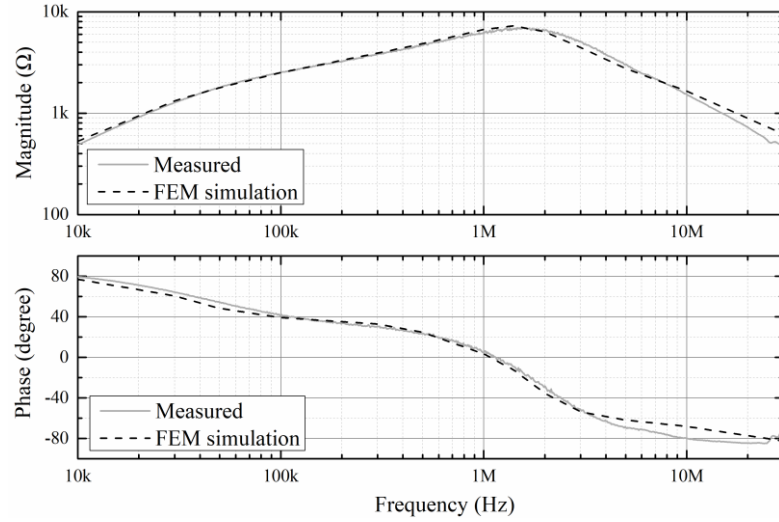
Fig. 5-9 Measured and simulated CM impedance of the designed choke

Based on choke impedance obtained from FEM simulation, the core's attenuation versus frequency is calculated and shown in Fig. 5-10 as the dashed line, which is higher than the required attenuation over the given frequency range. The effectiveness of the designed choke is validated with the measurement result shown in Fig. 5-11, where the CM current with the choke added is much lower and within the limit.
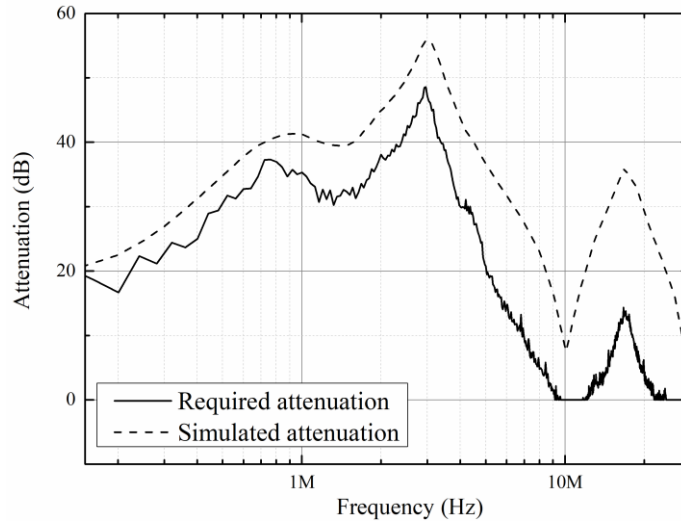
Fig. 5-10 Simulated and required CM attenuations
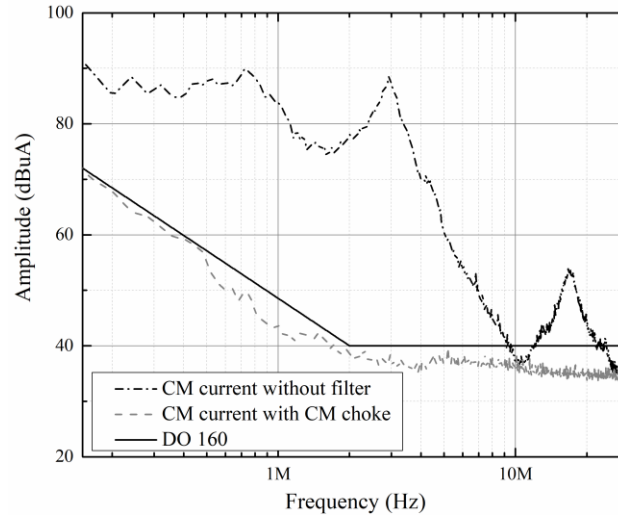
Fig. 5-11 Measured CM current

With known CM and DM peak currents, the resultant maximum magnetic flux density within the core is calculated using FEM as shown in Fig. 5-12. It shows that the maximum flux density is 0.27 T, which is far below the saturation flux density of nanocrystalline 500F (1.2 T). Therefore, the designed choke will not suffer from the flux saturation issue.
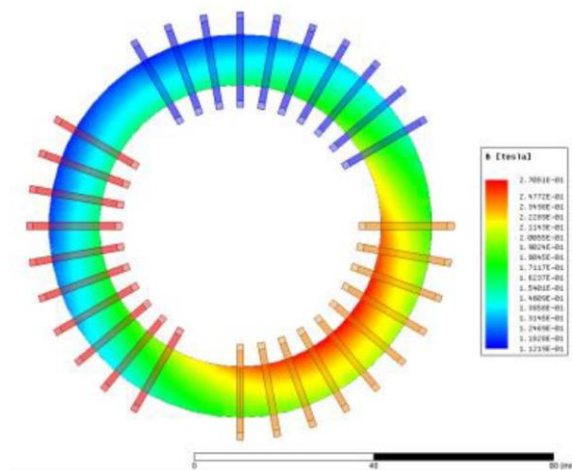
Fig. 5-12 Resultant magnetic flux density under known CM and DM peak currents.

This case study based on a 5.5 kW induction motor has confirmed that the online extracted noise source impedance can lead to a systematic CM inductor design approach

without the usual trial-and-error. Analytical estimation and FEM simulation help to choose the core size and the number of turns thus the desired attenuation can be achieved by a CM inductor with minimized size.

5.3   Second-order filter

Although the first order filter with a CM choke is able to bring the emission below the limit, the design of a second order LC filter is explored with the intention to reduce the size of the CM choke for a more compact filter. However, it is found that the second order CM filter is prone to the DM-to-CM conversion.

5.3.1   Measurement of the LC filters

A CM choke of 1.5 mH is selected with three Y-capacitors added and grounded via a 22 Ω damping resistor [80], as shown in Fig. 5-13.
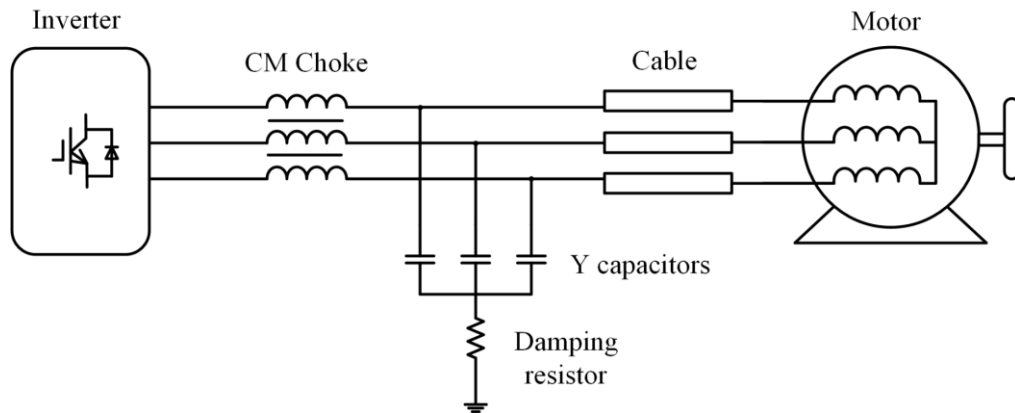
Fig. 5-13 Setup for the output-side second-order LC filter

The CM emissions for the second order filter with two different values of Y-capacitors (1 nF and 4.7 nF) are measured and shown in Fig. 5-14. Ideally, higher attenuation is expected from the second order filter as compared to the 1.5 mH CM choke alone.

Interestingly, it is observed that the second order filter exhibits higher CM emissions at some frequencies. For investigation purpose, the DM emissions are also measured and shown in Fig. 5-14. It reveals that the frequencies where higher CM emissions are observed are related to the resonant frequencies of DM emissions, as marked with the vertical dotted lines in Fig. 5-14. It indicates that there is a strong DM-to-CM conversion at these resonant frequencies, which is caused by the CM choke leakage inductance and the CM capacitors in the second order LC filters [84-86] but not so for the case of the CM choke alone.
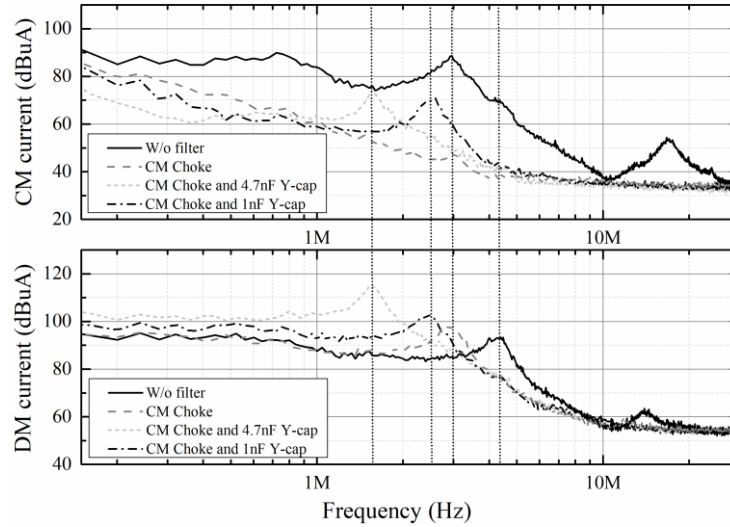
Fig. 5-14 The CM and DM emissions for different filter configurations

5.3.2   Simulation of the mode conversion

Unbalanced parameters in an EMI filter, as well as the unbalanced source and load terminations can lead to mode conversion, as reported in [87-90]. To better understand the mode conversion, a simulation model shown in Fig. 5-15 demonstrates how the imbalance impedance of the induction motor converts to CM current under a DM excitation. In the model, C_{inv} is the stray capacitance of the switching devices, $L_{leakage}$

is the leakage inductance of the CM choke and C_y is the CM capacitors between each phase and ground. An electrical model of a three-phase motor [91] is also included in the model for simulation purpose. The CM current is simulated with an emulated imbalance by a small variation of 2.5 % and 5% for the winding stray capacitance C_{wf} and winding inductance L_w. The results in Fig. 5-16 shows the DM to CM noise conversion with the imbalance impedance of the induction motor.
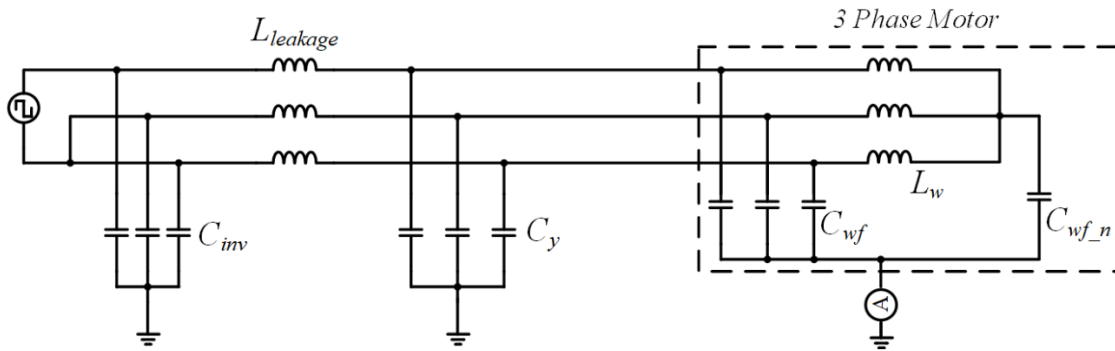
Fig. 5-15 Demonstration of DM-to-CM noise conversion through simulation
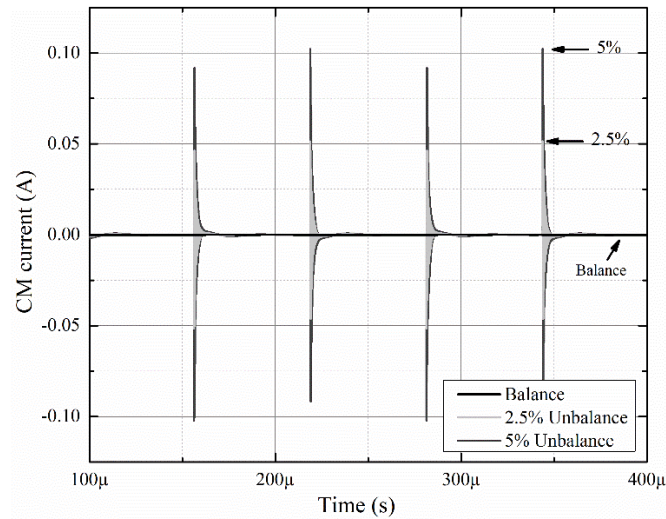
Fig. 5-16 Simulated CM current results with only DM excitation

With the in-circuit extracted source impedance, quantitative analysis of CM filter attenuation becomes feasible. It can also be used to show whether there is any mode transformation that degrades the CM filter performance.

5.3.3 Mode transformation in an LC filter

Based on the aforementioned noise source and load impedance, one can evaluate the effect of the mode transformation on the CM filter design quantitatively. Take the second order LC filter with 1.5 mH CM choke and 1 nF Y-capacitors for further study, the attenuation provided by the LC filter can be estimated by:

$$Att = 20log \left| \frac{Z_L(Z_S + Z_{CMC} + (Z_{Y-cap} + Z_{damping})||Z_L)}{(Z_S + Z_L)((Z_{Y-cap} + Z_{damping})||Z_L)} \right| \qquad (5\text{-}6)$$

where Z_{Y-cap} is the CM equivalent impedance of the 1nF capacitor branches and $Z_{damping}$ is the impedance of the damping resistor. The parasitic effects of the components have already been included based on their respective measured impedance responses. The impedance frequency responses of these components are substituted into equation (5-6) to compute the CM filter attenuation. The observed DM-to-CM conversion leads to a discrepancy between the calculated and measured results, as shown in Fig. 5-19(a). For the LC filter to function without the influence of mode conversion, a suitable value of DM inductor has to be added, as shown in Fig. 5-17.
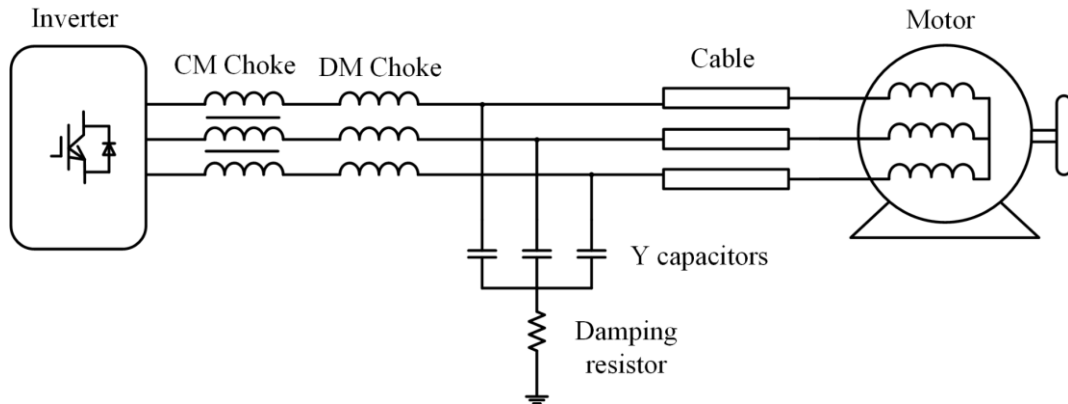
Fig. 5-17 Setup for the output-side LC filter with addition DM inductor

Fig. 5-19(a) shows the calculated and measured CM attenuation of the designed second order filter. The measured attenuation matches rather well with the calculated attenuation, except at 2.6 MHz, where the measured attenuation is 26 dB below the calculated attenuation. It indicates that there is a DM-to-CM conversion of about 26 dB at 2.6 MHz. It means that the DM emission must be suppressed by at least 26 dB at 2.6 MHz. With a 6 dB margin, the required DM attenuation by adding a DM inductor must be 32 dB at 2.6 MHz. The DM attenuation with the additional DM inductor can be computed by comparing the DM emission with and without the DM inductor, given by:

$$Att\_DM = 20log \left| \frac{Z_{L\_DM} + Z_\sigma + Z_{S\_DM} + Z_{cap}||Z_{load\_DM}}{Z_\sigma + Z_{S\_DM} + Z_{cap}||Z_{load\_DM}} \right| \qquad (5\text{-}7)$$

where Z_{L_DM} is the DM impedance of the DM inductor, Z_σ is the leakage impedance of the CM inductor, Z_{S_DM} is the measured DM source impedance, Z_{cap} is the equivalent DM impedance of the Y-capacitors and Z_{load_DM} is the DM load impedance. Based on the in-circuit impedance extraction method, these DM impedances are measured and plotted in Fig. 5-18.
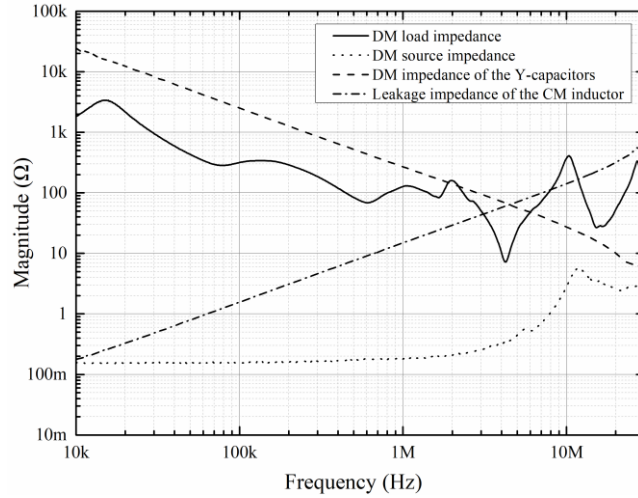
Fig. 5-18 DM impedances of source, load, Y-capacitors and leakage inductance of the CM choke

From (5-7), the calculated DM inductor is found to be 25 µH. A commercially available 30 µH DM inductor is selected. Compared with the CM choke, this DM inductor has negligible CM impedance but it is also included when calculating the CM attenuation as follows:

$$Att = 20log \left| \frac{Z_L(Z_S + Z_{CMC} + Z_{DMC} + (Z_{Y-cap} + Z_{damping})||Z_L)}{(Z_S + Z_L)((Z_{Y-cap} + Z_{damping})||Z_L)} \right| \qquad (5\text{-}7)$$

where Z_{DMC} is the CM impedance of the DM inductor.

The performance of the LC filter (CM choke and three 1 nF capacitors with a 22 Ω damping resistor) without and with the DM inductor are shown in Figs. 5-19 (a) and (b), respectively. Although the CM impedance of the DM inductor contributes little in the CM attenuation, it plays a crucial role by controlling the DM-to-CM conversion and thus the measured attenuation in Fig.5-19 (b) is a much higher than that in Fig. 5-19 (a).
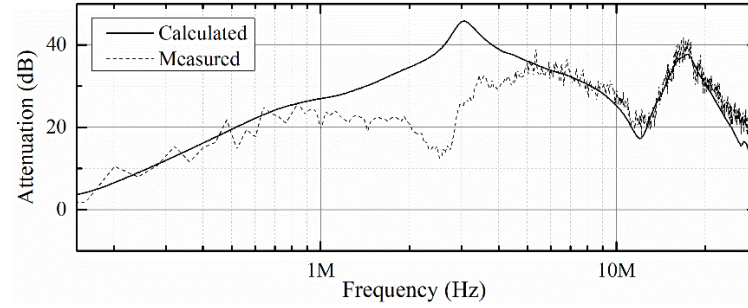
(a)
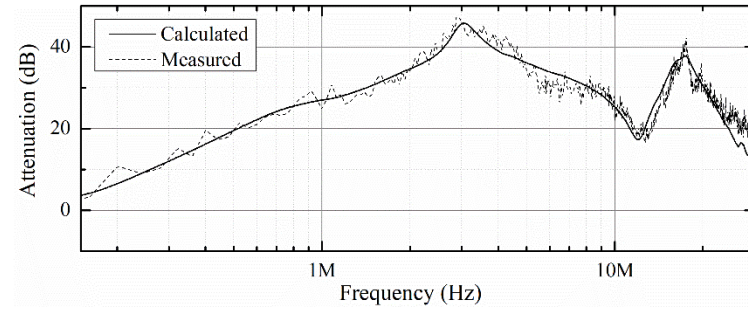
(b)

Fig. 5-19 Calculated and measured attenuation for the LC filter. (a) Without DM inductor. (b) With additional DM inductor.

Due to the asymmetry of motor drive system, DM-to-CM conversion has a significant impact on the CM filter performance of the second-order LC filters, which could lead to the discrepancy between the designed and measured attenuation of the filters. Thus, the second order CM filter may not necessarily lead to a more compact CM filter due to the need of an additional DM inductor to suppress the mode conversion.

Chapter 6 Conclusion and Future Work

6.1　Conclusion

Inverter-driven induction motors often suffer from premature bearing failure due to the high-frequency CM voltage and induced CM current. This thesis discusses the high-frequency simulations of single- and three-phase induction motor circuits under PWM operation. High-frequency simulations are important in providing a valuable insight into the motor's CM and DM behaviour. A controlled switch is integrated into the high-frequency model to study the bearing discharge process. EDM process is observed in the simulation and a parameter analysis is performed to understand the influence of bearing capacitance on the bearing discharge. Bearing degradation problem is also investigated experimentally and the result shows that CM voltage capacitively induces a high-frequency bearing voltage which has the potential to penetrate the bearing lubrication film while CM current drives a circulating type bearing current. Therefore, CM filter is suggested for high-power motors where the circulating bearing current is dominant, like in marine applications. Performance of a CM filter is also examined and the difference between calculation and measurement illustrates the necessity of online extraction of source impedance for filter optimization.

Existing in-circuit impedance measurement approaches have been reviewed comprehensively. This thesis proposed an inductive coupling approach with the ability to extract online impedance in a high-power noisy system. As compared with

conventional impedance measurement method, the merit of the proposed approach is summarized below:

- Front-end-protection of the VNA device is provided to avoid the damage of measurement ports caused by the fast switching of IGBTs in the motor drive system.

- Higher SNR is achieved to ensure reliable measurement results with good confidence for high-power systems with high background noise.

Information of the in-circuit noise source and load termination impedances of the motor drive system is the precondition of CM filter design. It allows an optimized CM choke to be designed systematically without the usual trial-and-error approach. With the known desired noise attenuation, two critical frequencies are selected to give a quick estimation of the core size and the number of turns based on analytical calculation, and then the full-modeling using finite element method provides more accurate evaluation of the choke performance. This design procedure is first described and then validated experimentally with a 5.5 kW motor drive system. Also, based on the noise source and load impedance, it is possible to evaluate the effect of the mode transformation on the CM filter design quantitatively.

6.2   Future Work

Based on the proposed online impedance measurement approach for the high-power noisy system, the following future work is worth exploring:

- Any fault of the stator winding will be reflected in the impedance difference and resonance shift. Therefore, proposed method can be applied in the condition monitoring of the motor stator winding by measuring both CM and DM impedance.

- Mode transformation in the filter design could be investigated with the detailed information of both load and termination impedance. The parasitic capacitance and the mutual inductance of the filter components need to be carefully modeled.

- Study the feasibility of the proposed method in an on-site marine system to select a proper filter for the MW motor with thick cables.

AUTHOR'S PUBLICATIONS

Journal Publications

1. F. Fan, K. Y. See, J. K. Banda, et al. "Investigation and Mitigation of Premature Bearing Degradation in Motor Drive System", *IEEE Electromagnetic Compatibility Magazine*, vol. 8, no. 1, pp. 75-81, 2019.
2. F. Fan, K. Y. See, K. R. Li, et al. "Systematic Common-Mode Filter Design for Inverter-Driven Motor System based on In-Circuit Impedance Extraction", *IEEE Transactions on Electromagnetic Compatibility,* accepted for publication.
3. K. R. Li, K. Y. See, F. Fan and N. B. Narampanawe, "Condition Monitoring of High Power DC Feeder with Multiple Parallel Cables," *IEEE Transactions on Power Delivery*, accepted for publication.

Conference Publications

1. T. Svimonishvili, F. Fan, K. Y. See, et al. "High-Frequency Model and Simulation for the Investigation of Bearing Current in Inverter-Driven Induction Machines", *IEEE Region 10 Conference*, pp. 55-59, 2016.
2. F. Fan, K. Y. See K Y, K. R. Li, et al. "In-Circuit Common-Mode Impedance Measurement for Motor Drive System", *Asia-Pacific International Symposium on Electromagnetic Compatibility*, pp. 1-3, Seoul, 2017. (Awarded Best Student Paper)
3. K. R. Li, K. Y. See and F. Fan, "Study of EMI Filter Performance without LISN based on Noise Impedances", *Asia-Pacific International Symposium on Electromagnetic Compatibility*, pp. 115-117, Seoul, 2017.
4. F. Fan, K. Y. See, J. K. Banda J K, et al. "Simulation of Three-Phase Motor Drive System with Bearing Discharge Process", *Progress in Electromagnetics Research Symposium*, pp. 2091-2097, Singapore, 2017. (Awarded Best Student Paper)
5. Z. X. Wang, F. Fan, J. S. Lam, K. Y. See, et al. "Reduction of common mode voltage of 2-level voltage source inverter-fed machine", *IEEE Asian Conference on Energy, Power and Transportation Electrification*, pp. 1-5, Singapore, 2017.
6. F. Fan, K. Y. See, K. R. Li, et al. "Efficient Inductive Coupled In-Circuit Impedance Extraction with Enhanced SNR and Instrument Protection", *Joint IEEE International Symposium on Electromagnetic Compatibility and Asia-Pacific Symposium on Electromagnetic Compatibility*, pp. 1288-1292, Singapore, 2018.
7. Y. Liu, F. Fan, K. Y. See, et al. "Switching Devices Comparison and RC Snubber for Ringing Suppression in one Single Leg T-type Converter", *IEEE Asian Conference on Energy, Power and Transportation Electrification*, pp. 1-5, Singapore, 2018.

REFERENCES

[1]   D. Busse, J. Erdman, R. J. Kerkman, D. Schlegel, and G. Skibinski, "System electrical parameters and their effects on bearing currents," *IEEE Transactions on Industry Applications,* vol. 33, no. 2, pp. 577-584, 1997.

[2]   U. T. Shami and H. Akagi, "Identification and Discussion of the Origin of a Shaft End-to-End Voltage in an Inverter-Driven Motor," *IEEE Transactions on Power Electronics,* vol. 25, no. 6, pp. 1615-1625, 2010.

[3]   F. Blaabjerg, U. Jaeger, and S. Munk-Nielsen, "Power losses in PWM-VSI inverter using NPT or PT IGBT devices," *IEEE Transactions on Power Electronics,* vol. 10, no. 3, pp. 358-367, 1995.

[4]   B. J. Baliga, M. S. Adler, R. P. Love, P. V. Gray, and N. D. Zommer, "The insulated gate transistor: A new three-terminal MOS-controlled bipolar power device," *IEEE Transactions on Electron Devices,* vol. 31, no. 6, pp. 821-828, 1984.

[5]   H. Shim *et al.*, "Analysis of high frequency characteristics of power inverter using accurate IGBT model based on datasheet and measurement," in *2015 IEEE Electrical Design of Advanced Packaging and Systems Symposium (EDAPS)*, 2015, pp. 81-84.

[6]   S. Castagno, R. D. Curry, and E. Loree, "Analysis and Comparison of a Fast Turn-On Series IGBT Stack and High-Voltage-Rated Commercial IGBTS," *IEEE Transactions on Plasma Science,* vol. 34, no. 5, pp. 1692-1696, 2006.

[7]   K. Yamaguchi, K. Katsura, and T. Jikumaru, "Motor loss and temperature reduction with high switching frequency SiC-based inverters," in *2017 IEEE 5th Workshop on Wide Bandgap Power Devices and Applications (WiPDA)*, 2017, pp. 127-131.

[8]   P. v. Vugt, R. Bijman, R. B. Timens, and F. Leferink, "Impact of grounding and filtering on power insulation monitoring in insulated terrestrial power networks," in *2013 International Symposium on Electromagnetic Compatibility*, 2013, pp. 472-477.

[9]   A. Muetze and A. Binder, "Don't lose your bearings," *IEEE Industry Applications Magazine,* vol. 12, no. 4, pp. 22-31, 2006.

[10]   M. J. Costello, "Shaft voltages and rotating machinery," *IEEE Transactions on Industry Applications,* vol. 29, no. 2, pp. 419-426, 1993.

[11]   C. Shaotang and T. A. Lipo, "Bearing currents and shaft voltages of an induction motor under hard- and soft-switching inverter excitation," *IEEE Transactions on Industry Applications,* vol. 34, no. 5, pp. 1042-1048, 1998.

[12]   R. R. Schoen, T. G. Habetler, F. Kamran, and R. G. Bartfield, "Motor bearing damage detection using stator current monitoring," *IEEE Transactions on Industry Applications,* vol. 31, no. 6, pp. 1274-1279, 1995.

[13]   D. Han, W. Lee, S. Li, and B. Sarlioglu, "New Method for Common Mode Voltage Cancellation in Motor Drives: Concept, Realization, and Asymmetry Influence," *IEEE Transactions on Power Electronics,* vol. 33, no. 2, pp. 1188-1201, 2018.

[14] M. H. Hedayati, A. B. Acharya, and V. John, "Common-Mode Filter Design for PWM Rectifier-Based Motor Drives," *IEEE Transactions on Power Electronics,* vol. 28, no. 11, pp. 5364-5371, 2013.

[15] A. Romanenko, A. Muetze, and J. Ahola, "Effects of Electrostatic Discharges on Bearing Grease Dielectric Strength and Composition," *IEEE Transactions on Industry Applications,* vol. 52, no. 6, pp. 4835-4842, 2016.

[16] S. Bhattacharya, L. Resta, D. M. Divan, and D. W. Novotny, "Experimental comparison of motor bearing currents with PWM hard- and soft-switched voltage-source inverters," *IEEE Transactions on Power Electronics,* vol. 14, no. 3, pp. 552-562, 1999.

[17] A. M. Hava and E. Ün, "A High-Performance PWM Algorithm for Common-Mode Voltage Reduction in Three-Phase Voltage Source Inverters," *IEEE Transactions on Power Electronics,* vol. 26, no. 7, pp. 1998-2008, 2011.

[18] Y. Tang, H. Zhu, B. Song, J. S. Lai, and C. Chen, "EMI experimental comparison of PWM inverters between hard- and soft-switching techniques," in *Power Electronics in Transportation (Cat. No.98TH8349)*, 1998, pp. 71-77.

[19] W. Zaixing *et al.*, "Reduction of common mode voltage of 2-level voltage source inverter-fed machine," in *2017 Asian Conference on Energy, Power and Transportation Electrification (ACEPT)*, 2017, pp. 1-5.

[20] F. Luo, D. Dong, D. Boroyevich, P. Mattavelli, and S. Wang, "Improving High-Frequency Performance of an Input Common Mode EMI Filter Using an Impedance-Mismatching Filter," *IEEE Transactions on Power Electronics,* vol. 29, no. 10, pp. 5111-5115, 2014.

[21] C. Jettanasen, "Passive common-mode EMI filter adapted to an adjustable-speed AC motor drive," in *2010 Conference Proceedings IPEC*, 2010, pp. 1025-1030.

[22] R. F. Schiferl, M. J. Melfi, and J. S. Wang, "Inverter driven induction motor bearing current solutions," in *Record of Conference Papers. Industry Applications Society. Forty-Ninth Annual Conference. 2002 Petroleum and Chemical Industry Technical Conference*, 2002, pp. 67-75.

[23] C. F. Hall, D. L. Knox, and B. D. Leamy, "Insulated bearings for downhole motors," ed: Google Patents, 2011.

[24] O. Magdun, Y. Gemeinder, and A. Binder, "Prevention of harmful EDM currents in inverter-fed AC machines by use of electrostatic shields in the stator winding overhang," in *IECON 2010-36th Annual Conference on IEEE Industrial Electronics Society*, 2010, pp. 962-967: IEEE.

[25] H. W. Oh and A. H. Willwerth, "New motor design with conductive micro fiber shaft grounding ring prevents bearing failure in PWE inverter driven motors," in *2007 Electrical Insulation Conference and Electrical Manufacturing Expo*, 2007, pp. 240-246.

[26] R. L. Ozenbaugh and T. M. Pullen, *EMI filter design*. CRC press, 2000.

[27] B. Mirafzal, G. L. Skibinski, R. M. Tallam, D. W. Schlegel, and R. A. Lukaszewski, "Universal Induction Motor Model With Low-to-High Frequency-Response Characteristics," *IEEE Transactions on Industry Applications,* vol. 43, no. 5, pp. 1233-1246, 2007.

[28]   H. Chen, Y. Yan, and H. Zhao, "Extraction of Common-Mode Impedance of an Inverter-Fed Induction Motor," *IEEE Transactions on Electromagnetic Compatibility,* vol. 58, no. 2, pp. 599-606, 2016.

[29]   W. Shen, F. Wang, D. Boroyevich, V. Stefanovic, and M. Arpilliere, "Optimizing EMI filter design for motor drives considering filter component high-frequency characteristics and noise source impedance," in *Nineteenth Annual IEEE Applied Power Electronics Conference and Exposition, 2004. APEC '04.*, 2004, vol. 2, pp. 669-674 vol.2.

[30]   H. Rebholz and S. Tenbohlen, "Prospects and limits of common- and differential-mode separation for the filter development process," in *2008 International Symposium on Electromagnetic Compatibility - EMC Europe*, 2008, pp. 1-6.

[31]   K. R. Li, K. Y. See, and X. M. Li, "Inductive Coupled In-Circuit Impedance Monitoring of Electrical System Using Two-Port <italic>ABCD</italic> Network Approach," *IEEE Transactions on Instrumentation and Measurement,* vol. 64, no. 9, pp. 2489-2495, 2015.

[32]   F. Fan, K. Y. See, K. Li, X. Liu, M. A. Zagrodnik, and A. K. Gupta, "In-circuit common-mode impedance measurement for motor drive system," in *2017 Asia-Pacific International Symposium on Electromagnetic Compatibility (APEMC)*, 2017, pp. 1-3.

[33]   A. Kempski, R. Strzelecki, R. Smolenski, and Z. Fedyczak, "Bearing current path and pulse rate in PWM-inverter-fed induction," in *2001 IEEE 32nd Annual Power Electronics Specialists Conference (IEEE Cat. No.01CH37230)*, 2001, vol. 4, pp. 2025-2030 vol. 4.

[34]   A. Muetze and A. Binder, "Techniques for Measurement of Parameters Related to Inverter-Induced Bearing Currents," *IEEE Transactions on Industry Applications,* vol. 43, no. 5, pp. 1274-1283, 2007.

[35]   A. Muetze and A. Binder, "Practical Rules for Assessment of Inverter-Induced Bearing Currents in Inverter-Fed AC Motors up to 500 kW," *IEEE Transactions on Industrial Electronics,* vol. 54, no. 3, pp. 1614-1622, 2007.

[36]   D. Busse, J. Erdman, R. J. Kerkman, D. Schlegel, and G. Skibinski, "Bearing currents and their relationship to PWM drives," *IEEE Transactions on Power Electronics,* vol. 12, no. 2, pp. 243-252, 1997.

[37]   D. Macdonald and W. Gray, "A practical guide to understanding bearing damage related to PWM drives," in *Conference Record of 1998 Annual Pulp and Paper Industry Technical Conference (Cat. No.98CH36219)*, 1998, pp. 159-165.

[38]   M. Kriese, E. Wittek, S. Gattermann, H. Tischmacher, G. Poll, and B. Ponick, "Influence of bearing currents on the bearing lifetime for converter driven machines," in *2012 XXth International Conference on Electrical Machines*, 2012, pp. 1735-1739.

[39]   C. Shaotang and T. A. Lipo, "Circulating type motor bearing current in inverter drives," *IEEE Industry Applications Magazine,* vol. 4, no. 1, pp. 32-38, 1998.

[40]   A. Drives, "Technical guide No. 5-Bearing Currents in modern AC drive systems," ed: Accessed on, 2014.

[41]   P. T. Finlayson, "Output filters for PWM drives with induction motors," *IEEE Industry Applications Magazine,* vol. 4, no. 1, pp. 46-52, 1998.

[42] P. Pairodamonchai, S. Suwankawin, and S. Sangwongwanich, "Design and Implementation of a Hybrid Output EMI Filter for High-Frequency Common-Mode Voltage Compensation in PWM Inverters," *IEEE Transactions on Industry Applications,* vol. 45, no. 5, pp. 1647-1659, 2009.

[43] H. Chung, S. Y. R. Hui, and K. K. Tse, "Reduction of power converter EMI emission using soft-switching technique," *IEEE Transactions on Electromagnetic Compatibility,* vol. 40, no. 3, pp. 282-287, 1998.

[44] I. Stevanovic, S. Skibin, M. Masti, and M. Laitinen, "Behavioral Modeling of Chokes for EMI Simulations in Power Electronics," *IEEE Transactions on Power Electronics,* vol. 28, no. 2, pp. 695-705, 2013.

[45] M. L. Heldwein, L. Dalessandro, and J. W. Kolar, "The Three-Phase Common-Mode Inductor: Modeling and Design Issues," *IEEE Transactions on Industrial Electronics,* vol. 58, no. 8, pp. 3264-3274, 2011.

[46] J. Kalaiselvi and S. Srinivas, "Bearing Currents and Shaft Voltage Reduction in Dual-Inverter-Fed Open-End Winding Induction Motor With Reduced CMV PWM Methods," *IEEE Transactions on Industrial Electronics,* vol. 62, no. 1, pp. 144-152, 2015.

[47] G. Vidmar, B. Štibelj, B. Rihtarsic, M. Zagirnyak, and D. Miljavec, "Evaluation of different mitigation techniques for electromagnetic interference caused by common mode voltage in BLDC outer-rotor motor," in *2012 15th International Power Electronics and Motion Control Conference (EPE/PEMC)*, 2012, pp. DS1c.3-1-DS1c.3-5.

[48] A. Muetze and H. W. Oh, "Design Aspects of Conductive Microfiber Rings for Shaft-Grounding Purposes," *IEEE Transactions on Industry Applications,* vol. 44, no. 6, pp. 1749-1757, 2008.

[49] Schaffner. (2013). *Sine wave filter solutions for motor drive applications*. Available: https://www.schaffner.com/fileadmin/media/downloads/applicatioschaffnern_note/Schaffner_AN_Filter_solutions_for_motor_drives_applications.pdf

[50] V. Tarateeraseth, K. Y. See, F. G. Canavero, and R. W. Chang, "Systematic Electromagnetic Interference Filter Design Based on Information From In-Circuit Impedance Measurements," *IEEE Transactions on Electromagnetic Compatibility,* vol. 52, no. 3, pp. 588-598, 2010.

[51] M. J. Nave, "Power Line Filter Design for Switched Mode Power Supplies," 1991.

[52] Y. Gemeinder, M. Schuster, B. Radnai, B. Sauer, and A. Binder, "Calculation and validation of a bearing impedance model for ball bearings and the influence on EDM-currents," in *2014 International Conference on Electrical Machines (ICEM)*, 2014, pp. 1804-1810.

[53] S. Kye Yak and D. Junhong, "Measurement of noise source impedance of SMPS using a two probes approach," *IEEE Transactions on Power Electronics,* vol. 19, no. 3, pp. 862-868, 2004.

[54] K. Li, K. See, and F. Fan, "Study of EMI filter performance without LISN based on noise impedances," in *2017 Asia-Pacific International Symposium on Electromagnetic Compatibility (APEMC)*, 2017, pp. 115-117.

[55] T. Svimonishvili, F. Fan, K. Y. See, X. Liu, M. A. Zagrodnik, and A. K. Gupta, "High-frequency model and simulation for the investigation of bearing current in

inverter-driven induction machines," in *2016 IEEE Region 10 Conference (TENCON)*, 2016, pp. 55-59.

[56]   B. Mirafzal, G. L. Skibinski, and R. M. Tallam, "Determination of Parameters in the Universal Induction Motor Model," *IEEE Transactions on Industry Applications,* vol. 45, no. 1, pp. 142-151, 2009.

[57]   A. F. Moreira, T. A. Lipo, G. Venkataramanan, and S. Bernet, "High-frequency modeling for cable and induction motor overvoltage studies in long cable drives," *IEEE Transactions on Industry Applications,* vol. 38, no. 5, pp. 1297-1306, 2002.

[58]   A. Binder and A. Muetze, "Scaling Effects of Inverter-Induced Bearing Currents in AC Machines," *IEEE Transactions on Industry Applications,* vol. 44, no. 3, pp. 769-776, 2008.

[59]   G. Costabile *et al.*, "An accurate evaluation of electric discharge machining bearings currents in inverter-driven induction motors," in *2007 European Conference on Power Electronics and Applications*, 2007, pp. 1-8.

[60]   C. 25, "Limits and methods of measurement of radio disturbance characteristics for protection of receivers used on board vehicles," 2002-08.

[61]   D. Han, C. T. Morris, W. Lee, and B. Sarlioglu, "Comparison Between Output CM Chokes for SiC Drive Operating at 20- and 200-kHz Switching Frequencies," *IEEE Transactions on Industry Applications,* vol. 53, no. 3, pp. 2178-2188, 2017.

[62]   A. Muetze and C. R. Sullivan, "Simplified Design of Common-Mode Chokes for Reduction of Motor Ground Currents in Inverter Drives," *IEEE Transactions on Industry Applications,* vol. 47, no. 6, pp. 2570-2577, 2011.

[63]   P. Chen and Y. Lai, "Effective EMI Filter Design Method for Three-Phase Inverter Based Upon Software Noise Separation," *IEEE Transactions on Power Electronics,* vol. 25, no. 11, pp. 2797-2806, 2010.

[64]   O. e. C. USA. (2017). *Bode 100 user manual (Package Version ENU1006 05 01 ed.)*. Available: https://www.omicron-lab.com/fileadmin/assets/manuals/Bode-100-User-Manual-ENU10060501.pdf

[65]   M. Moreau, N. Idir, and P. L. Moigne, "Modeling of Conducted EMI in Adjustable Speed Drives," *IEEE Transactions on Electromagnetic Compatibility,* vol. 51, no. 3, pp. 665-672, 2009.

[66]   X. Gong, I. Josifović, and J. A. Ferreira, "Modeling and Reduction of Conducted EMI of Inverters With SiC JFETs on Insulated Metal Substrate," *IEEE Transactions on Power Electronics,* vol. 28, no. 7, pp. 3138-3146, 2013.

[67]   O. Magdun and A. Binder, "High-Frequency Induction Machine Modeling for Common Mode Current and Bearing Voltage Calculation," *IEEE Transactions on Industry Applications,* vol. 50, no. 3, pp. 1780-1790, 2014.

[68]   J. Xue and F. Wang, "Modeling and design of common-mode inductor for conductive EMI noise suppression in DC-fed motor drive system," in *2012 IEEE Energy Conversion Congress and Exposition (ECCE)*, 2012, pp. 645-651.

[69]   C. R. Sullivan and A. Muetze, "Simulation Model of Common-Mode Chokes for High-Power Applications," *IEEE Transactions on Industry Applications,* vol. 46, no. 2, pp. 884-891, 2010.

[70]   D. Han, C. Morris, W. Lee, and B. Sarlioglu, "Determination of CM choke parameters for SiC MOSFET motor drive based on simple measurements and

frequency domain modeling," in *2016 IEEE Applied Power Electronics Conference and Exposition (APEC)*, 2016, pp. 2861-2867.

[71] D. Liu and X. Jiang, "High frequency model of common mode inductor for EMI analysis based on measurements," in *2002 3rd International Symposium on Electromagnetic Compatibility*, 2002, pp. 462-465.

[72] I. Boldea and S. A. Nasar, *Electric drives*. CRC press, 2016.

[73] F. Luo *et al.*, "Analysis of CM Volt-Second Influence on CM Inductor Saturation and Design for Input EMI Filters in Three-Phase DC-Fed Motor Drive Systems," *IEEE Transactions on Power Electronics,* vol. 25, no. 7, pp. 1905-1914, 2010.

[74] L. Xing, M. Shen, M. Li, and W. Said, "Common mode choke optimization for three-phase motor drive systems," in *2012 IEEE Energy Conversion Congress and Exposition (ECCE)*, 2012, pp. 1399-1405: IEEE.

[75] S. Ogasawara and H. Akagi, "Modeling and damping of high-frequency leakage currents in PWM inverter-fed AC motor drive systems," *IEEE Transactions on Industry Applications,* vol. 32, no. 5, pp. 1105-1114, 1996.

[76] A. Roc'h and F. Leferink, "Nanocrystalline Core Material for High-Performance Common Mode Inductors," *IEEE Transactions on Electromagnetic Compatibility,* vol. 54, no. 4, pp. 785-791, 2012.

[77] Y. a. Yoshizawa, S. Oguma, and K. J. J. o. a. P. Yamauchi, "New Fe‑based soft magnetic alloys composed of ultrafine grain structure," vol. 64, no. 10, pp. 6044-6046, 1988.

[78] Vacuumschmelze. (2011). *Nanocrystalline material in common mode chokes*. Available: www.vacuumschmelze.com

[79] VacuuMscHMElZE. (2016). *EMC Products Based on Nanocrystalline Vitroperm*. Available: https://www.mouser.com/pdfdocs/VACChokesandCoresDatasheet.pdf

[80] D. Han, C. T. Morris, W. Lee, and B. Sarlioglu, "Three-phase common mode inductor design and size minimization," in *2016 IEEE Transportation Electrification Conference and Expo (ITEC)*, 2016, pp. 1-8.

[81] M. K. Jutty, V. Swaminathan, and M. K. Kazimierczuk, "Frequency characteristics of ferrite core inductors," in *Proceedings of Electrical/Electronics Insulation Conference*, 1993, pp. 369-372.

[82] A. Massarini and M. K. Kazimierczuk, "Self-capacitance of inductors," *IEEE Transactions on Power Electronics,* vol. 12, no. 4, pp. 671-676, 1997.

[83] H. Chen, Z. Qian, S. Yang, and C. Wolf, "Finite-Element Modeling of Saturation Effect Excited by Differential-Mode Current in a Common-Mode Choke," *IEEE Transactions on Power Electronics,* vol. 24, no. 3, pp. 873-877, 2009.

[84] J. Xue, F. Wang, and B. Guo, "EMI noise mode transformation due to propagation path unbalance in three-phase motor drive system and its implication to EMI filter design," in *2014 IEEE Applied Power Electronics Conference and Exposition - APEC 2014*, 2014, pp. 806-811.

[85] D. Bellan, "Mode transformation of EMI noise due to unbalanced filter capacitors in three-phase motor drive systems," in *IECON 2017 - 43rd Annual Conference of the IEEE Industrial Electronics Society*, 2017, pp. 7024-7027.

[86] D. Drozhzhin, G. Griepentrog, A. Sauer, R. D. Maglie, and A. Engler, "Investigation on differential to common mode coupling in the output cable of

AC drive for more electric aircraft," in *2017 19th European Conference on Power Electronics and Applications (EPE'17 ECCE Europe)*, 2017, pp. P.1-P.9.

[87]   S. Wang and F. C. Lee, "Investigation of the Transformation Between Differential-Mode and Common-Mode Noises in an EMI Filter Due to Unbalance," *IEEE Transactions on Electromagnetic Compatibility,* vol. 52, no. 3, pp. 578-587, 2010.

[88]   J. Meng and W. Ma, "A new technique for modeling and analysis of mixed-mode conducted EMI noise," *IEEE Transactions on Power Electronics,* vol. 19, no. 6, pp. 1679-1687, 2004.

[89]   S. Qu and D. Chen, "Mixed-mode EMI noise and its implications to filter design in offline switching power supplies," *IEEE Transactions on Power Electronics,* vol. 17, no. 4, pp. 502-507, 2002.

[90]   J. Xue and F. Wang, "Mixed-mode EMI noise in three-phase DC-fed PWM motor drive system," in *2013 IEEE Energy Conversion Congress and Exposition*, 2013, pp. 4312-4317.

[91]   F. Fan, K. Y. See, J. K. Banda, X. Liu, and A. K. Gupta, "Simulation of three-phase motor drive system with bearing discharge process," in *2017 Progress in Electromagnetics Research Symposium - Fall (PIERS - FALL)*, 2017, pp. 2091-2097.